© 2016 Matthew L.S. Zappulla

GRADE EFFECTS ON THERMAL-MECHANICAL BEHAVIOR DURING THE INITIAL SOLIDIFICATION OF STEEL

BY

MATTHEW L.S. ZAPPULLA

THESIS

Submitted in partial fulfillment of the requirements
for the degree of Master of Science in Mechanical Engineering
in the Graduate College of the
University of Illinois at Urbana-Champaign, 2016

Urbana, Illinois

Adviser:

Professor Brian G. Thomas

Abstract

This work takes initial steps towards the ultimate goal of fundamental understanding of how cracks and depressions form during continuous casting of steel, and demonstrates a tool towards troubleshooting and preventing them. Mathematical models are developed and applied to examine thermal and mechanical behavior in the mold region of the continuous casting process. First, the models are used to study the effect of changes in steel grade early in the process for uniform solidification. Next, a thermal resistor model was developed of the interfacial gap, and finally, these two models are combined for a preliminary coupled analysis of a depression.

The effect of different steel grade on the relevant behavior is captured according to the phase fractions and the properties of each phase. The model is validated using analytical solutions, and applied to explore the behavior of four different steel grades: Ultra-Low Carbon (0.003 %C), Low Carbon (0.04 %C), Peritectic (0.13 %C), and High Carbon (0.47 %C), simulating 30 s dwell times. Mesh refinement for capturing solidification details was examined and element sizes of 0.1 mm or smaller may be required to properly study solidification phenomena. All steel grades were found to follow the same general solidification behavior of compression at the surface increasing with time, and tension towards the solidification front. The initial solidification rate increases with carbon content. Thermal strain dominates the mechanical behavior. More stress and inelastic strain are generated in the high carbon steels, because they are mainly composed of high-strength austenite. Stress in the δ-ferrite phase is always very small, owing to the low strength of this phase. This simple model can help in the calculation of taper

profiles for different steel grades and maintain the desired contact with the mold. While fixed linear taper practices are common in industry, this work demonstrates that the desired profile of the shell is actually parabolic.

A thermal resistor model was developed to examine heat transfer phenomena within the interfacial gap during continuous casting. Results show that increasing slag layer thickness decreases heat flux across the gap. In addition, decreasing solidification temperature of the mold flux, for a fixed gap size, leads to more high-conductivity liquid present in the gap, so the heat flux rises. Finally, this work demonstrates an example of combining the realistic thermal-resistor model of the gap together with the thermal-mechanical model to show the different local behavior that can occur at a depression. Differences in flux layer thickness at the depression cause a drop in heat flux, higher surface temperatures, and a drop in shell thickness, which can result in necking phenomena in the solid shell as the stress from the shrinkage of the surrounding material concentrates in thinned shell regions.

This work is the first step in demonstrating a transient 3-D model of thermal-mechanical behavior to examine the formation of cracks and depressions - where the correct behavior can be verified in a simplified case where an analytical solution exists, while allowing for extensions to higher dimensional modeling work in the future.

For R.L.Z. & L.B.P.Z.

You taught me to always have a plan.

Acknowledgments

I would like to thank my advisor Professor Brian G. Thomas for his unflinching support and guidance through the past 4 years of work, thank you for always asking the right questions at the right times.

All the students of the CCC: Kenny Swartz, Eric Badger, Aravind Murali, Brendan Joyce, Gavin Hamilton, Pete Srisuk, Ramnik Singh, Seong-Mook Cho, Prathiba Divuuri, Adnan Akhtar, Hyung-Jin Lee, Hyunjin Yang, Kun Xu, Kai Jin, Nathan Seymour, Yonghui Li, Xialou Yan, A.S.M. Jonayat

Particular mention to Dr. Lance C. Hibbeler, Dr. Bryan Petrus, Dr. Rui Liu, and Dr. Joydeep Sengupta for many shared pints of advice; as well as Dr. Seid Koric for his helpful support with HPC and when ABAQUS just doesn't want to work.

I also gratefully acknowledge the financial support by the member companies of the Continuous Casting Consortium at the University of Illinois at Urbana-Champaign, whos current members include: ANSYS-Fluent, Baosteel, Nucor, Magnesita Refractories, Arcelor-Mittal, SSAB, Postech/Posco, AK Steel, ABB, Nippon Steel and Sumitomo Metals Corp., JFE Steel, Severstal, and Tata Steel. This work was also supported by the National Science Foundation (Grant Number: CMMI-1300907), as well as part of the Blue Waters sustained-petascale computing project, which is supported by the National Science Foundation (awards OCI-0725070 and ACI-1238993) and the state of Illinois. Blue Waters is a joint effort of the University of Illinois at Urbana-Champaign and its National Center for Supercomputing Applications.

This work would also not have been possible without the support of all my friends, you truly helped me keep my sanity.

Table of Contents

List of Tables ix

List of Figures x

Chapter 1 Introduction 1
1.1 Steel 1
1.2 The Continuous Casting Process 2
1.3 Steel Alloying 4
1.4 Continuous Casting Defects 6
1.5 Objectives of Current Work 10

Chapter 2 Steel Grade Effects On Solidification Behavior 12
2.1 Abstract 12
2.2 Introduction 13
2.3 Goals 15
2.4 Model Description 16
2.5 Heat Flux 22
2.6 Steel Grades and Phase Fractions 26
2.7 Material Properties 29
2.8 Model Validation 37
2.9 Solution Method & Details 41
2.10 Results and Discussion 41
2.11 Conclusions 58
2.12 Future Work 60

Chapter 3 Thermal Resistor Model of the Shell-Mold Gap 61
3.1 Introduction 61
3.2 Mold Gap Phenomena 62
3.3 The Model 73
3.4 Heat Transfer Model Results 76
3.5 Coupled Thermal-Mechanical Model of Slag Finger Depression . . 79
3.6 Conclusions 87
3.7 Future Work 87

Chapter 4 Conclusions and Future Work 88
4.1 Conclusions 88
4.2 Future Work 90

Appendix A Ferrostatic Pressure 92
A.1 Ferrostatic Pressure 92

Appendix B ABAQUS Operational Notes, Input Files & Scripts 96
B.1 Contact 97
B.2 Frictional Force Balance 98
B.3 Example Input Files 102
B.4 GAPCON for Resistor Model 110
B.5 Parametric Study Scripts 115

References 122

List of Tables

2.1 Heat flux profile coefficients 26
2.2 Steel grade compositions [% wt.] 29
2.3 Steel grade transition temperatures [°C] 29
2.4 Properties used in the Weiner and Boley test problem 37

3.1 Gap conductivity and resistance values 72

List of Figures

1.1 Bessemer's patented manufacturing method 2
1.2 Continuous casting process schematic 3
1.3 Dendrite strength and ductility 7
1.4 Depressions, cracks, and observed phenomena 9
1.5 Examples of observed cracks/depressions 9

2.1 Simulation domain 16
2.2 Thermal and mechanical boundary conditions 17
2.3 Instantaneous and average heat flux curves 23
2.4 Measured heat removed and fitted curves 25
2.5 Pseudo-binary iron-carbon phase diagram 27
2.6 Phase fractions for four steel grades investigated 28
2.7 Temperature and grade dependent specific heat capacity 30
2.8 Temperature-dependent properties of steel grades investigated . . 33
2.9 Temperature-dependent elastic modulus of steel 35
2.10 Comparison of Weiner & Boley and ABAQUS results 38
2.11 Mesh study results for low carbon steel 40
2.12 Behavior of unconstrained and constrained solidifying plates . . . 42
2.13 Low carbon steel contour plot results 43
2.14 Temperature and Y-Stress contour plot results 45
2.15 Typical strain distribution through the shell thickness 46
2.16 Strain contours for five casting situations investigated 50
2.17 Surface profiles for five casting situations investigated 52
2.18 Y-stress profiles through shell thickness 53
2.19 Temperature profile through the shell thickness 54
2.20 Ideal taper profile for five casting situations investigated 54
2.21 Thermal strain at the shell surface 56
2.22 Parabolic taper profile 58

3.1 Schematic of slag layers in the mold 62
3.2 Contact interface roughness 64
3.3 Temperature dependent slag/strand interface resistance 65
3.4 Crystallinity and thickness dependent conductivity 67
3.5 Temperature dependent conductivity 68
3.6 Interfacial gap material schematic 72

3.7 Interfacial gap resistor schematic 73
3.8 Calculation flowchart for resistor model 75
3.9 Projected and actual heat flux 76
3.10 Flux layer thickness variation 77
3.11 Effect of solidification temperature variation 78
3.12 Time varying flux thickness 78
3.13 Slag finger domain 80
3.14 Slag finger mesh 80
3.15 Slag finger thermal boundary conditions 81
3.16 Slag finger model implementation 81
3.17 Slag finger mechanical boundary conditions 82
3.18 Slag finger model results 83
3.19 Slag finger model deformed shape 84
3.20 Y-heat flux contour plot showing distorted elements 84
3.21 Slag finger temperature results 85
3.22 Slag finger liquid fraction contour 86
3.23 Slag finger thermal boundary conditions 86

A.1 Ferrostatic pressure applied pulling on domain 93
A.2 Ferrostatic pressure applied pushing on domain 94
A.3 Results of varied ferrostatic pressure application 95

B.1 Internal force balance at 10 s 99
B.2 External force balance at 10 s 100

Chapter 1

Introduction

1.1 Steel

Steel by definition is a metal alloy that is composed primarily of Iron and Carbon; yet for it's seeming simplicity, steel is one of the most versatile and fundamental building blocks of the modern world.

Steelmaking has evolved over the course of hundreds of years from the blacksmiths of the middle ages [1] to the Bessemer process [2]. The process patented by Bessemer in the mid 1800's, shown in Figure 1.1, is quite similar to the method employed in modern strip casting. However, at the time of the patent it proved very difficult to control and the quality of the final products was far inferior to other methods [3] which slowed it's adoption.

The introduction of mold oscillation in the 1930's by Siegfried Junghans brought about the start of a functionally continuous process. Further developments in the 1950's and 60's saw the development of modern continuous casting [4] including the successful operation of the worlds first production scale continuous casting machines [3]. In the beginning only vertical casters were constructed, this presented issues due to the long time period required for complete solidification. Introduction of the arc-type machine alleviated this difficulty, and continuous casting quickly began to spread, and by the 1990's was the production method for the majority of the world's total crude steel.

Steel offers one of the most efficient cost-to-weight ratios of any manufacturing material and it's strength is unparalleled. It is found everywhere from construction equipment to construction material, infrastructure to transportation, and even

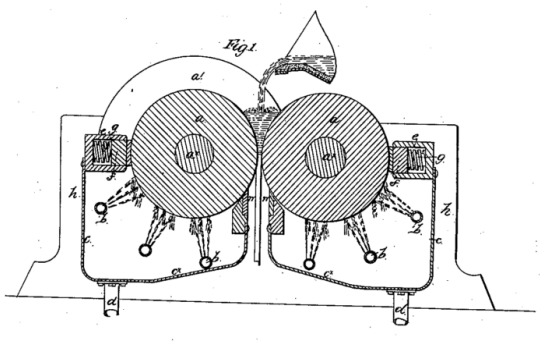

Figure 1.1: Bessemer's patented manufacturing method for iron and steel [6]

household appliances. Total crude steel production exceeded 1.6 billion metric tonnes in 2014 and worldwide continuous casting production has grown from 91% in 2004 to 96% in 2014 [5].

1.2 The Continuous Casting Process

The basic principle of the continuous casting process for steel is based on pouring liquid steel into a water cooled copper mold which is also open at the bottom as shown in Figure 1.2. Preparation of the liquid steel is conducted elsewhere in the plant inside of large ladles made of ceramic refractory material and is referred to as steelmaking and metallurgy.

Primary steelmaking begins with melting, refining, and homogenization of the raw materials [8]. The Basic Oxygen Furnace (BOF) is used for iron ore/pig iron and with the high reusability of steel, Electric Arc Furnaces (EAF) are often used with steel scrap [9] as well as Direct Reduced Iron (DRI). After primary steelmaking, the hot metal is poured into a ladle and transported to secondary metallurgy. In secondary metallurgy, the metal undergoes alloying, desulfurization, vacuum treating, decarburization, deoxidation and other treatments necessary to achieve the composition and properties desired for the final product [10]. The final product out of secondary steelmaking and metallurgy is a ladle full of molten steel to be cast - weighing in excess of 300 metric tonnes. The ladles usually travel to the

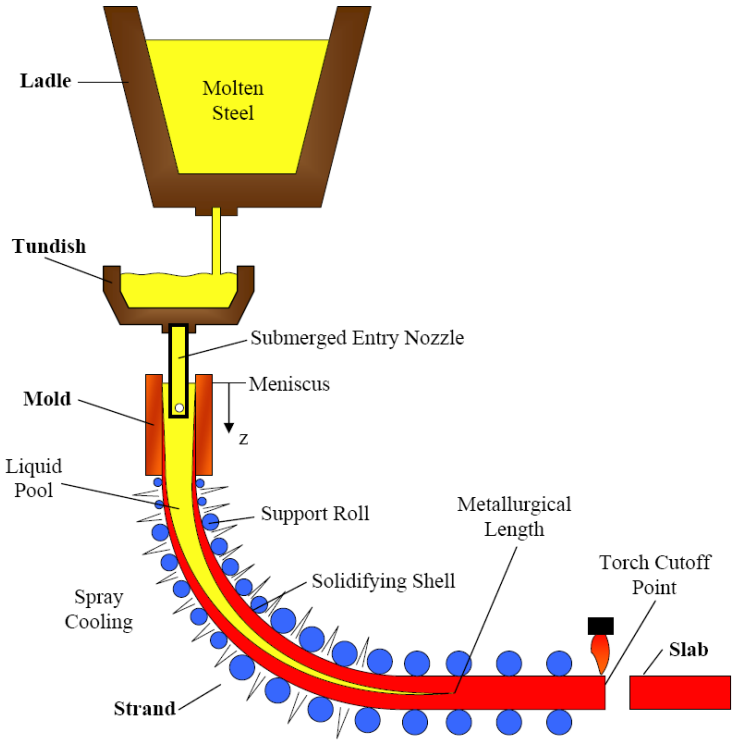

Figure 1.2: Continuous casting process schematic [7]

caster by a combination of tundish cars on railroad tracks and overhead cranes.

Liquid steel is fed from the tundish into the mold through the Submerged Entry Nozzle (SEN) [11]. The main purpose of the tundish is to act as a buffer so that the process is continuous between ladle changes, however, it also provides more opportunity for separation of oxide inclusion [12] as well as a smooth and stable pattern for flow into the mold thereby reducing level issues near the meniscus [13]. The flow of molten steel into the mold is controlled by either a stopper rod in the base of the tundish or a slide-gate within the SEN itself. Swing towers or ladle turrets, devices capable of holding the next ladle in position, have enabled smoother operation and reduced sequence time for ladle exchange [3].

Refractory nozzles in the bottom of the tundish distribute liquid steel into the mold and heat transfer to the water cooled copper immediately solidifies the liquid steel and begins to grow the steel shell. The mold is oscillated vertically to prevent the solidifying shell from sticking to the mold walls. Mold powder is added to the free surface of the liquid steel not only to provide thermal and chemical insulation

from the environment, but also as lubricant in the interface between the solidifying shell and the mold.

To start up the caster, a dummy bar is used to 'plug' the mold from the bottom to allow the initial steel to solidify and support the process above. The bar is withdrawn from the machine, disconnected, and process is then capable of continuous operation. As soon as the solidified shell is sufficiently thick to contain the liquid steel, the strand is withdrawn from the mould at a rate referred to as the casting speed V_C using drive rollers and is further cooled by water sprays of the secondary cooling system. The hot solidified skin of the shell cannot withstand the pressure exerted by the liquid steel (ferrostatic pressure) within the shell above and would bulge outwards if not constrained. Therefore, it is necessary to support the continuously solidifying shell using support rolls below the mold.

The thickness of the shell increases with distance from the meniscus down the length of the mold. The strand becomes completely solid after passing several meters down the machine where the two sides of the growing shell meet. The distance from the meniscus to this location is referred to as the metallurgical length and varies from caster to caster as well as a variety of casting conditions. The final cast product is cut to length by an oxy-acetelyne torch that travels with the strand at the casting speed, or in some cases with a pendulum shear.

1.3 Steel Alloying

As discussed in Section 1.2, the composition of steel is prepared during steel-making and metallurgy. Alloy steels are made by additions of one or several alloying elements, the most important being Carbon, which determines the type of steel as well as it's castability, and many other properties. Other elements are added in varying proportions (or combinations) and the material takes on different characteristics such as increased hardness, corrosion resistance, strength, improved ductility, and manufacturability. Besides Carbon, common additions & their effects [14] include:

Aluminum: Used as deoxidizer, restricts grain growth, helpful in nitriding

Chromium: Increased hardenability, toughness; and corrosion and wear resistance

Cobalt: Used in making cutting tools; improved hot hardness in ferrite

Manganese: Counteracts sulfur embrittlement, increased surface hardness & shock resistance

Molybdenum: Increases strength, resistance to shock and heat, higher creep strength

Nickel: Low temperature strength in pearlite and ferrite, Improves corrosion resistance

Phosphorus: Strengthen low C steels and can improve machinability

Silicon: Improved electrical properties, oxidation resistance, strengthen low alloy steels

Tungsten: Adds hardness, improves grain structure, and heat resistance

Vanadium: Grain refiner in austenite, increased strength, toughness and shock resistance

Other trace elements are always present in small amounts, and are often unintended "residuals"; these include: Sulfur, Phosphorus, Silicon, Oxygen, Nitrogen, Copper, Tin, Antimony, Bismuth, and a host of others.

For all of the ambient temperature benefits and performance gains that these alloys provide to final steel products, addition of them to the steelmaking process increases the complexity and makes it difficult to troubleshoot intermittent problems, such as depressions and cracks during the continuous casting process. Each company has their own offering of steel grades to meet the needs of customer and industry demand, and decisions for grades to be cast are usually made far in advance of the actual casting. Recent years have seen the appearance of TRIP (TRansformation Induced Plasticity), TWIP (TWinning Induced Plasticity), and AHSS (Advanced High Strength Steel) grades [15] in the market and with their increased durability and strength, come a host of difficulties upstream as their properties are not always fully understood. Due to this lack of fundamental knowledge, understanding the basic behavior of steel solidification as well as observed trends is crucial to making decisions about casting conditions, especially when it comes to new grades.

1.4 Continuous Casting Defects

Cracks and depression formation are dangerous quality defects that have affected the steel casting industry since its inception; in the final product they can lead to loss of millions of dollars or sudden failures, and in the worst case can lead to catastrophic breakouts in an operating caster.

The continuous casting process itself has a high predisposition for generating cracks [16]; The high rate of heat removal results in steep temperature gradients and thus high thermal strains and stresses as the shell attempts to expand or contract - particularly in transverse planes through the strand. It also becomes subjected to mechanical stresses from the mold, rolls, ferrostatic pressure, bending and straightening, most notably in longitudinal planes including the casting direction. While it is widely accepted that embrittlement and tensile stress are necessary to initiate a crack, there is still a lot that is unknown about their exact origins.

Low strength and ductility are often associated with the presence of liquid films in interdendritic spaces. A schematic is shown in Figure 1.3. These films are known to be highly segregated, have depressed solidus temperatures, and thus are not as strong as the dendrites themselves [16]. Compositional effects are often discussed qualitatively in the literature, such as the observation that lower Manganese to Sulfur ratios as well as elevated levels of Aluminum, Nitrogen, Sulfur, and Copper can result in more cracks. The literature includes a variety of compositional heuristics for crack formation, but the peritectic phase transformation associated with the iron-carbon phase diagram is the most prevalent trend. Cracks are more likely in "peritectic steels", found between the limit of carbon solubility in delta-ferrite, 0.09%C, and the peritectic composition of 0.16%C, depending on other alloying elements, with an additional elevated likelihood in the ultra-low carbon range (e.g. $< 0.005\%$C).

This peritectic range of steel grades is known to have a variety of difficulties associated with casting due to its complex behavior during solidification and

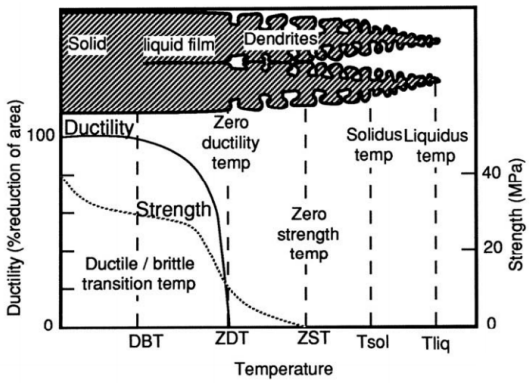

Figure 1.3: Dendrite strength and ductility

solid-state phase transformations, and subsequent rippled shell surface. While these ripples can provide strong sites for crack initiation they would likely lead to transverse cracks in operations with controlled oscillation and horizontal oscillation marks. This suggests that longitudinal cracks in peritectic steels may be caused by other secondary factors.

Rapid shrinkage can be quite large in the case of peritectic steels (over other carbon steels) and because of this, the shell may lose contact with the wall. This loss of contact can result in shell thinning, and thus lead to cracking further down the mold as local shell regions change phase at different times. The ultra-low carbon range is also expected to have this predisposition to cracking. This is potentially due to the long duration of the delta ferrite to austenite transition period, but again, the general occurrence and predisposition is known, but not the exact formation mechanisms.

Heat removal from the steel shell in the mold is controlled mainly by the heat conduction across the interface between the shell and the copper mold. It has been estimated that the gap alone accounts for as much as 84% of the total resistance, while the mold wall and the mold/cooling water interface account for the balance of 16% [17]. Thus, the pattern of heat removal in the mold is dependent largely on the dynamics of gap formation, which is in itself a very complicated process and the subject of much research interest.

Proper mold care is important to minimize cracks. Improper over-taper may

push on the weak shell and distort it, this is more common towards mold exit. Improper under-taper (usually occuring towards the middle of the mold) or improper sub mold support can allow the strand to move around or bulge from ferrostatic pressure. Irregular mold oscillation can result in deeper oscillation marks or potentially slag getting stuck between the mold and shell. Mold wear is known to change the taper over the life of the mold and if this is not accounted for unintended bad taper practices may occur. Each of these mechanical mold issues also mean deviation from uniform heat transfer, this can cause local reheating and weakening of the shell. This reheating is significant for a number of reasons not just related to the strength of the material. If the temperature change is significant enough a phase transformation may take place, meaning not only a thinner shell is present, but in the case of reheating from austenite, the potential appearance of a weak delta ferrite phase surrounded by colder and much stronger austenite.

Much of the contemporary literature is concerned with the micro-scale and compositional phenomena related to cracking. This is good on a fundamental level and a complete understanding will expand the tools we have to fix such issues, however, it does leave many unanswered questions. We know compositional differences are known to have a strong effect on crack susceptibility, but we know little about the differences in cause: Is the physical mechanism that is responsible for peritectic cracking, the same as that of the ultra-low carbon steel? Cracks are widely known to appear at the base of depressions, and deeper and wider surface cracks are seen to generally appear at the base of deeper and wider depressions as shown in Figures 1.4 and 1.5. However, it is observed that in many cases, depressions appear without surface cracks. This begs the question, what is it about certain depressions that cause them to develop a crack?

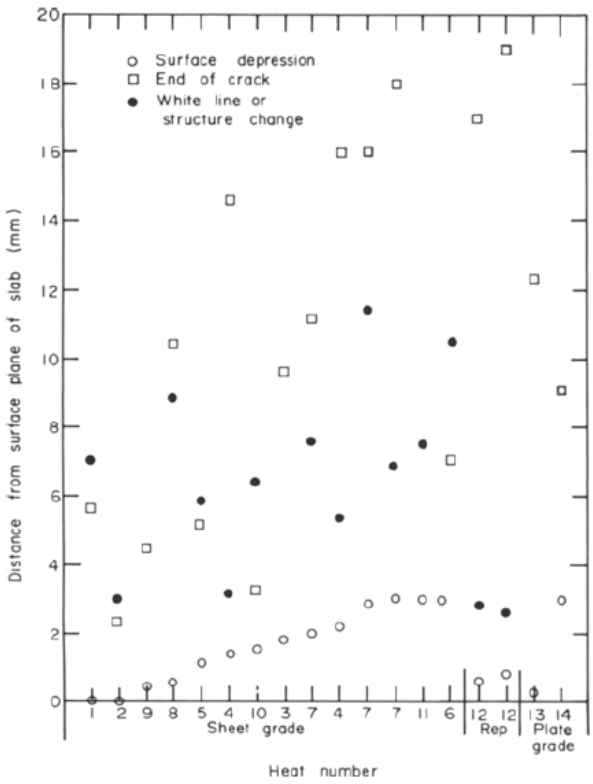

Fig. 5—Depth of crack, surface depression and white line (or structure change) below surface plane of slab for different heats.

Figure 1.4: Depressions, cracks, and observed phenomena [16]

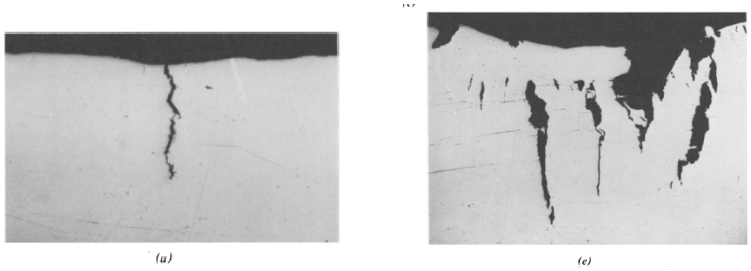

Figure 1.5: Examples of observed cracks/depressions

Heat transfer issues within the mold have a significant effect on final cast shape. Flux layer thickness variations, scratches on the surface of the copper (or coating), water channel scaling and clogging, premature or uneven mold wear, all of these can create local heat transfer nonuniformities. But do they all result in the same final defect? Can the final shape of the depression help to identify the root cause?

How large can a mold scratch be before we begin to see indications on the slab? How do flux thickness variations translate to the final shell?

Cracks and depressions are still one of the most costly defects in continuous casting, many times resulting in resurfacing, scarfing, downgrading, or complete scrapping. As technology has increased so too has our ability to limit and confine our defects to smaller sizes, and less detrimental areas. However, cracks remain an issue at many casters and while general causes are known, little is known (and proven) on the process of formation. Much of the knowledge that does exist is empirical, and there is quite a bit still unknown about the fundamental mechanisms; as such more work is needed on the steps that can be taken when troubleshooting a caster that is producing a high amounts of them.

1.5 Objectives of Current Work

While the continuous casting process, and steelmaking in general, is one of the oldest processes of the industrialized world, it is clear that its complexities are vast. As industrial experience and research budgets increase in continuous casting, improvements are seen across the board. Previous advances have mainly come from trials at operating steel plants. But, as the process improves, and defects become more intermittent, this "trial and error" approach becomes more expensive. With continuous casting production measured in the *billions* of metric tonnes per year, any small improvement in the process leads to increases in throughput, efficiency, and cost savings.

Modeling, more specifically computational modeling, allows engineers to take a unique real world situation, make assumptions, and distill it into its most relevant and basic parameters. Computational modeling affects our lives daily from weather forecasts to traffic patterns and power grid operations. By making these simplifications we can study and begin to understand the phenomena and behavior in different situations that might otherwise be extremely expensive or unrealistic to duplicate in the real world. Continuous casting research stands to

benefit greatly from computational modeling as the real process environment is so hazardous that conventional experimental techniques are often inadequate and dangerous at the temperatures and conditions that are present at an operating caster.

This work aims to take initial steps towards the ultimate goal of fundamental understanding of crack formation and to evaluate the differences of how stress and strain develop between steel grades. This will provide knowledge towards better understanding of how cracks and depressions form, and assist in troubleshooting and preventing them, and within these tools and understanding, examining the effect of steel grade on that behavior.

This thesis is divided into 3 chapters which follow this introduction. First, a mathematical model is presented and applied to examine the thermal-mechanical solidification behavior of 4 different steel grades utilizing grade- and temperature-dependent properties. This model is used to explore the behaviors that result from the different phase transformation histories in commercially cast steels, with uniform solidification of a plate as a starting point. Then, a temperature-dependent thermal resistor model of the interfacial gap is proposed and demonstrated to allow for coupled thermal and stress modeling. In addition it introduces the opportunity to alter the heat flux profile throughout the entire mold. In this way we can examine the effect of uniform and nonuniform flux thickness variations Imposed air gaps, slag fingers, and a variety of other potential mold scenarios. Finally, the coupled thermal stress model is used to simulate a flux layer thickness variation and the formation of a depression during continuous casting in the model.

Chapter 2

Steel Grade Effects On Solidification Behavior

2.1 Abstract

A mathematical model has been developed, using ABAQUS finite element software [18], to study the effect of grade on temperature, stress, strain, and shell development early in the solidification process of continuously cast steels and use it to help design continuous casting taper profiles for different steels. This work investigates the effect of grade on thermal-mechanical behavior during initial solidification of steels during continuous casting of a wide strand. The employed finite-element model uses an efficient algorithm to integrate the nonlinear temperature- and phase-dependent elastic-viscoplastic constitutive equations [19]. The model is validated using an analytical solution, and a mesh convergence study is performed. Four steel grades are simulated for 30 s of casting without friction: Ultra-Low Carbon (0.003%C), Low Carbon (0.04%C), Peritectic (0.13%C), and High Carbon (0.47%C). All grades show the same general behavior. Initially, fast cooling causes tensile stress and inelastic strain near the surface of the shell, with slight complementary compression beneath the surface, especially with lower carbon content. As the cooling rate decreases with time, the surface quickly reverses into compression, with a tensile region developing towards the solidification front. Higher stress and inelastic strain are generated in the high carbon steels, because they contain more high-strength austenite. Stress in the δ-ferrite phase near the solidification is always very small, owing to the low strength of this phase. The total strain remains uniform through the thickness, and becomes increasingly negative at a decreasing rate as the dwell time increases. After a great amount of

shrinkage in the first few seconds, the shell shrinks at a decreasing rate, which was used to calculate grade-specific ideal taper profiles. All grades follow a similar, roughly parabolic shape, except for the peritectic, which was either larger or smaller, depending on the heat transfer.

2.2 Introduction

The surface quality of cast metal products depends significantly on initial solidification behavior. In casting processes, such as continuous casting, die casting and ingot casting, defects such as cracks, segregation, porosity, and microstructural or grain defects that appear in the newly-solidified shell may evolve and lead to problems in the final product, even after many subsequent processing steps.

Steel composition strongly affects the surface quality of continuously cast steels, especially for grades involving the peritectic transformation. In addition, each steel grade has slightly different shell growth, shrinkage, and thermal-mechanical characteristics. Fundamental understanding of these phenomena is especially required when developing and solving problems in new steel grades, such as Advanced High Strength Steels (AHSS). The extreme environment of steel casting processes makes experimentation difficult. Thus, modeling is an important tool in the development of this understanding.

The thermal and mechanical behavior of the solidifying shell is explored in this work using a computational model. Four steel grades are studied to explore the typical behavior of four different types of phase transformation histories in the iron-rich side of the $Fe - Fe_3C$ phase diagram: ultra-low carbon (ULC) with 0.003 wt. %C, low carbon (LC) with 0.045 wt. %C, peritectic (P) with 0.13 wt. %C, and high-carbon (HC) with 0.47 wt. %C.

2.2.1 Literature Review

In preparation for this work, a literature review was conducted to examine the state-of-the-art and identify potential gaps in knowledge. Previous studies have often focused on the effect of steel grade on micro-scale behavior such as the formation of dendrites during solidification [20–24], segregation [20, 25–30], the columnar-to-equiaxed transition [22, 29, 31–33], and damage criteria for hot tear crack formation [34–37]. Other studies have examined macroscopic scale behavior, such as shell growth [38–40], shell shrinkage [41, 42], solidification force [43, 44], stress development [45, 46], hot ductility [26, 47–49], and strain to failure [50].

Small differences in steel composition can greatly change evolution of the phase fractions during solidification [26, 51], and consequent changes in the material properties and behaviors. Specifically, ultra-low carbon steels and peritectic steels experience much greater mechanical deformation during solidification than do low- and medium carbon steels, which consequently causes lower and less-uniform heat transfer [52], and greater crack susceptibility for peritectics [39,53,54]. Identifying phase fraction histories is a useful step in predicting these phenomena. Tools to study the equilibrium phases of steels have used experimental methods involving slow cooling rates, such as Differential Scanning Calorimetry [55, 56], as well as steel-composition-dependent phase diagrams [30, 57], and applying free-energy-based models, such as Thermocalc and Factsage to steel [58–60]. Some tools, such as IDS, model species diffusion to incorporate non-equilibrium kinetic effects in finding the phase fractions [27].

Steel properties at high temperature are difficult to measure; only a few papers have measured thermal properties [61,62] or mechanical testing in the appropriate regime of low-strain (< 2 %), and low-strain-rate (10^{-5} to 10^{-2} %/s), which include tensile tests on austenite and ferrite [48, 63] and creep tests above $800°C$ [40].

Previous macro-scale thermal-mechanical modeling work [41,46,64–73] has been conducted using temperature-dependent constitutive and material properties in-

cluding studies for billets [41, 67–71], slabs [41, 72], as well as work towards better taper prediction [41, 46, 66, 67, 71–73].

Other models have used phase field modeling which include studies on hot tear sensitivity [51, 74] and microstructure evolution [75, 76]. Only a few previous models have investigated the effect of steel grade on initial solidification, such as the deformed shape of solidifying droplets [77] or continuously-cast shells [65].

The current work models the macroscale thermal-mechanical behavior during the initial solidification of a steel casting process; it presents validation using an analytical solution, and then applies the model to explore the fundamental differences between steel grades, in the context of a typical continuous steel casting process.

2.3 Goals

While the literature supplies useful tools for understanding some of the expected behavior, these previous models have been applied to varying steel grades but in a limited manner and not with differences in grade behavior being the primary focus. This work demonstrates the methodology necessary to model and capture the relevant behavior in a solidification problem; it also explores the basic property differences between steel grades, presents validation using analytical solutions, and a simulation of a continuous thin slab steel casting process where the shrinkage and solidification behavior of each grade is explored. In addition, we show a comparison of stress and strain profiles for each grade with the same interfacial heat flux profile.

As peritectic steel grades are widely accepted to be highly complex and are the subject of significant study in the literature [53, 78–80] as well as current industrial interest, this work includes one to study general behavior, with the understanding it is not all encompassing and the intent that further study be included in the future. The peritectic grade in this work is also examined using a lower applied heat flux to simulate more appropriate casting conditions.

With the information this model provides, better choices can be made for taper profiles and casting conditions when attempting to cast grades where complete information may not exist. In addition, it is the first step in demonstrating a transient 3-D model of thermal-mechanical behavior where the correct behavior can be verified in a simplified case where an analytical solution exists, while allowing for extensions to higher dimensional modeling work.

2.4 Model Description

The solidifying steel is envisioned here as a thin plate constrained against bending. Considering that in continuous casting, the shell solidifying in the mold is pushed against the mold by ferrostatic pressure, this domain is representative of a typical vertical section through the wide faces of a slab caster, away from the corner region. With perfect contact against the mold wall and uniform solidification, the domain is simply a thin strip "drilled" through the shell thickness, as shown in Figure 2.1. To compare the effect of steel grade, the thermal and mechanical properties vary with temperature and composition.

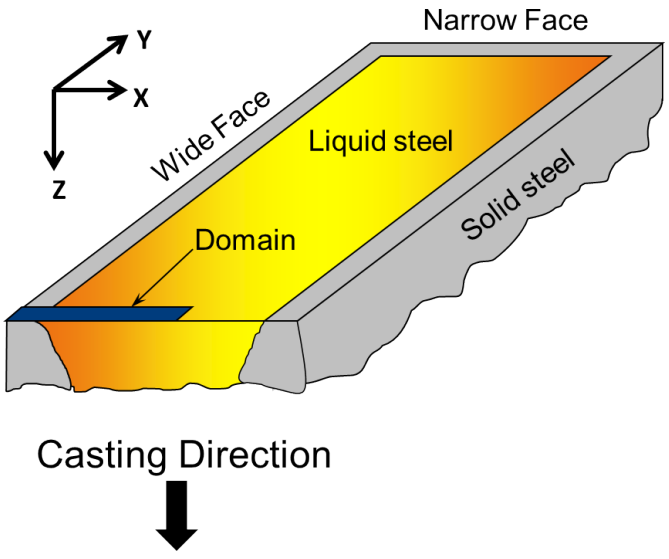

Figure 2.1: Initial solidification of a continuous cast slab showing model domain [81]

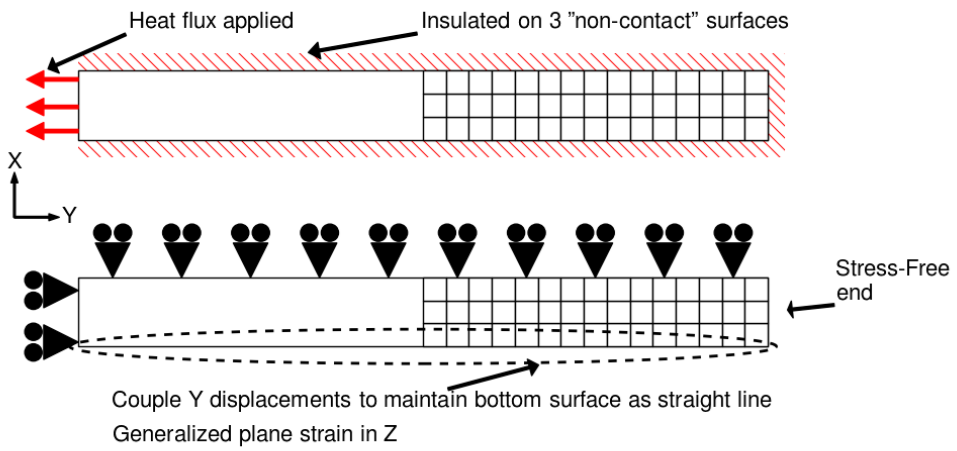

Figure 2.2: Thermal and mechanical boundary conditions

2.4.1 Simulation Domain

The domain is a thin strip of finite elements extending through the thickness of the solidifying steel, as shown in Figure 2.2, and modeled as three rows of 400 finite elements each, 0.1 mm by 0.1 mm as shown in Figure 2.2. A domain length of 40 mm was chosen to investigate shell thicknesses of up to about 16 mm, in order to avoid problems associated with insufficient liquid in the domain [70].

2.4.2 Heat Transfer Model

Assuming fourier law heat conduction, and no internal heat generation or deformation heating (viscious dissipation) effects, the energy equation simplifies to the form of Equation (2.4.1).

$$\rho \frac{DH}{Dt} = \nabla \cdot (k(T) \nabla T) \tag{2.4.1}$$

$$\rho \frac{DH}{Dt} = \rho \frac{\partial H}{\partial T} \frac{DT}{Dt} \tag{2.4.2}$$

where, H is the specific enthalpy, ρ is density, k is thermal conductivity, T is temperature, t is time.

Expansion of the material derivative D term yields independent time temperature and velocity terms:

$$\frac{DT}{Dt} = \frac{\partial T}{\partial t} + V_x \frac{\partial T}{\partial x} + V_y \frac{\partial T}{\partial y} + V_z \frac{\partial T}{\partial z} \tag{2.4.3}$$

where, V_x, V_y, V_z are velocity components in the: x direction perpendicular to the mold surface, y horizontal direction tangential to the mold surface, and z the casting directions.

$$\rho \left(\frac{\partial H(T)}{\partial T} \right) \left(\frac{\partial T}{\partial t} \right) = \frac{\partial}{\partial x} \left(k(T) \frac{\partial T}{\partial x} \right) + \frac{\partial}{\partial y} \left(k(T) \frac{\partial T}{\partial y} \right) = \nabla \cdot (k(T) \nabla T) \tag{2.4.4}$$

$$\rho \frac{\partial H}{\partial t} = \nabla \cdot (k(T) \nabla T) \tag{2.4.5}$$

The continuous casting process is assumed to be operating at steady state with no speed changes, thus the transient term $\frac{\partial T}{\partial t}$ is equal to zero and drops out.

The $2-D$ transient heat conduction given by Equation (2.4.1) is solved for the temperature distribution which is then fed into the mechanical analysis.

The Péclet number

The Péclet number (Pe) given by Equation (2.4.6) is a class of dimensionless numbers [82] relevant in the study of transport phenomena in a continuum. Named after the French physicist Jean Claude Eugène Péclet, it is a representative ratio of the rate of advection to the rate of diffusion. For this model, advection is caused by strand movement at the casting speed, and diffusion is due to the

thermal diffusivity of the steel given by Equation (2.4.7).

$$Pe = \frac{Lu}{\alpha} \tag{2.4.6}$$

where α is thermal diffusivity, L is a characteristic length, u is characteristic velocity,

$$\alpha = \frac{k}{\rho c_p} \tag{2.4.7}$$

thus,

$$Pe = \frac{Lu}{\frac{k}{\rho c_p}} \tag{2.4.8}$$

Substituting Equation (2.4.8) with casting parameters, it becomes:

$$Pe = \frac{LV_C}{\frac{k}{\rho c_p}} \tag{2.4.9}$$

Where L is the distance below the meniscus taken below as mold exit, V_c is the casting speed, k is the thermal conductivity, ρ is the mass density, and C_p is the specific heat capacity.

$$\begin{aligned} V_C &= 3\text{m}\,\text{min}^{-1} & L &= 1\text{m} \\ k &= 33\text{W}\,\text{m}^{-1}\,\text{K} & \rho &= 7500\text{kg}\,\text{m}^{-3} \\ C_p &= 661\text{J}\,\text{kg}^{-1}\,\text{K} & H_f &= 272\text{kJ}\,\text{kg}^{-1} \\ \Delta T &= 500^{\circ}\text{C} \end{aligned}$$

The assumption of advection domination can be seen, even for very short times. Even for casting speeds as low as 1 $\mathrm{m\,min^{-1}}$ by 0.25 seconds, advection is already 3 orders of magnitude greater than conduction by mold exit. This time below meniscus directly translates to the distance below meniscus as a result of the constant casting speed.

$$Pe = \frac{LV_c}{\left(\frac{k}{\rho c_p}\right)} = \frac{1(\mathrm{m}) \times 3(\mathrm{m/min})}{\frac{33(\mathrm{w/m\times K})}{7500(\mathrm{kg/m^3})\times 661(\mathrm{J/kg\times K})}} = 7.5 \times 10^3 \tag{2.4.10}$$

With negligible heat conduction in the casting direction, a Lagrangian domain may be used to analyze the heat transfer in the solidifying shell. This approximation essentially transforms the physical z - direction into a temporal quantity, which is valid while the process remains at steady state.

2.4.3 Stress Model

During initial solidification the thermal-mechanical strains are on the order of only a few percent. Thus, the small strain assumption was adopted for this work. This assumption is supported by previous solidification model results [83].

$$\nabla \cdot \underline{\underline{\sigma}} + b = 0 \tag{2.4.11}$$

The general governing equation for the static problem is given by the force equilibrium balance in Equation (2.4.11), where $\underline{\underline{\sigma}}$ is the second order Cauchy stress tensor, and b is an applied traction.

The out-of-plane (z-direction) stress is characterized by a state of generalized plane strain, where slices are constrained to remain planar by continuity. The lower edge is also constrained to remain planar using an ABAQUS assembly EQN defined in the input file, shown in Appendix B.3.2.

2.4.4 Liquid Treatment

Solidification problems present a unique challenge when it comes to handling the liquid. Liquid that is modeled as too weak (very small yield strength if considered to act like a Bingham plastic [84]) or the presence of too much of it in the domain (not taking full advantage of symmetry or areas of interest) can be difficult to converge if at all. Conversely, liquid that is modeled as too strong (with a high yield strength) will converge but may yield non-physical behavior such as not allowing the solid to shrink as it would naturally.

For this work the liquid region was treated as a perfectly plastic solid [85]. The yield strength for the liquid was chosen to be $\sigma_{yield} = 10$ kPa. This value was chosen to provide a minimum strength needed to aid in convergence without adding inappropriate strength to the liquid based on studies conducted varying this parameter. This behavior is applied any time the mass fraction of the liquid is greater than zero.

2.4.5 Model Setup

The initial temperature of the domain for each case is set 5°C above the grade's liquidus temperature to facilitate comparison between them. This superheat represents a steady fluid flow in the meniscus region and is in line with predicted meniscus temperature profiles reported in the literature [86].

While fluid flow within the liquid pool may create a non-uniform superheat distribution in the melt, the effect is minor when the pouring temperature is close to liquidus temperature; and thus is ignored in this work, which treats superheat in the liquid with simple conduction [64].

Contact with the mold (and resultant frictional effects) have been neglected and the model does not include applied ferrostatic pressure, so in the stress equilibrium equation for this work $b = 0$. Instead the contact interface has been constrained against rigid body motion as shown in Figure 2.2.

To ensure that an accurate solution was being obtained, a mesh resolution study

was conducted to select the mesh refinement level and 400 elements through the thickness were used. Details of this study can be found in Section 2.8.2.

2.5 Heat Flux

In a continuous caster, the instantaneous rate of heat leaving the surface of the solidifying steel shell (heat flux), $\dot{q}_{Inst}$ MW m^{-2}, can be estimated as a function of time down the mold, t, by thermocouples embedded in the mold wall. In addition, the average heat flux leaving the mold $\dot{q}_{Avg}$ MW m^{-2} can be found by measuring the rise in temperature and flow rate of the cooling water, and knowing the surface area of the mold in contact with the steel. This average can be converted to the total heat removed, $\bar{Q}_{Tot}$ MW m^{-2}, during the "dwell time", t_{dwell}, spent by the steel in the mold:

$$\bar{Q}_{Tot} = \dot{q}_{Avg} \times t_{dwell} \tag{2.5.1}$$

where,

$$t_{dwell} = \frac{z_{dwell}}{V_c} \tag{2.5.2}$$

z_{dwell} is working mold length, and V_c is casting speed, assumed to be constant. Measurements of total mold heat removal, $\bar{Q}_{Tot}$, from previous work [68, 69, 69, 87–92] are plotted vs dwell time in Figure 2.3.

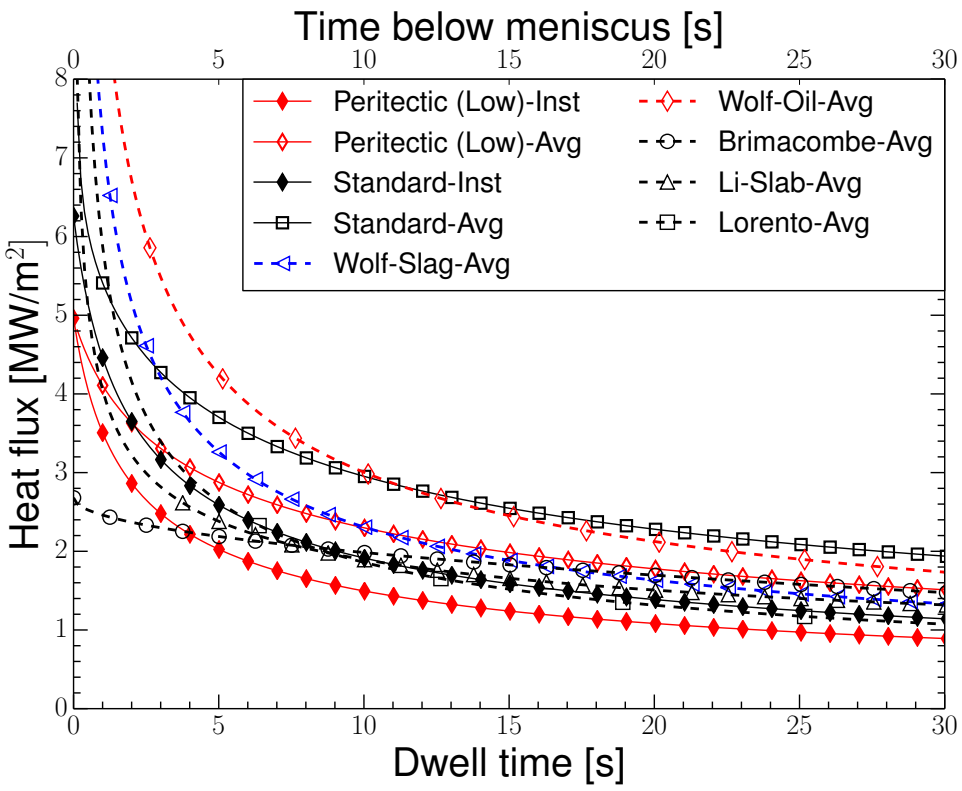

Figure 2.3: Instantaneous and average heat flux curves

It is convenient to express Q_{Tot} in the following form, with time down the mold:

$$Q_{Tot} = -ab^n + a(t+b)^n \tag{2.5.3}$$

The time-average heat flux in the mold then is given as:

$$\bar{\dot{q}}_{Avg} = \frac{Q_{tot}(t_{dwell})}{t_{dwell}} = \bar{\dot{q}}_0 + \frac{a}{t_{dwell}}(t_{dwell}+b)^n \tag{2.5.4}$$

where $\bar{\dot{q}}_0 = -ab^n/t_{dwell}$.

If b=0 , Equation (2.5.4) simplifies to:

$$\bar{\dot{q}}_{Avg} = \bar{\dot{q}}_0 + a(t_{dwell})^{n-1} \tag{2.5.5}$$

The coefficients for the average heat flux profiles in previous measurements are given in Table 2.1, according to this equation form. The corresponding instantaneous heat flux profile down the mold is found by differentiating Equation (2.5.3):

$$\dot{q}_{Inst} = \frac{d}{dt} Q_{Tot} = n \times a(t+b)^{n-1} \tag{2.5.6}$$

By including non-zero b in Equation (2.5.6), this form has a horizontal time-shift that avoids the unrealistic high instantaneous heat flux that is otherwise produced at small times. Thus, the equation form with non-zero b adopted here has the advantage of roughly capturing the linear drop in instantaneous heat flux observed at short times (< 1 s), in strip casting processes [69].

In this work, two different profiles of heat flux down the mold (HF) are used to simulate typical casting conditions, by fitting measurements for "standard" and "low" heat flux conditions to the above equation forms. The total heat removed using these two profiles is given by Equation (2.5.3), and included in Figure 2.3. Coefficients for these two profiles are included in Table 2.1 for the time-average and instantaneous forms, given by Equation (2.5.7) and Equation (2.5.8), respectively.

$$\dot{q}_{standard} = 6.36(t+1.032)^{-0.5} \tag{2.5.7}$$

$$\dot{q}_{low} = 4.96(t+1)^{-0.5} \tag{2.5.8}$$

The Standard-HF curve, Equation (2.5.7), was found by fitting all of the data points in Figure 2.4. The Low-HF curve, Equation (2.5.8), was generated by excluding the higher HF data of Duvuuri [92]. This curve is used for peritectic

steels, which have lower heat flux, owing to their deeper oscillation marks, surface depressions [93], and usually higher slag crystallization temperatures [94]. Peritectic steels are difficult to cast, due to the mechanical behavior during the peritectic transformation [53, 55]; lowering heat removal is one method to lessen castability problems, such as longitudinal cracks and depressions [54].

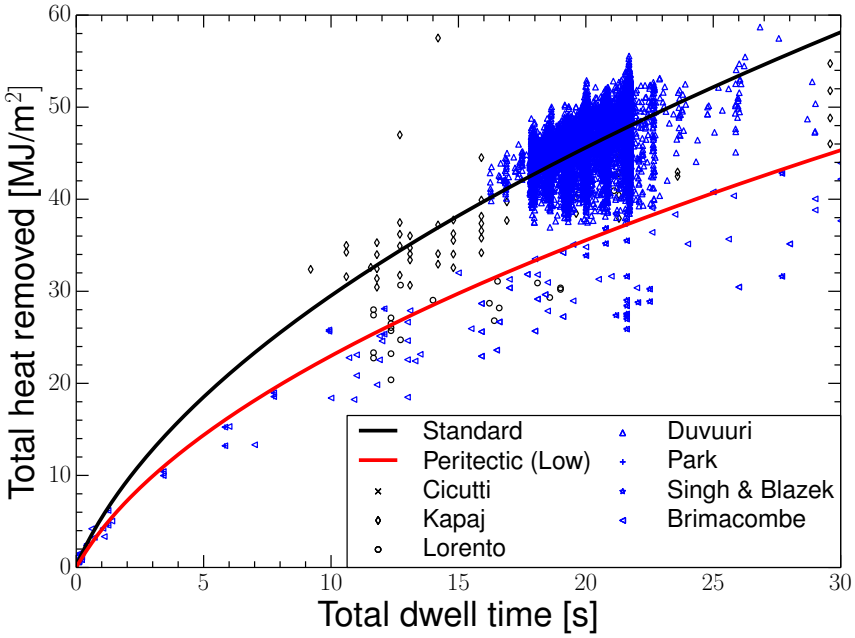

Figure 2.4: Measured heat removed and fitted curves

Figure 2.3 compares average heat flux formulas from previous literature with those generated for the current work. The standard and low heat flux curves, plotted using solid lines in black and red respectively. The corresponding instantaneous heat flux curves are also included, shown with filled diamonds. Note that at any given time down the mold, the instantaneous heat flux is always significantly less than that on the time-average curve, at that dwell time. This is a natural consequence of a function that decreases with time.

Table 2.1: Heat flux profile coefficients

Profile	q_0	a	b	n
Wolf (slag)	-	7.3	-	0.5
Wolf (oil)	-	9.5	-	0.5
Li (billet)	-	9.57	-	0.496
Li (slab)	-	4.05	-	0.67
Lorento	-	5.88	-	0.5
Brimacombe	2.68	-0.22	-	0.5
This work (standard)	-	12.72	1.032	0.5
This work (low)	-	9.92	1	0.5

2.6 Steel Grades and Phase Fractions

Four steel grades were chosen for this work: 0.003%C (ULC), 0.04%C (LC), 0.13%C (P), and 0.47%C (HC) steel. The composition for each grade is shown in Table 2.2 and the transition temperatures are shown in Table 2.3. These grades were selected to capture the range of different phase-dependent behavior of plain-carbon steel grades. Other alloying elements were selected to make the grades typical of these commercially-produced steels.

The pseudo-binary Iron-Carbon phase diagram shown in Figure 2.5 consists of a linearization of 15 points calculated according to the equations of Kagawa and Okamoto as a function of alloying element composition [57]. The lever rule is used to calculate phase fractions in each two-phase region, and a lever rule for ternary systems is used in the three-phase region.

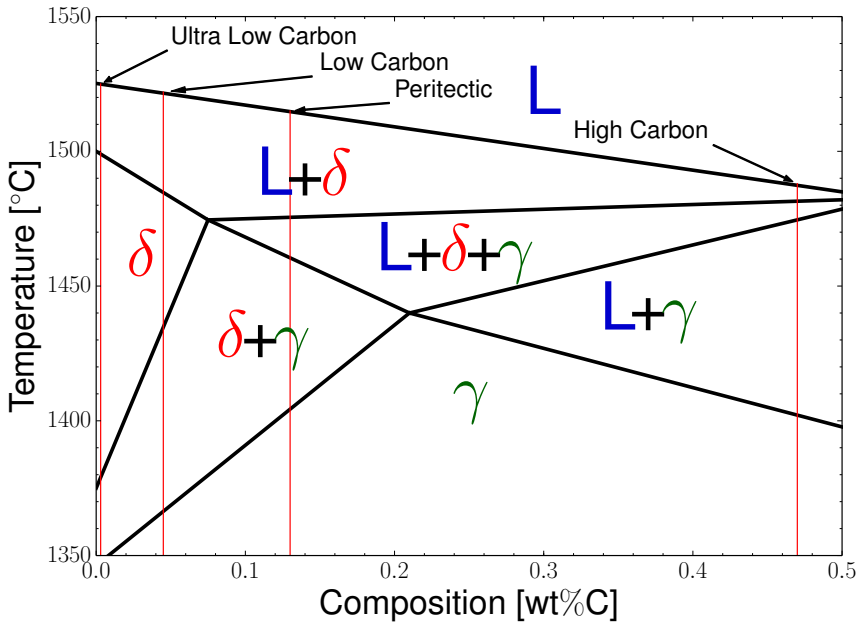

Figure 2.5: Pseudo-binary iron-carbon phase diagram for 0.04%C steel showing approximate solidification path for four steel grades investigated

The described methods provide the mass fractions of liquid, δ-ferrite, and austenite for each grades. Figure 2.6 shows the phase fractions thus generated as a function of temperature for each of the steels simulated. As the Figure indicates, the liquid fraction decreases parabolically as the steel cools from its liquidus temperature, this behavior agrees with a more sophisticated microsegregation model developed from measurements and described in the literature [95].

These grades were selected to capture the different possible phase-dependent behavior of steel grades produced by continuous casters. Specifically they differ in their phase fraction cooling history, for example, the ultra-low and the low carbon grades contains primary δ-ferrite, while the high carbon grade has primary austenite. The ULC and LC grades transition fully into δ-ferrite from liquid and have a range of approximately 100°C before transitioning into austenite, the primary difference between the two being the much shorter transition regions for the ULC. The peritectic grade passes through the so-called "Peritectic Triangle" and experiences both the peritectic reaction and transformation strongly affecting its solidification behavior.

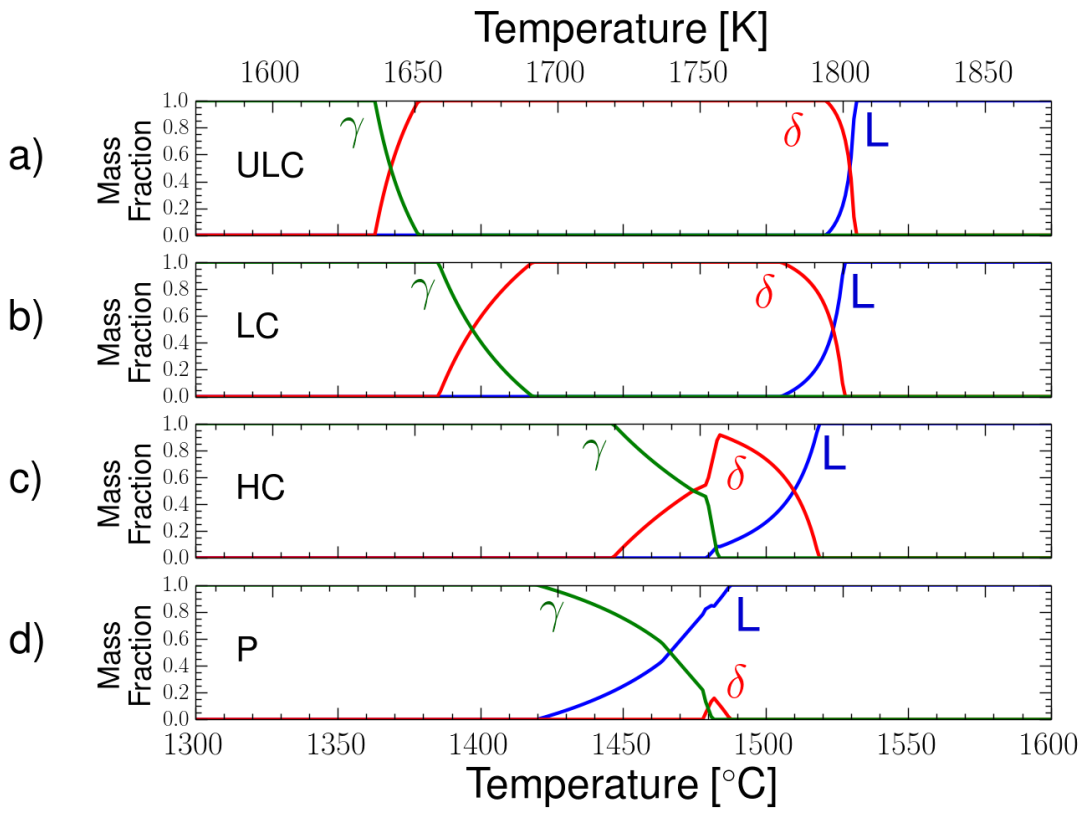

Figure 2.6: Phase fractions for four steel grades investigated: a) Ultra-Low carbon b) Low carbon c) Peritectic d) High carbon)

Table 2.2: Steel grade compositions [% wt.]

Grade	C	Al	Cr	Cu	Mn	Ni	P	S	Si	Ti
High Carbon	0.470	0.04	0.01	0.01	0.75	0.01	0.01	0.01	0.220	0.05
Peritectic	0.130	0.04	0.01	0.01	0.50	0.01	0.01	0.01	0.015	0.05
Low Carbon	0.040	0.04	0.01	0.01	0.20	0.01	0.01	0.01	0.020	0.05
Ultra-Low Carbon	0.003	0.04	0.01	0.01	0.08	0.01	0.01	0.01	0.005	0.05

Table 2.3: Steel grade transition temperatures [°C]

Grade	Liquidus	Solidus	Liquidus-Solidus	δ Start	δ End	γ Start
High Carbon	1488	1419	69	1482	1478	1419
Peritectic	1519	1479	40	1484	1479	1446
Low Carbon	1528	1505	23	1505	1419	1385
Ultra-Low Carbon	1532	1521	11	1521	1379	1363

The transition temperatures and phase fractions for the four grades match well with the CON1D software package [96] and are similar to the output from the microsegregation model CKSEG [95], with the exception of the high carbon steel.

The HC grade chosen experiences primarily a liquid to austenite transition, however, the particular grade chosen also briefly passes through the peritectic triangle. In the case of the high carbon steel grade, the model predicts a smaller appearance of δ-ferrite presence prior to the austenite transition, compared to CKSEG.

For the purposes of this work, examining the difference between general phase fraction cooling histories, this difference is negligible.

2.7 Material Properties

2.7.1 Enthalpy and Specific Heat Capacity

The specific enthalpy, H ($\mathrm{J\,kg^{-1}}$), curve used to relate heat content and temperature in this work, is obtained by integrating the specific heat curve C_P fitted from measured data complied by Harste [97] as given in Equations (2.7.2) to (2.7.4)

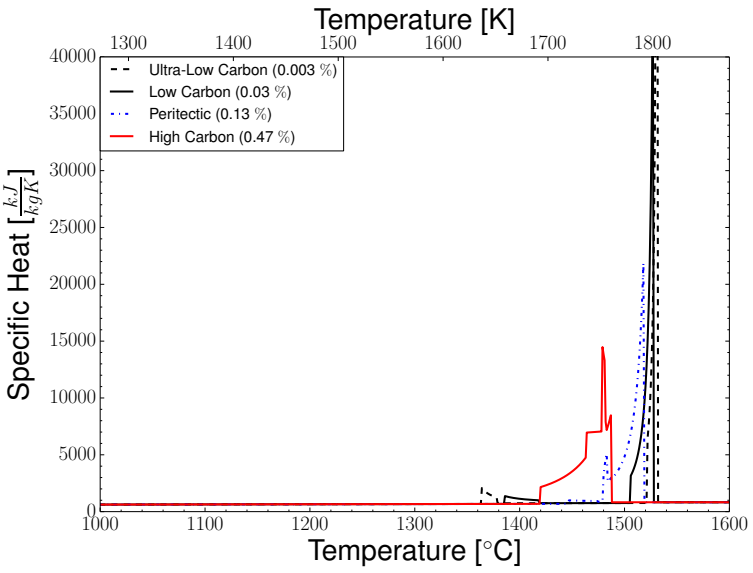

Figure 2.7: Temperature and grade dependent specific heat capacity

and (2.7.7). Figure 2.7 shows the specific heat capacity, and Figure 2.8 shows the enthalpy for the four grades examined in this work. The enthalpy values used are weighted according to the fraction presence of each phase as shown in Equation (2.7.1). Values vary based on temperature and the phase of the steel. It is worth noting that while the latent heats for each of the grades is very similar, it is not identical, and the distribution of release based on temperature is also not the same. The equations used for each phase [97] are shown in Equations (2.7.2) to (2.7.4) and (2.7.7).

$$H[kJ/Kg] = H_L f_L + H_\delta f_\delta + H_\gamma f_\gamma + H_\alpha f_\alpha \tag{2.7.1}$$

Where temperature T is given in Kelvin.

$$H_L = 824.6T - 104642.3 + \Delta H^l_{mix} \tag{2.7.2}$$

$$H_\delta = 0.8872T^2 + 441.39T + 50882.3 \tag{2.7.3}$$

$$H_\gamma = 0.07489T^2 + 429.849T + 93453.72 + \Delta H^\gamma_{mix} \tag{2.7.4}$$

where,

$$\Delta H^{l}_{mix} = 18125(\%C) + 1966120\frac{(\%C)^2}{43.839(\%C) + 1201.1} \tag{2.7.5}$$

$$\Delta H^{\gamma}_{mix} = 36601(\%C) + 1907930\frac{(\%C)^2}{43.839(\%C) + 1201.1} \tag{2.7.6}$$

$$H_{\alpha} = \begin{cases} 5188T^{-1} - 86 + 0.505T & \\ \quad -6.55 \times 10^{-5}T^2 + 1.5 \times 10^{-7}T^3 & T \leq 800 \\ 5188T^{-1} - 86 + 0.505T & \\ \quad -6.55 \times 10^{-5}T^2 + 1.5 \times 10^{-7}T^3 & 800 < T \leq 1000 \\ 5188T^{-1} - 86 + 0.505T & \\ \quad -6.55 \times 10^{-5}T^2 + 1.5 \times 10^{-7}T^3 & 1000 < T \leq 1042 \\ 5188T^{-1} - 86 + 0.505T & \\ \quad -6.55 \times 10^{-5}T^2 + 1.5 \times 10^{-7}T^3 & 1042 < T \leq 1060 \\ -10.068T + 2.9934 \times 10^{-3}T^2 & \\ \quad -5.21766 \times 10^{6}T^{-1} + 12.822 & 1060 < T \leq 1184 \end{cases} \tag{2.7.7}$$

2.7.2 Thermal Conductivity

The temperature and grade dependent conductivity functions for plain carbon steel phases is fitted from measured data compiled by Harste [97] and is given by Equations (2.7.8) and (2.7.11). Figure 2.8 shows the conductivity for the four steel grades studied. The conductivity, k ($\mathrm{W\,m^{-1}\,K}$), increases linearly through the mushy zone to the liquid by a factor of 6.5 to partly account for the effect of convection due to flow in the liquid steel pool [98]. A small difference in shell thickness is noted when this is not included, but for the purposes of this work is negligible.

$$k_l = 39.0 \tag{2.7.8}$$

$$k_\delta = (21.6 + 0.00835T)(1 - F_1(C\%^{F_2})) \tag{2.7.9}$$

$$k_\gamma = 20.14 + 0.00931T \tag{2.7.10}$$

where,

$$F_1 = 0.425 - 0.0004385T \tag{2.7.11}$$

$$F_2 = 0.209 - 0.00109T \tag{2.7.12}$$

2.7.3 Mass Density and Thermal Linear Expansion

Mass density, ρ ($(\mathrm{kg\,m^{-3}})$), is calculated by weighted phase fraction of all of the phases given by Equation (2.7.15). Experimental data taken from the work of Jablonka et al. [62] and compiled by Jimbo and Cramb [99]. The thermal linear-expansion function is obtained from solid-phase density measurements complied by Harste [97] and liquid density measurements by Jimbo and Cramb [99].

A simple mixture rule is applied to obtain the overall density from the values of the different phases. Figure 2.8 shows the density and thermal linear-expansion curves for the four grades examined, choosing the reference temperature, T_0, to be the 1507°C for all grades in this work [18].

$$\alpha_L = \sqrt[3]{\frac{\rho_{T_0}}{\rho_T}} - 1 \tag{2.7.13}$$

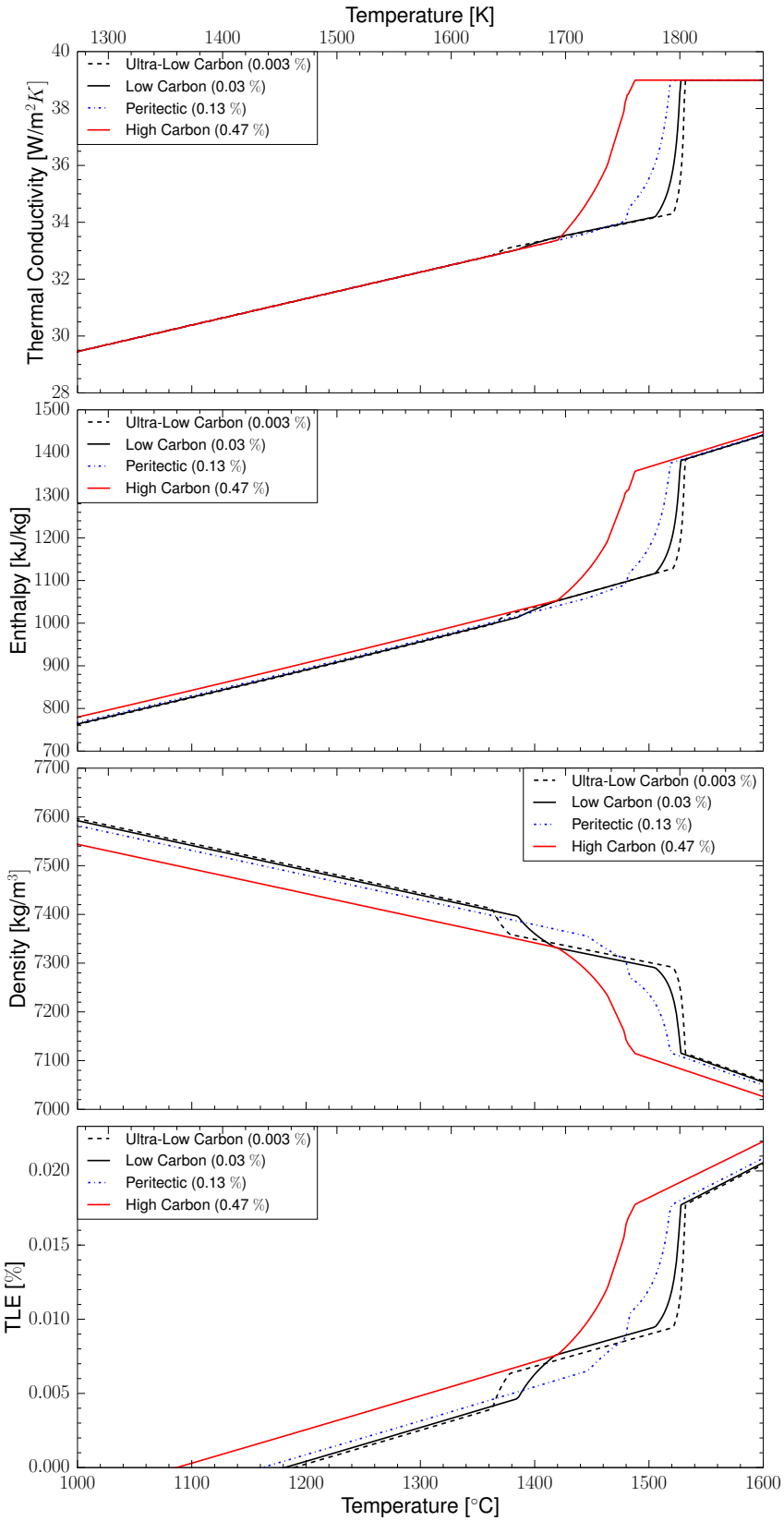

Figure 2.8: Temperature-dependent properties of four steel grades investigated: a) Thermal conductivity b) Enthalpy c)Density d) Thermal linear expansion

$$\rho_l = 7100 - 73.2C_C - (0.828 - 0.0874C_C)(T - 1550) \quad (2.7.14a)$$

$$\rho_\delta = \frac{100(8011 - 0.47T)}{(100 - C_C)(1 + 0.013C_C)^3} \quad (2.7.14b)$$

$$\rho_\gamma = \frac{100(8106 - 0.51T)}{(100 - C_C)(1 + 0.008C_C)^3} \quad (2.7.14c)$$

$$\rho_\alpha = 7881 - 0.324T - 3 \times 10^{-5}T^2 \quad (2.7.14d)$$

$$\rho_T[\mathrm{kg\,m^{-3}}] = \rho_l f_l + \rho_\delta f_\delta + \rho_\gamma f_\gamma + \rho_\alpha f_\alpha \quad (2.7.15)$$

Where α_L is the Thermal Linear Expansion coefficient and the density ρ_{T_0} is the density at the reference temperature T_0. For this work ρ_{T_0} is taken to be 7400 $\mathrm{kg\,m^{-3}}$.

2.7.4 Elastic Properties

The temperature-dependent elastic-modulus curve used in this model is a stepwise linear fit of measurements by Mizukami et al. [100], given in Figure 2.9.

The liquid is modeled as a weak perfectly plastic solid. The elastic modulus of the liquid region was given the value of 0.01MPa, and the Poisson ratio is constant at $\nu = 0.3$. The measured Poisson ratio that approaches 0.5 at high temperatures is achieved with this model, by considering the large extent of incompressible creep strain ($\nu = 0.5$) that accompanies the elastic strain during the test [101]. Incorrectly incorporating part of the volume conserved plastic behavior, where $\nu = 0.5$, into the elastic has been found to be likely to cause numerical difficulty for the solver [18].

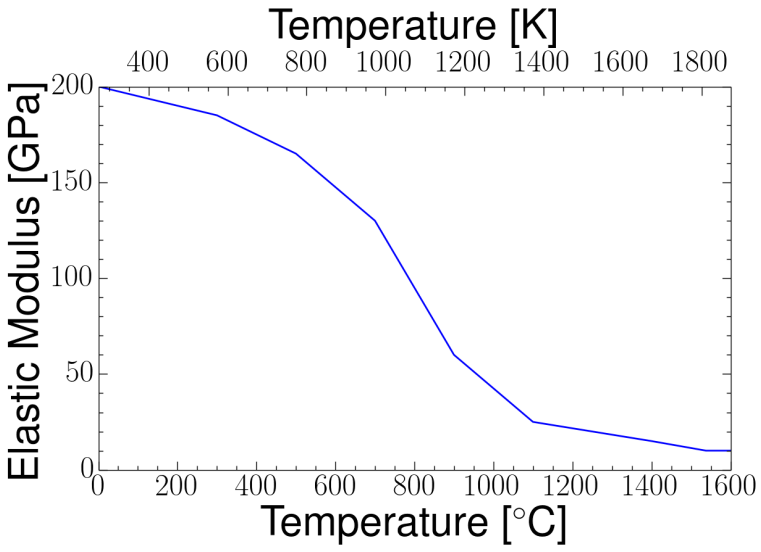

Figure 2.9: Temperature-dependent elastic modulus of steel

2.7.5 Constitutive Models

Two constitutive models relating the stress-strain relationship are utilized in this work. These equations were developed to match tensile-test measurements of Wray [102] and creep-test data of Suzuki et al [47]. The details of these two models can be found in [103] and [104] respectively.

The ferrite and austenite phases are not of comparable strength. Ferrite is approximately an order of magnitude weaker than austenite of the same temperature, because of this a weighted mixture rule is not appropriate in regions with the much weaker phase when the softer material dominates the net mechanical behavior. In previous works where these two constitutive equations were utilized, Equation (2.7.17) was in effect when there was less than 10% of either ferrite phase, otherwise Equation (2.7.16) was used. This work also uses this method. Improving upon this transition method is left for future work.

Two different constitutive equations are used to model the behavior of solidifying steel. Equation (2.7.16) is the Zhu Modified Power law [103] and is used for

ferrite.

$$\dot{\bar{\epsilon}}_{in-\delta}[1/s] = 0.1F_\delta|F_\delta|^{n-1} \tag{2.7.16}$$

where,

$$\begin{aligned}
F_\delta &= \frac{C\overline{\sigma}}{f_C(\frac{T(K)}{300})^{-5.52}(1+1000|\bar{\epsilon}_{in}|)^m} \\
f_C &= 1.3678 \times 10^4 C_C^{-5.56\times10^{-2}} \\
m &= -9.4156 \times 10^{-5}T(K) + 0.349501 \\
n &= (1.617 \times 10^{-4}T(K) - 0.06166)^{-1}
\end{aligned}$$

C represents the sign on the 3 dimensional stress tensor [105], and C_C is the wt.% carbon.

Equation Equation (2.7.17) is the Kozlowski model III [104] which is used for austenite.

$$\dot{\bar{\epsilon}}_{in-\gamma}[1/s] = f_C|F_\gamma|^{f_3-1}F_\gamma exp(\frac{-4.465\times10^4}{T(K)}) \tag{2.7.17}$$

where,

$$\begin{aligned}
F_\gamma &= C\overline{\sigma} - f_1\epsilon_{in}|\epsilon_{in}|^{f_2-1} \\
f_1 &= 130.5 - 5.128 \times 10^{-3}T(K) \\
f_2 &= -0.6289 + 1.114 \times 10^{-3}T(K) \\
f_3 &= 8.132 - 1.54 \times 10^{-3}T(K) \\
f_C &= 4.655 \times 10^4 + 7.14 \times 10^4 C_C + 1.2 \times 10^5 C_C^2
\end{aligned}$$

Table 2.4: Properties used in the Weiner and Boley test problem

Property	Value	Unit
Thermal Conductivity	33	$\mathrm{W\,m^{-1}\,K}$
Density	7500	$\mathrm{kg\,m^{-3}}$
Young"s Modulus (Solid)	4000	MPa
Young"s Modulus (liquid)	1400	MPa
Poisson"s Ratio	0.3	-
Thermal Expansion	$2x10^{-5}$	$\mathrm{K^{-1}}$
Pour Temperature	1769	K
Fixed Wall Temperature	1273	K
Liquidus Temperature	1768.1	K
Solidification Temperature	1768	K
Solidus Temperature	1767.9	K
Latent Heat	272	$\mathrm{kJ\,kg^{-1}}$
Specific Heat	661	$\mathrm{J\,kg^{-1}\,K}$

2.8 Model Validation

Model validation requires a test problem with a known solution. For this work, the analytical solution to the thermal stress model derived by Weiner and Boley [106] was used as well as a mesh resolution study to verify convergence the results.

2.8.1 Weiner and Boley Plate Solidification

The semi-infinite pure material elastic perfectly plastic plate domain is constrained against bending but otherwise free to shrink. We use it here as an ideal problem to validate our solidification stress model. The constants and parameters used to approximate the behavior of our problem for this simplified validation problem can be found in Table 2.4. For the Weiner and Boley model a mushy zone is included just enough for numerical stability, and is approximately negligible.

Results of the numerical and analytical solution are shown in Figure 2.10, the temperature and stress are plotted along the lower edge of the domain starting from the chilled end towards the free end. As expected, the temperature in the liquid remains constant, while the temperature distribution through the solid

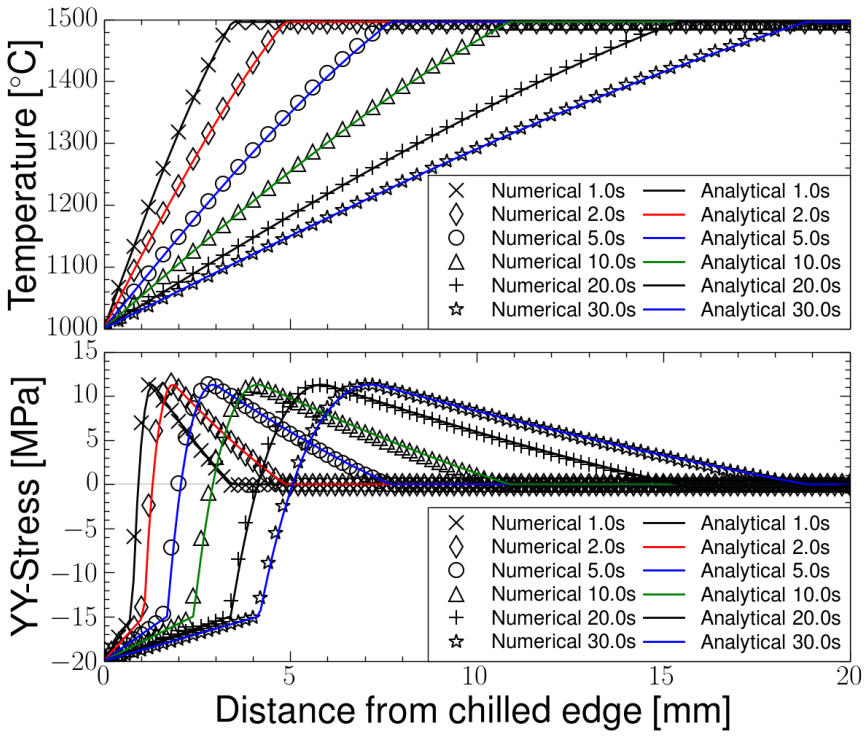

Figure 2.10: Comparison of Weiner & Boley and ABAQUS predicted temperature and stress distributions through the shell

decreases with time. The stress profile shows behavior that indicates compression at the surface moving towards tension at the solidification front.

The surface of the shell is quenched immediately. This causes the domain to shrink locally. Initially the domain is allowed to shrink freely, unconstrained by the lack of strength in the primarily liquid domain. The liquid has negligible strength, and thus carries no stress. As time progresses, the rest of the domain cools and attempts to shrink. Relative to the solidified surface, the interior of the domain is still weaker and as it attempts to shrink remains opposed by the stronger material at the surface. This tends to generate compression at the surface, and to maintain equilibrium, generates subsurface tension.

Comparing the results shown in Figure 2.10, the numerical results match the analytical solution. Thus, the methodology is validated, with 400 elements, the same mesh density used in the simulations in the investigation of grade effect.

2.8.2 Mesh Resolution

A mesh study was conducted to verify that the model was converging to a proper solution, changing only the number of elements through the solidification direction (x). The domain width was chosen to maintain 3 elements through the thickness and an aspect ratio of 1. (i.e. the 10-elements case has 4mm square elements, giving a 12mm wide domain). Figure 2.11 shows results for 6 different mesh refinements after 10s of solidification; these results indicate that while 1, 2.5, and 4 mm elements can accurately reproduce the temperature history, shown in Figure 2.11(a), a much more refined mesh is necessary to properly resolve the stress and strain behavior, shown in Figure 2.11(b-d).

While 4mm elements capture the behavior of compression at the surface, and tension towards the solidification front, the problem becomes the low number of elements through the mushy zone. The size of the mushy zone is strongly grade dependent and can vary by almost an order of magnitude. For the LC steel shown, the mushy zone at 10s is only 2mm wide and with elements close to that size, the mushy zone could be contained within a single element.

The phase transformation regions raise similar problems and are often thinner than the mushy zone. For the LC steel, the δ-ferrite to austenite region is 1 mm wide, and the 1mm elements just barely capture the details. The inelastic strain, shown in Figure 2.11(d), demonstrates that 4 mm elements capture the general behavior in the austenite near the surface, but indicate the presence of strain throughout the mushy zone and also into the liquid.

For all of the reasons discussed, element size selection is extremely important for a solidification model. It becomes notably more important when interested in the solidification front or any phase transformation region

For this work an element size of 0.1 mm was chosen (400 elements through the 40 mm length) providing a balance between speed of calculation and capture of relevant phenomena.

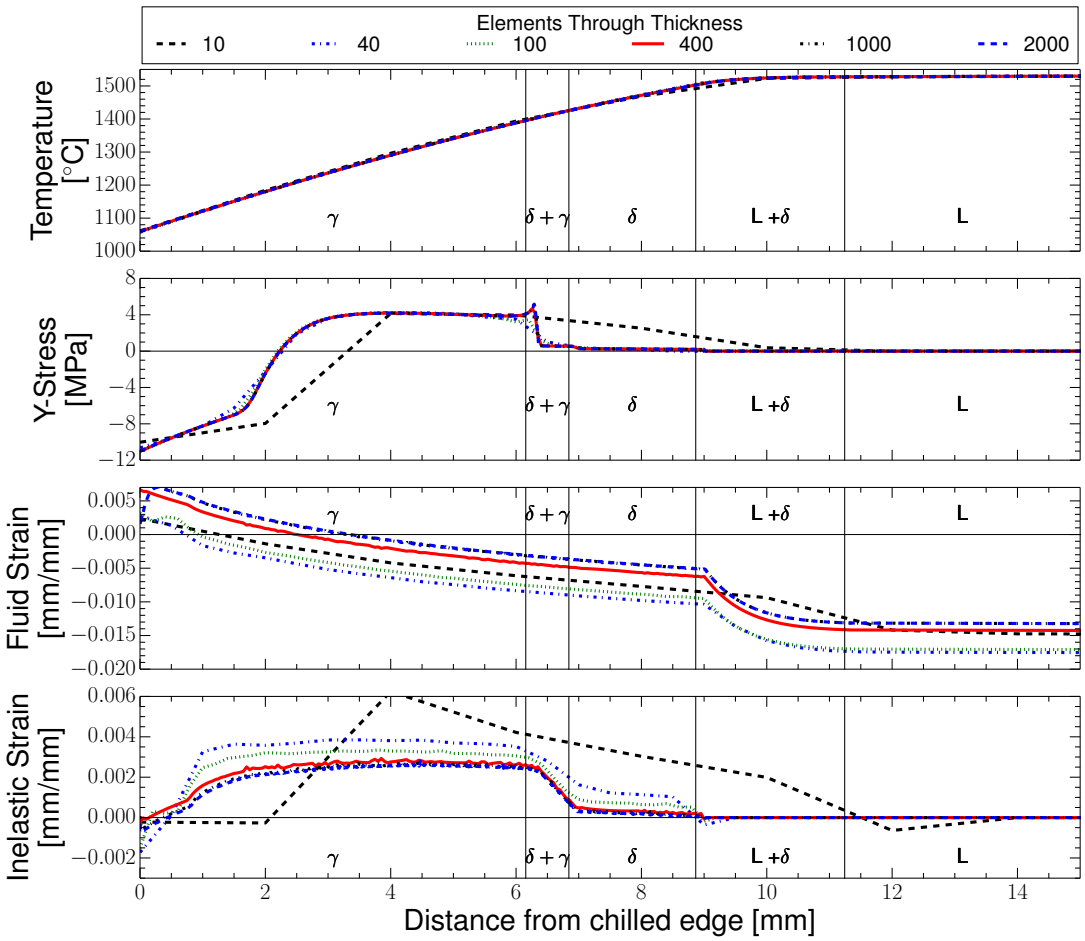

Figure 2.11: Mesh study results through shell thickness for low carbon steel (0.045%C)—10s below meniscus a) Temperature b) Y-Stress c) Fluid Strain d) Inelastic Strain

2.9 Solution Method & Details

The governing equations are solved incrementally using the finite-element method [107] in ABAQUS/Standard [108] (implicit). Analysis was performed in two separate steps consisting of the 30s heat transfer analysis, followed by the 30s mechanical analysis, with the heat transfer solution as input for each time increment of the mechanical step. While this neglects the nonlinear coupling between the mechanical and thermal solutions, the "one-way coupled" method, has been shown to be reasonable in regions of uniform heat transfer [109] and is appropriate for our simplified case. Details of the numerical method are provided elsewhere [64, 105].

DCC2D4 4-node linear diffusive heat transfer elements were used for the thermal problem and CPEG4H 4-node bilinear quadrilateral elements for the stress. The time step size was allowed to vary from 0.00001s to 1s, controlled by ABAQUS, with a maximum temperature change per increment of 10°C. Output was requested at 0.05s intervals. Each grade simulation required about one hr wall-clock time on one core of a Dell Precision T7600 workstation with 2 Intel Xeon 1.8GHz quad-core processors and 64GB of DDR3 SDRAM. The Peritectic and Ultra-Low Carbon grades took slightly longer than the others due to the abrupt changes in phase fraction visible in Figure 2.6

2.10 Results and Discussion

2.10.1 General Solidification Behavior

As discussed in the results of the test problem, during soldification the shell wants to shrink. Left unconstrained the shell would warp into a shape like that shown in Figure 2.12, this would generate tension at the surface and compression towards the solidification front. In reality, forcing the shell not to warp and to maintain straight edges for symmetry results in compression at the surface and tension towards the solidification front - this is the true behavior of a solidifying plate

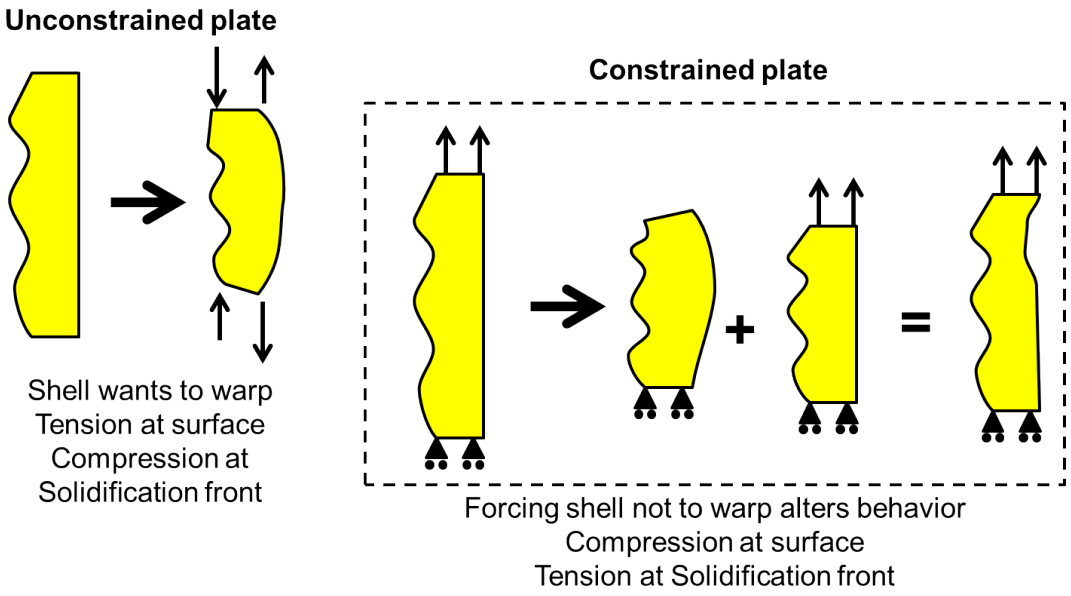

Figure 2.12: Behavior of unconstrained and constrained solidifying plates

and within a steel caster.

2.10.2 Typical Results for LC Steel Behavior

Typical results for LC steel are used to show the thermal-mechanical behavior predicted by the model. Figure 2.13 shows the temperature, thermal strain, fluid strain, and inelastic strain. The stress results were already presented in Figure 2.11, with the contour shown in Figure 2.14. A breakdown of the total strain into its components of elastic, thermal, fluid, and inelastic strain profiles is given in Figure 2.15. Stress and strain components are shown in the direction tangential to the surface (y-y component).

Shell Growth and Temperature

The temperature contours show that shell growth, s, follows the well-known $s = k\sqrt{t}$ behavior, where t is the time of solidification, and k is some empirically determined value corresponding to situation specific solidification conditions. At 30 s, the low carbon steel has a total shell thickness of about 16 mm with the

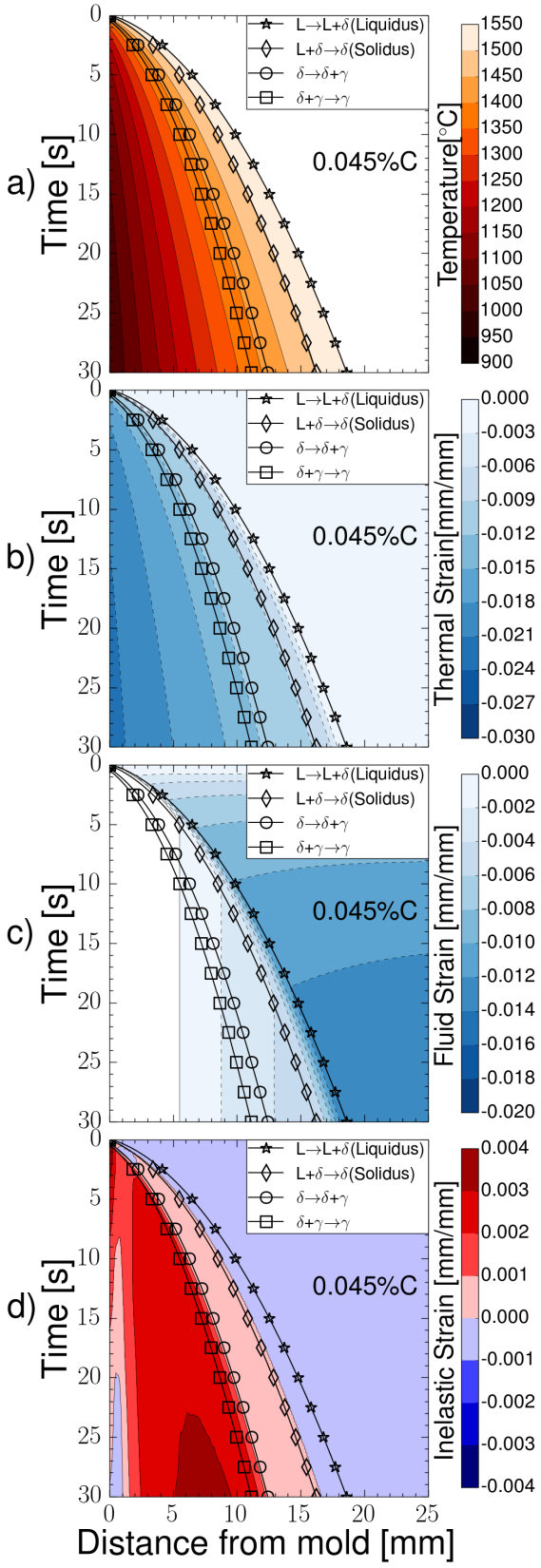

Figure 2.13: 0.045%C low carbon steel contours: a) Temperature, b) Thermal strain, c) Fluid strain, d) Inelastic strain

mushy zone extending just 3 mm beyond that. The austenite (γ) portion of the shell is slightly more than 10 mm thick, extending inwards from the surface; the δ-ferrite region is about 3.5 mm thick. The $\delta \rightarrow \gamma$ transition region remains only about 1 mm for the entire simulation.

Stress

Compression develops at the surface and tension is generated at the solidification front, as discussed previously. Compression at the surface increases with time, as the entire shell attempts to further shrink and is opposed by the growing region of colder stronger steel.

Elastic Strain

Elastic strain is directly proportional to the stress and displays compression at the surface with tension toward the solidification front. Most of the elastic strain are carried in the austenite, with very little observed in the δ-ferrite region due to the lower strength of the phase. Elastic strains are always less than about 0.05%, which is very small relative to the other strains; this is visible in Figure 2.15.

Thermal Strain

The thermal strain dominates the mechanical behavior, going further into compression with time, i.e. decrease in temperature. This behavior is accentuated through transition regions, where the changes in density are most abrupt and drive negative thermal expansion; the largest being the initial contraction of liquid to solid transformation.

Fluid Strain

The fluid strain (also called "flow strain" [64]) is the inelastic strain generated in the liquid, which is caused by shear (fluid flow) during liquid shrinkage. This

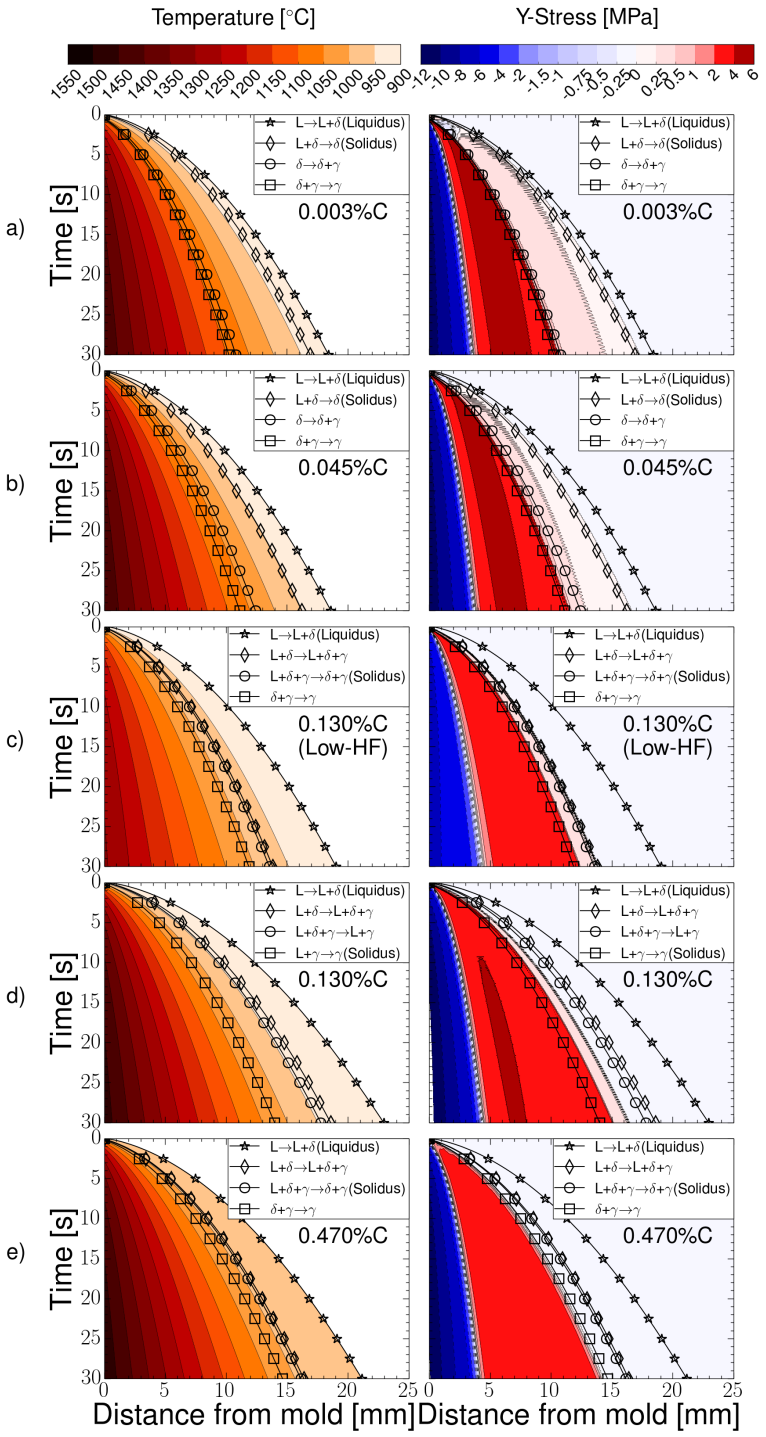

Figure 2.14: Temperature and Y-Stress contours for five casting situations investigated: a) Ultra-Low carbon steel with Standard HF, b) Low carbon steel with Standard HF, c) Peritectic steel with Standard HF, d) Peritectic steel with Low HF, e) High carbon steel with Standard HF

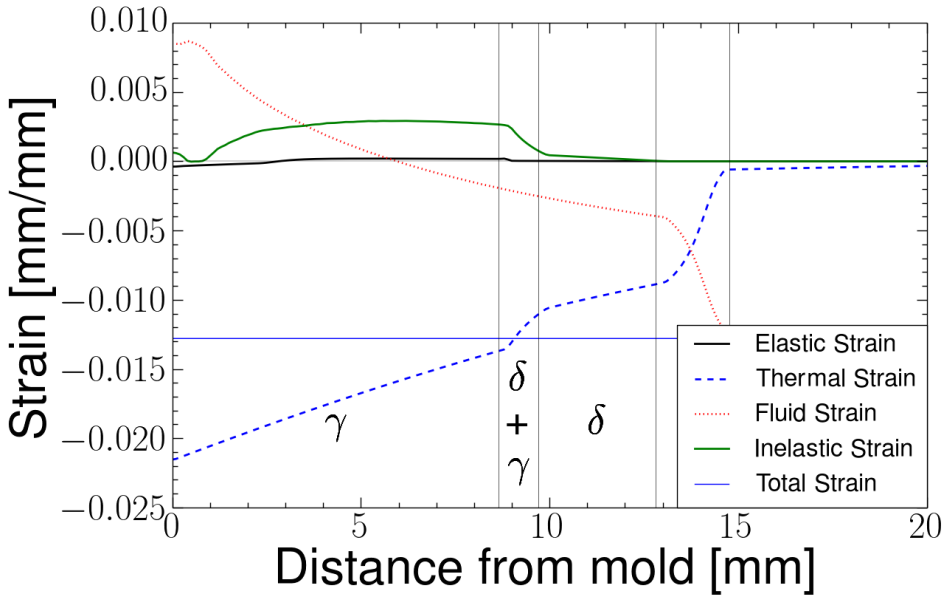

Figure 2.15: Typical strain distribution through the shell thickness for Low Carbon Steel (0.045%C) —10s below meniscus

strain represents a measure of liquid feeding. Feeding difficulties can lead to porosity between dendrites [110] if the liquid is unable to flow to fill the interdendritic spaces. After solidification is complete, the fluid strain remains constant with time, as any further inelastic strain builds up in the solid phases.

Within the liquid region, the fluid strain is always compressive, which indicates flow out of the region. This compression is a real consequence of the constraints on the domain, which require the upper and lower edges to remain parallel; shrinkage of the solid portion of the domain squeezes the liquid portion of the domain as well, causing liquid to flow outwards away from the solidification front. In addition to generating fluid strain, this squeezing initially causes the length of the domain to increase rapidly (as the rapid surface cooling causes shrinkage of the strong cold shell at the surface, which dominates the strength and behavior of the entire domain). Later, the domain length shrinks slowly, as the surface cools and shrinks more slowly than the interior.

Inelastic Strain

Low levels of tensile inelastic strain begin to develop in the δ-ferrite region and increases drastically during the transition to austenite. At the surface, the rapid initial solidification and very thin mushy zone causes more compressive thermal strain, tensile stress and tensile inelastic strain. In the case of the low carbon steel shown, this tensile inelastic strain persists at the surface, even after 10 s. Inelastic strain development in the fluid prior to complete solidification appears to be insignificant compared to the total inelastic strain.

Total Strain

Driven largely by the thermal strain, the total strain becomes increasingly compressive during solidification as the domain cools and shrinks. The total strain naturally remains constant through the shell thickness and accompanying liquid in the domain, as required for a plate that is constrained from bending. Total strain is the important quantity to match when designing mold taper.

2.10.3 The Grade Effect

The temperature, stress, and strain results of the four different steel grades are compared in Figures 2.14 and 2.16 to 2.19. The peritectic steel grade was simulated with both the same "higher" heat flux as the others, and with the low heat flux, more typical of this grade in plant practice.

Shell Growth and Temperature

Comparing the peritectic steel results in Figure 2.14 c) and d) shows that increasing heat flux causes the shell thickness to increase by about 20% (represented by corresponding increases in both the solidus and liquidus contour positions). At the same time, the higher heat flux also causes a lower surface temperature, owing to the steeper temperature gradient, as shown in Figure 2.19.

Increasing carbon content causes increased thickness of the mushy zone, according to the increasing temperature range between the liquidus and solidus temperatures, as shown in the left side of Figure 2.14. With the same superheat, the liquid temperature decreases with increasing carbon content, as shown in the top right of Figure 2.19, so the temperature profiles of the four grades become correspondingly lower.

The effect of steel grade on shell thickness is complicated, because it depends on the thermal properties, the heat flux, and the definition of shell thickness. Except for the peritectic steel, increasing the carbon content increases the liquidus thickness and decreases the solidus thickness, due to the increase in mushy zone thickness.

Stress

For all four steels, the general stress profile of compression at the surface increasing to tension near the solidification and down to zero in the liquid, as shown in Figure 2.18. At early times in ULC and LC steels, however, a brief tensile peak appears at the surface, due to the rapid cooling and shrinkage, as shown in Figure 2.18(b). This generates a corresponding very mild compression region inside the δ-ferrite for a brief period, which can be seen in the top left of Figure 15 (a-b) stress frames. As time increases beyond 2 s, surface stress becomes compressive in all steel grades. As the steel continues to cool and strengthen, the magnitude of this surface compression increases. For the same reason, decreasing the heat flux (in the peritectic steel) causes higher temperatures and lower absolute stress levels, both at the surface and in the interior.

Figure 2.14 shows low stress in the δ-ferrite whenever that phase appears, which is due to its low strength and inability to carry any significant load. Moving towards the left, a sharp increase in strength from δ-ferrite to austenite is observed, which is accompanied by a pointed peak. Although this peak is not a numerical error, it is an artifact that disappears when the phase transition occurs over a

wide temperature range. Naturally, this peak is missing from high carbon steel, which has no delta phase, so its stress transition is smooth across the austenite near the solidification front.

The sharp increase in strength from δ-ferrite to austenite causes a pointed peak to appear in the stress profile. Although this peak is not a numerical error, it is an artifact that disappears when the phase transition occurs over a temperature range. Naturally, this peak is missing from high carbon steel, which has no δ phase, so the stress peak is smooth.

Strain Results

Contours of the thermal, fluid, and inelastic strain components are compared for the four steels in Figure 2.16. The dominant component, thermal strain, increases in magnitude as temperature decreases. Thus, the greatest magnitude thermal strain is found at the surface, where it increases with decreasing carbon content.

The fluid strain evolution in all grades is similar to that discussed for LC steel previously. Fluid strain is always negative, indicating shrinkage. The greatest magnitude fluid strain is observed in the peritectic steel at standard heat flux, owing to the greater shrinkage of this grade for the higher heat flux.

The inelastic strain results in Figure 2.17 show that the initial tensile inelastic strain peak decreases in magnitude with increasing carbon content. This increased tensile peak results in the lower-carbon steel grades (below 0.13 %C) remaining in tension at the surface, even after 30 s when the higher carbon grades have become compressive, this agrees with previous results [111]. This persistent tension is likely caused by the rapid shrinkage as a result of the narrow mushy zone in both the ULC and LC steels.

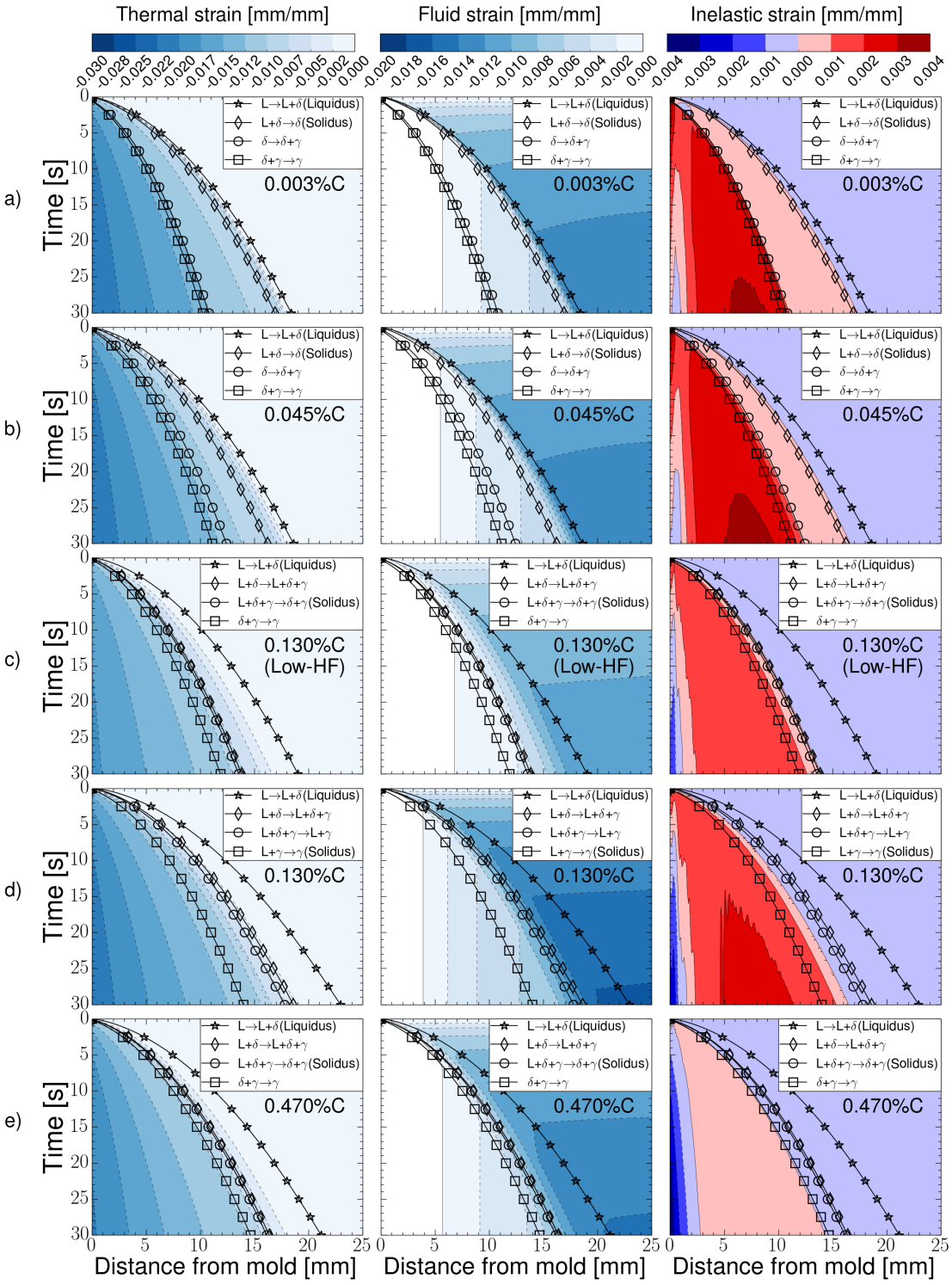

Figure 2.16: Thermal, Fluid, and Inelastic strain contours for five casting situations investigated: a) Ultra-Low carbon steel with Standard HF, b) Low carbon steel with Standard HF, c) Peritectic steel with Standard HF, d) Peritectic steel with Low HF, e) High carbon steel with Standard HF

Elastic The elastic strain is seen to peak at the austenite repacking transition of BCC to FCC. The transition manifests itself with an abrupt increase in Elastic strain at the 10%δ-90%austenite temp (corresponding an increase in strength of the region when it transforms from δ-BCC to austenite-FCC), followed directly by a drop to almost a strain-less condition ending with a slight increase back to positive strain at only a fraction of its previous (BCC) strain. It appears that high carbon steels have slightly lower elastic strain before this transition peak than the other grades, additionally it would seem that the Ultra-low carbon steel exhibits the highest relative elastic strain before and after this transition.

Inelastic Strain It can be observed that in all steel grades there is an initial period with development of negative inelastic strain. This effect becomes more apparent in the higher carbon content steels. This development occurs only within the δ-ferrite phase and quickly dissipates after 3 seconds. As we near the end of the simulation we observe that the inelastic strain at the surface has continued to decrease from its initial values, however, while the P, LC, and ULC appear to become negative the high carbon remains positive. It was observed however that qualitatively they are all moving in the negative direction.

2.10.4 Taper Practices

Strand solidification during continuous casting results in a shrinking cross-section down the caster. To accommodate this shrinkage and maintain support of the shell, a taper is applied to the mold on both the wide and narrow face coppers. Linear taper practices apply a fixed angle to the flat narrow face mold copper. While taper (and width) changes are sometimes conducted during casting, applied taper for a given heat is decided apriori based on the casting conditions and the grade being cast.

As mentioned before, differences in taper from the ideal shrinkage of the strand (under or over taper) can results in a variety of quality problems, for these reasons

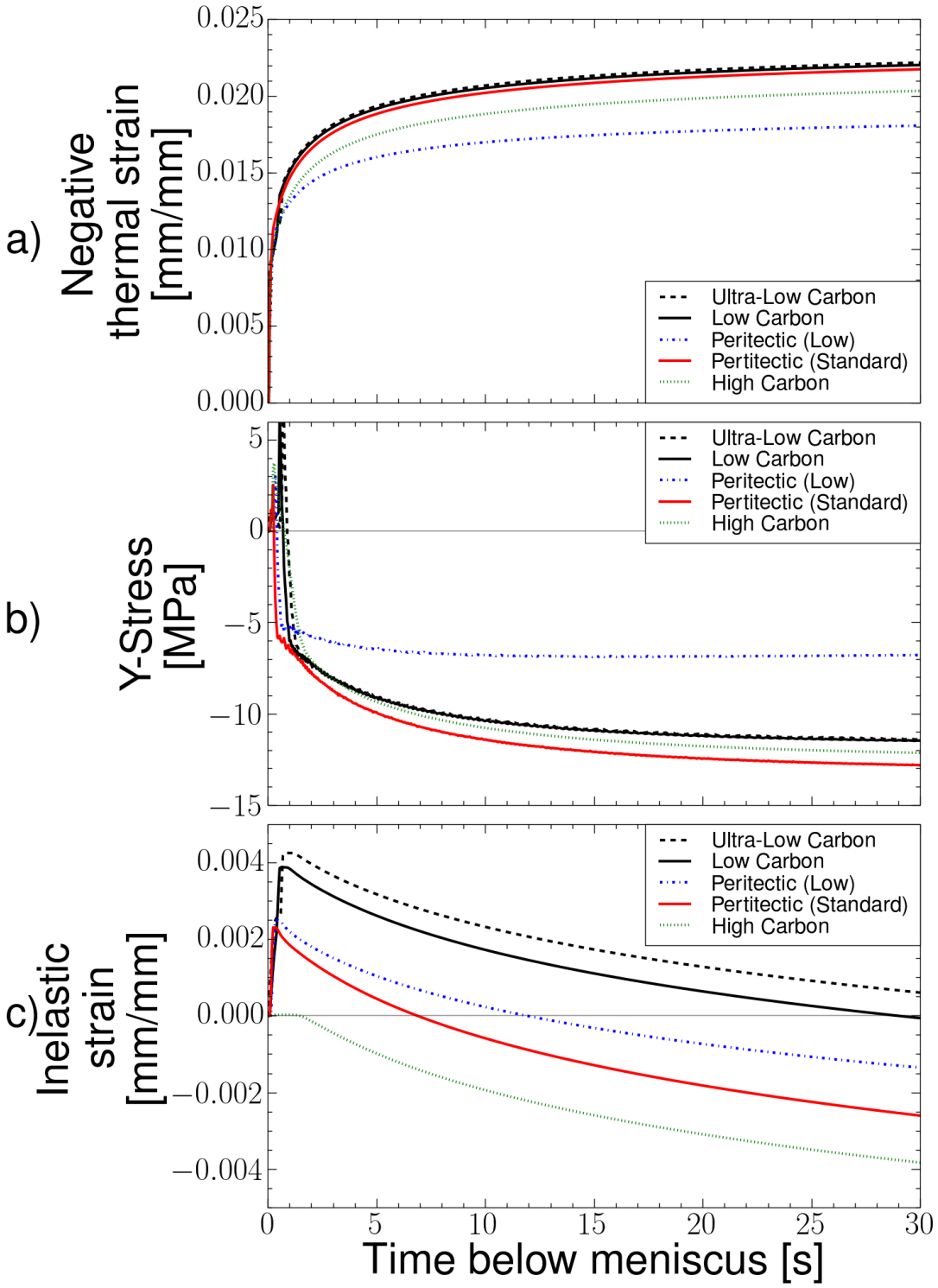

Figure 2.17: Surface profiles for five casting situations investigated: a) Inelastic Strain, b) Thermal Strain, C) Y-Stress

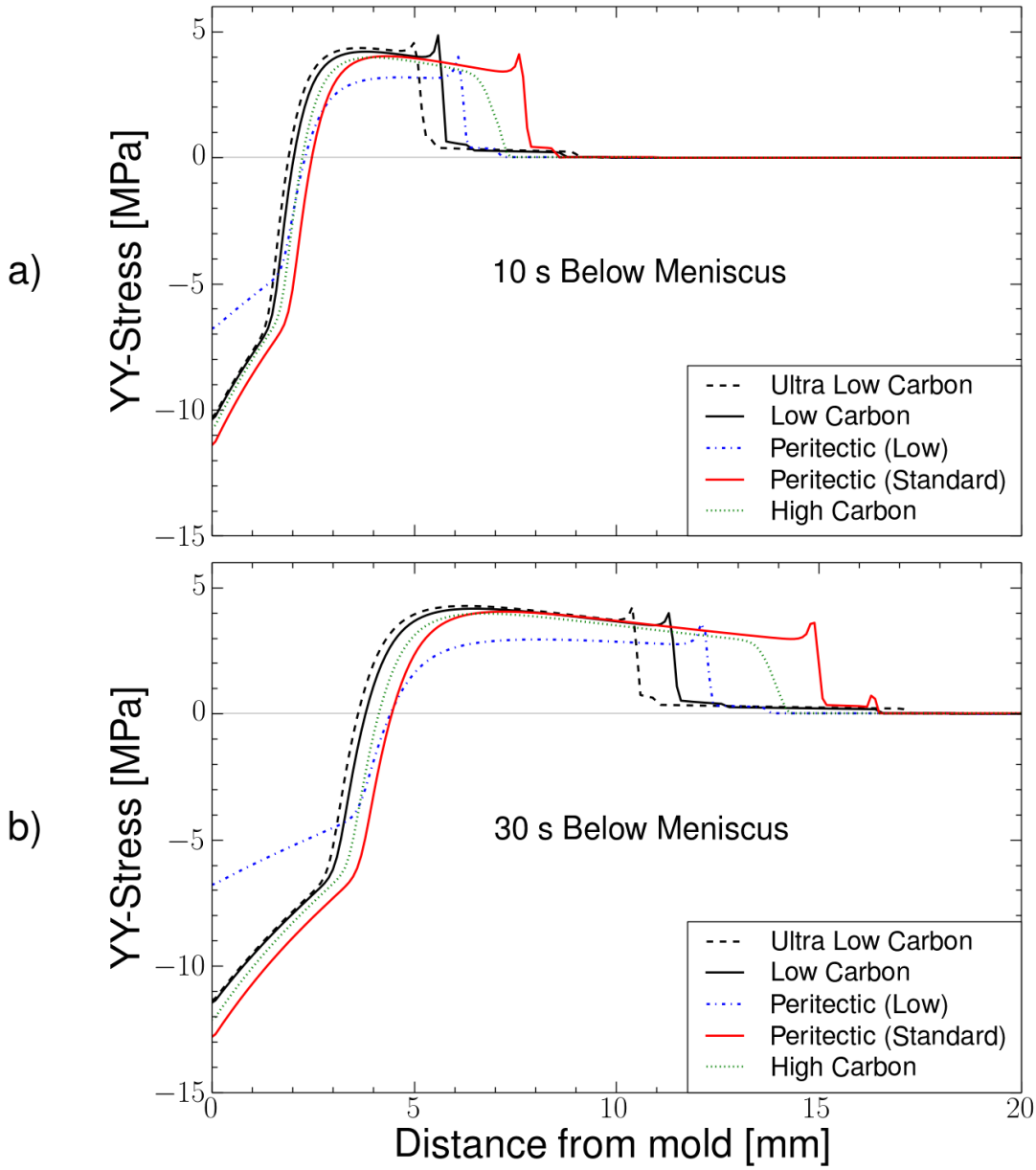

Figure 2.18: Y-stress profiles through shell thickness for five casting situations investigated: a) 10 s, b) 30 s

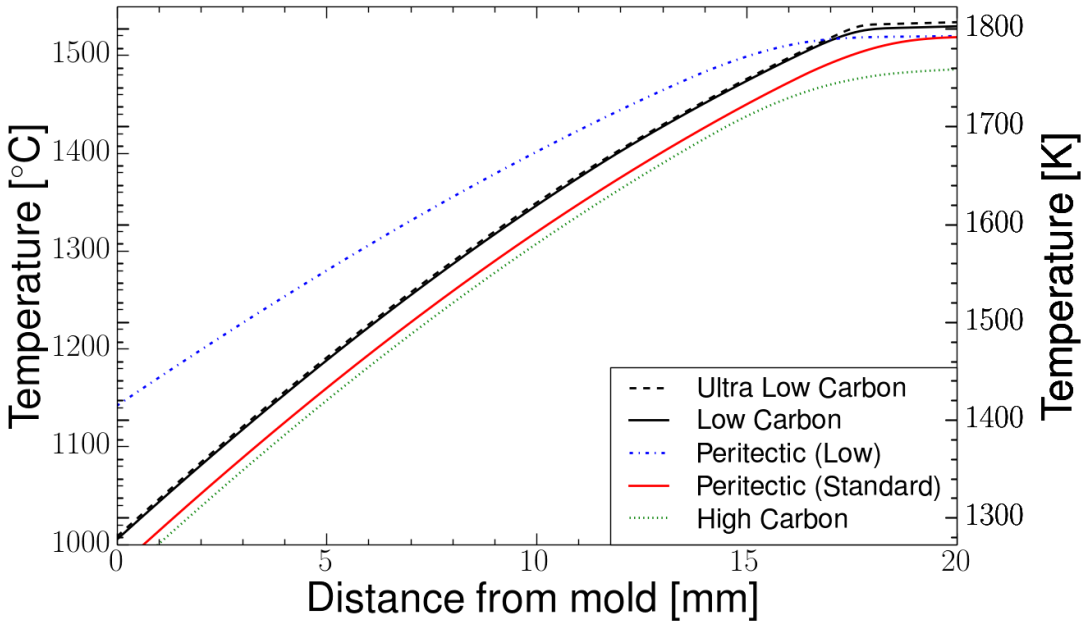

Figure 2.19: Temperature profile through the shell thickness at 30 s for five casting situations investigated

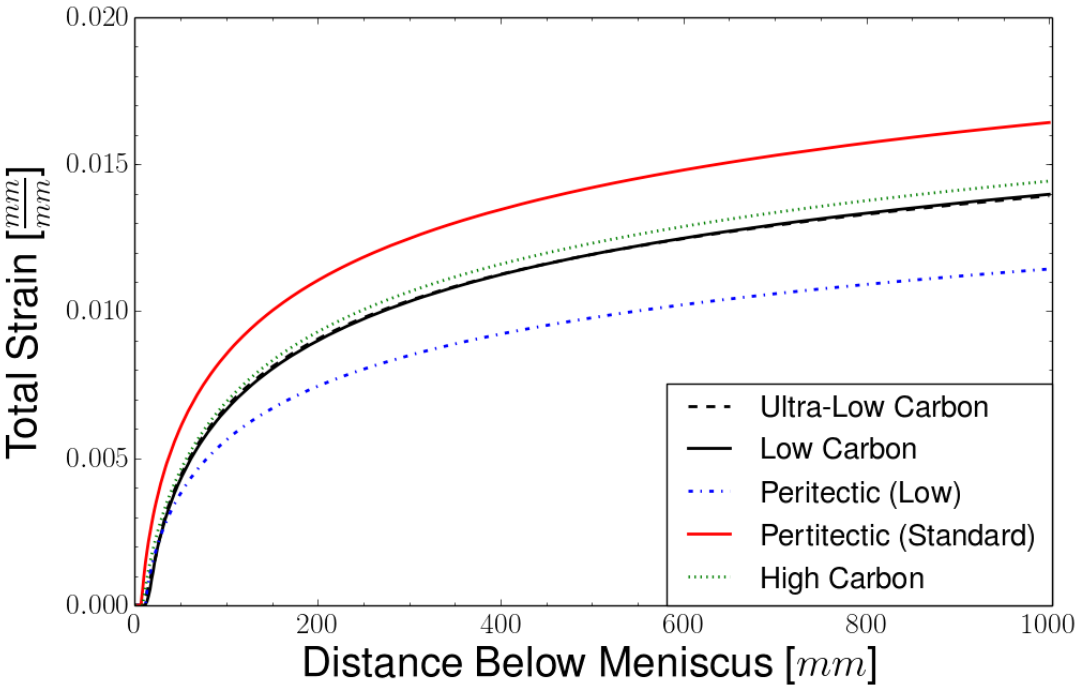

Figure 2.20: Ideal taper profile for five casting situations investigated

it is important the applied taper is closest to the ideal shrinkage for a given grade and casting condition. As shown in Figure 2.20 the ideal shrinkage profile for all of the steel grades is parabolic. The large initial shrinkage is a result of the sudden change in density as the crystal structure transitions from BCC to FCC. The majority of the shell shrinkage occurs during this transition period, after this this point the shell continues to shrink but the change is much smaller in magnitude.

While ferrostatic pressure aids in maintaining surface contact between the solidifying shell and the narrow face copper, applying a linear taper profile to an ideally parabolic shrinkage profile is likely to result in under taper, allow a gap to form, and potential bulging of the shell.

The peritectic grade simulated with both Low and Standard HF demonstrate that cooling rate has a strong effect on the final taper, increasing total strain by almost 50% with increased HF.

The ideal shrinkage profiles presented give a good starting point for general understanding of taper trends; however it does not provide all of the information required for proper taper selection.

In an operating caster mold distortion affects the operating shape of the copper. In a distorted mold, thermal expansion tends to cause the narrow face coppers to try and bow in towards the strand center-line. This results in a different realized taper than what is applied or indicated by sensors such as inclinometers. Depending on the water box support and bolt pattern, this can cause unpredictable results including premature mold wear and non-uniform changes in taper down the caster. Detailed discussion of mold distortion can be found elsewhere [112]

Taper based on TLE

Prior works have suggested that a basic taper practice should begin by looking at the expected TLE profile for a given grade. While this is a good starting point, it does generally result in an overestimation of the total shrinkage of the strand.

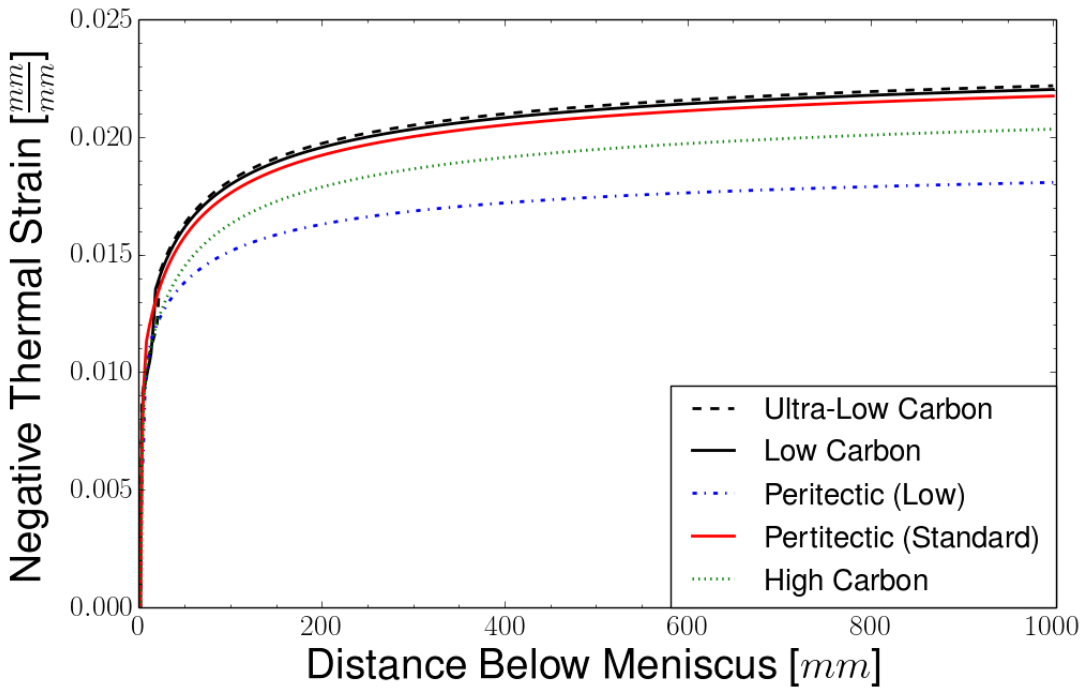

Figure 2.21: Thermal strain at the shell surface

Taper based on Total Strain Calculation

By taking into account all of the strain contributions we are able to get a much more accurate result with only a little extra work. As shown in Figure 2.21 the thermal strain does not exactly match with the Total strain Figure 2.20 and thus by using only the thermal strain for calculation we are not getting the whole picture.

As previous works have asserted, adopting a parabolic mold taper shape would be the most ideal, some even suggesting multitaper such as shown in Figure 2.22. However, machining a contoured profile into the mold is not inexpensive. A bi-linear taper, while far less common than a single linear taper, would also be a marked improvement in better matching the projected shrinkage of the shell. Clearly accounting for the fact that the majority of the shell shrinkage occurs in the upper 1/3 of the mold.

Grade Based Taper Practice

The results of this work have implications for optimal taper practice. Solidification and cooling result in shrinking of the steel shell; this shrinkage should be accommodated in order to maintain contact between the edges of the shell and the mold walls without an excessive air gap. This is accomplished in continuous casting by applying a taper to the mold walls that roughly matches this shrinkage represented by the total strain. Proper taper practice is important to mold operation to ensure safe, uniform heat transfer between the mold and shell, and to reduce the likelihood of surface defects and breakouts. Insufficient taper causes insufficient and non-uniform heat transfer between the strand and the mold across the gap, which can lead to corner rotation, shell thinning, and narrow face bulging [113]. Excessive taper can lead to many problems such as excessive mold wear, gutter, or even buckling of the shell. Both taper problems can cause gutter, longitudinal cracks, and breakouts.

As shown in Figure 2.20 the ideal taper profile for all of the steel grades is parabolic, according to total shrinkage, which is indicated by the total y-y strain decreasing with time down the mold. This shrinkage is controlled mainly by the drop in surface temperature, because the shell at the surface is coldest and strongest. The majority of the shell shrinkage occurs during this transition period while the shell is about 5 mm thick. After this this point the shell continues to shrink but the change is much smaller in magnitude as it is opposed by the increasing thickness and strength of the shell.

For the same heat flux, the peritectic steel experiences the greatest shrinkage and ideal taper, while the other three steels have similar, but lower profiles. This is because the large shrinkage that accompanies the δ-ferrite to austenite phase transformation occurs in the solid at high temperature in the peritectic steel, while the shell is still hot and weak, and unable to resist the shrinkage. However, with decreased heat flux, that is typical of the real commercial process, the peritectic steel experiences about 30% less shrinkage and ideal taper. The great dependence

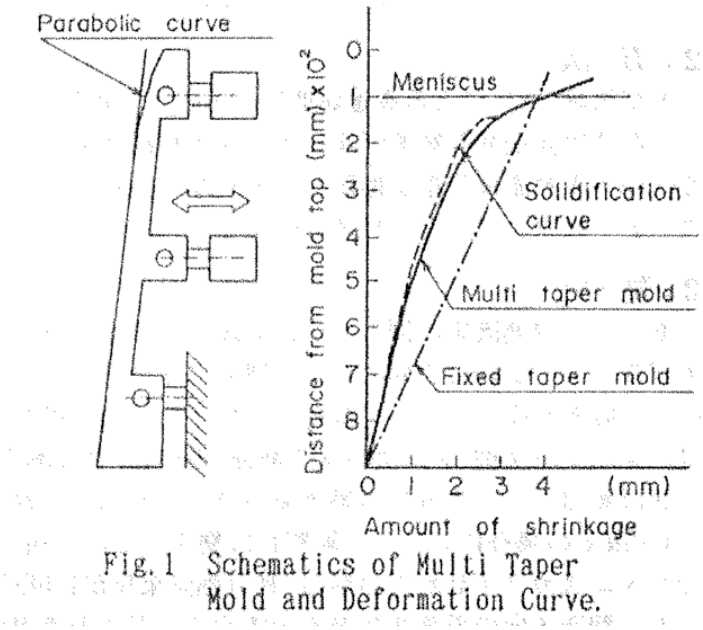

Fig. 1 Schematics of Multi Taper Mold and Deformation Curve.

Figure 2.22: Parabolic taper profile [115]

of taper on heat flux indicates that casting speed and mold powder should have a greater effect on ideal taper than steel grade, which is consistent with previous findings [41].

The total strain profiles presented here are only a rough starting point for designing ideal taper. Designing taper in a real operating caster requires consideration of many other factors, such as friction with the mold walls, creep expansion of the shell width due to ferrostatic pressure on the unmodeled mold faces, mold distortion [114], and mold wear. Further discussion can be found elsewhere [41].

2.11 Conclusions

A thermal-mechanical model of solidification of a flat steel shell has been developed and applied to investigate the effect of steel grade on temperature, stress, strain, ideal taper, and shell development during the early stages of solidification in a frictionless mold. The model features realistic boundary conditions based on previous literature, and realistic thermal and mechanical properties that vary with temperature, phase fraction, and carbon content. Four different steel grades were

investigated: Ultra-Low Carbon (0.003 %C), Low Carbon (0.04 %C), Peritectic (0.13 %C), and High Carbon (0.47 %C), simulating 30 s dwell times.

Mesh refinement for capturing solidification details was examined and element sizes of 0.1 mm or smaller may be required to properly study solidification phenomena. Proper treatment of the liquid in the stress model can alleviate convergence problems and avoid non-physical results.

- All steel grades were found to follow the same general solidification behavior of compression at the surface increasing with time, and tension towards the solidification front
- Initial solidification rate increases with carbon content
- Thermal strain dominates the mechanical behavior. Initially, fast cooling causes tensile stress and inelastic strain at the surface of the shell, with slight complementary compression beneath the surface, especially with lower carbon content
- As the cooling rate decreases, the surface then reverses into compression, with a tensile region developing subsurface . Stress decreases towards zero (the ferrostatic pressure) at the solidification front.
- More stress and inelastic strain are generated in the high carbon steels, because they are mainly composed of high-strength austenite
- Stress in the δ-ferrite phase is always very small, owing to the low strength of this phase

This simple model can help in the calculation of taper profiles for different steel grades and maintain the desired contact. While fixed linear taper practices are common in industry, it is clear that the desired profile of the shell is parabolic, which agrees with previous work [115].

2.12 Future Work

This work is the first step in development, validation, and application of a comprehensive transient 3-D model of thermal-mechanical behavior during continuous casting of steel slabs, including corner effects and non-uniform heat flux around the mold perimeter. In this modeling approach, the properties of different steel grades depend mainly on the phase fraction histories. This enables predictions of any steel grade knowing only the phase fraction histories, so extensive experimental testing is not required. Validation of this approach with measurements would be helpful, and is intended as future work.

Chapter 3

Thermal Resistor Model of the Shell-Mold Gap

3.1 Introduction

In continuous casting, as the liquid steel solidifies against the four walls of the water-cooled copper mold, the solidifying shell ideally does not come into direct contact with the mold copper. Mold powder is added to the free surface of the liquid steel, melts and flows between the steel shell and the mold wall to act as a lubricant. The re-solidified mold powder, or 'slag', adjacent to the mold wall cools and greatly increases in viscosity, thus acting like a solid. It is thicker near and just above the meniscus, where it is called the 'slag rim'. Depending on temperature, cooling rate, and cooling history, this slag layer may have a structure that is glassy, crystalline, or a combination as shown in Figure 3.1. As long as the interface temperature remains above its crystallization temperature, the slag layer will remain liquid and provide lubrication for the shell as it moves downward. If the interface temperature is at or below the crystallization temperature, liquid and solid layers may be present, and if the conditions allow, an air gap may form within the gap.

As the shell travels down the mold and solidifies it shrinks due to phase changes and thermal contraction. If the taper calculation is not adequate, an air gap may form in the space between the shell and the mold. The gap may also be affected by mold distortion warping the copper out of it's expected shape. The size of the gap is particularly important when exploring positions near the corner where geometry effects and shell strength outweigh ferrostatic pressure.

It has been estimated that the gap alone accounts for as much as 84% of the

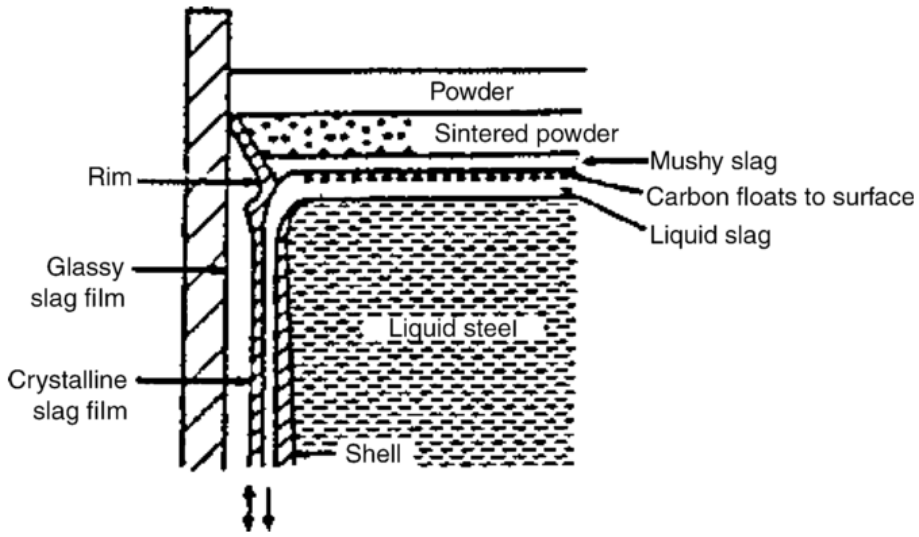

Figure 3.1: Schematic of slag layers in the mold [116]

total resistance, while the mold wall and the mold/cooling water interface accounts for the balance of 16% [17]. Thus, the behavior of heat removal in the mold is dependent largely on the behavior of the gap.

In an ideal casting, the mold gap is filled entirely with slag in either solid or liquid form. The slag provides lubrication between the moving shell and mold as well as aiding in heat transfer. If there is a disruption or non-uniformity in this lubricating layer, such as the formation of an air gap, the heat transfer will be strongly affected and potentially create local hot spots. Local hot spots and reheating are widely regarded to be one of the major causes for surface defects such as longitudinal cracks and depressions [11, 117].

3.2 Mold Gap Phenomena

3.2.1 Interfaces

It is clear from the literature that the interface resistances are significant relative to the total resistance of the gap [118,119]. The two most important interfaces are the interface between the copper mold and the flux layer, and the flux layer with

the shell. The Mold-Flux interface is the interaction between the copper mold surface and the solid layer of flux it is in contact with. The Flux-Shell interface is the interaction between the liquid or solid layer of flux. In the upper part of the mold this is almost always a liquid layer, however depending on conditions, this layer may have become fully solid by mold exit.

The Mold/Flux Interface

This interfacial resistance is largely a property of the particular mold powder as the surface roughness is related to its crystallization behavior as well as its transition temperatures [85]. The mold/slag interfacial resistance increases with crystallinity of the flux due to increased density of solid phase in the form of surface roughness on mold side (equivalent to air gap) also increases with thickness of the slag layer [119]. Prior works have treated this interface as temperature or thickness dependent, reducing the resistance with distance from the meniscus [120] or with increasing thickness [119]. However, for this work, a fixed value of $h_{Mold} = 2500$ $\mathrm{W\,m^{-2}\,K}$ was used for this Mold/Slag interfacial heat transfer coefficient which is in line with reported values [119]. The value of mold flux interface thermal resistance is given by Equation (3.2.1). Because the resistance value for this interface is fixed, calculation of the interface temperature, T_{mc}, is trivial according to Equation (3.2.2).

$$R_{Mold} = \frac{1}{h_{Mold}} \tag{3.2.1}$$

$$T_{mc} = T_{mold} + (T_{shell} - T_{mold})\frac{R_{contact}}{R_{total}} \tag{3.2.2}$$

The Flux/Shell Interface

Similar to the Mold/Slag interface, the slag strand interface resistance increases greatly as the temperature drops below the slag crystallization temperature. Non-

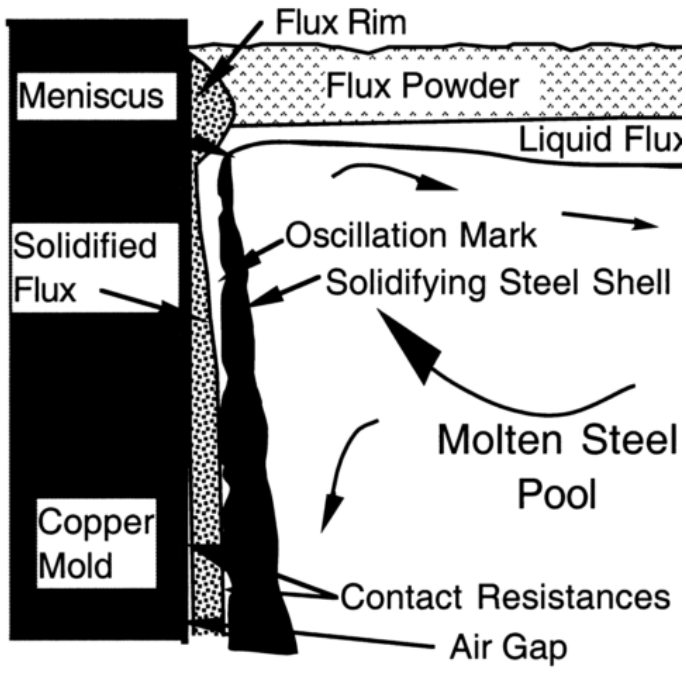

Figure 3.2: Contact interface roughness [118]

uniformities in the flatness of the shell surface shown in Figure 3.2 are incorporated into the model through this interface resistance. Data discussed in the literature [73, 90] seen in Figure 3.3, shows the variation in heat transfer with temperature. As this represents a large resistor relative to the total, and being highly temperature dependent on the interface temperature a fixed value was not used for this interface.

The interface resistance between the liquid slag and the solid steel shell is temperature dependent. The data points for the resistance were taken from the literature [90] and a curve fit was applied as shown in Figure 3.3. Hysteresis was not accounted for in calculation for this interface.

The flux/shell interface temperature, T_{ls}, is calculated using Equation (3.2.3). Deriving a smooth function for this temperature dependent behavior proved somewhat difficult but an exponential function, Equation (3.2.4), was chosen. The corresponding resistance value for the interface is calculated by Equation (3.2.5).

Flux-Strand Interface Temperature		
°C		W/m²·K
Temperature		$h_{Interface}$
Crystal	1030	1000
Softening	1150	2000
Solidus	1511	10000
Liquidus	1529	20000

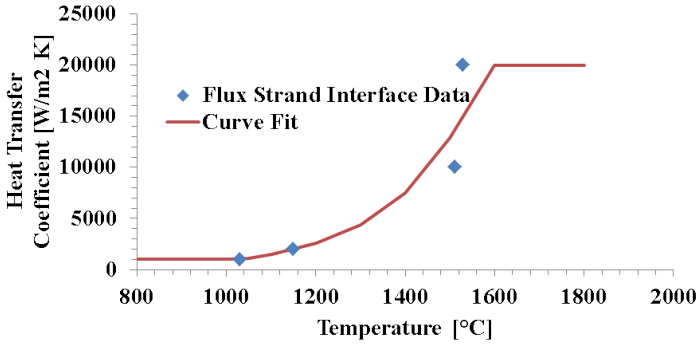

Figure 3.3: Temperature dependent slag/strand interface heat transfer/resistance [90]

Due to the non-physical implications of the exponential function on the upper and lower end, the interfacial coefficient was bounded. If $h_{Shell} < 1,000\ \mathrm{W\,m^{-2}\,K}$, $h_{Shell} = 1,000\mathrm{W\,m^{-2}\,K}$. This lower bound represents some theoretical oscillation mark/surface roughness opposition to heat transfer when the temperature is low enough. If $h_{Shell} > 20,000\ \mathrm{W\,m^{-2}\,K}$, $h_{Shell} = 20,000\mathrm{W\,m^{-2}\,K}$. This upper bound representing some degree of "perfect" contact and preventing numerical issues as it were to approach infinity.

$$T_{ls} = T_{mc} + (T_{shell} - T_{mold})\frac{R_{sol} + R_{liq} + R_{rad}}{R_{total}} \tag{3.2.3}$$

$$h_{shell} = 3.8981e^{0.0054T_{ls}} \tag{3.2.4}$$

$$R_{shell} = \frac{1}{h_{shell}} \tag{3.2.5}$$

3.2.2 Gap Formation in Continuous Casting

Shrinkage of the steel shell away from the mold walls may generate contact resistances or air gaps, which act as a further resistance to heat flow, especially after the slag is completely solid and unable to flow into the gaps. The surface rough-

ness depends on the tendency of the steel shell to 'ripple' during solidification at the meniscus to form an uneven surface with deep oscillation marks.

This depends on the oscillation practice, the slag-rim shape and properties, and the strength of the steel grade relative to the ferrostatic pressure, mold taper, and mold distortion. These interfacial resistances predominantly control the rate of heat flow in the process.

3.2.3 Slag Layer

As discussed above, mold powder is added to the free surface of the liquid steel. The mold powder on the top surface melts and forms a slag pool above the meniscus. As the steel is cast, liquid slag flows down around the sides providing the desired lubrication within the gap and solidifying as it moves below the meniscus. The powder can either be a mechanical mixture of fine grain oxides or a premelted and granulated mixture. Important properties such as: viscosity, basicity, melt temperature, melting rate and degree of crystallization are strongly related to the composition of the powder [4]. The composition of the casting powder may change throughout the casting due to reactions between steel and slag. As the composition changes, the essential properties of the slag will also change leading to variations in layer thickness, crystallinity, thermal conductivity, and resistance as shown in Figure 3.4 [119].

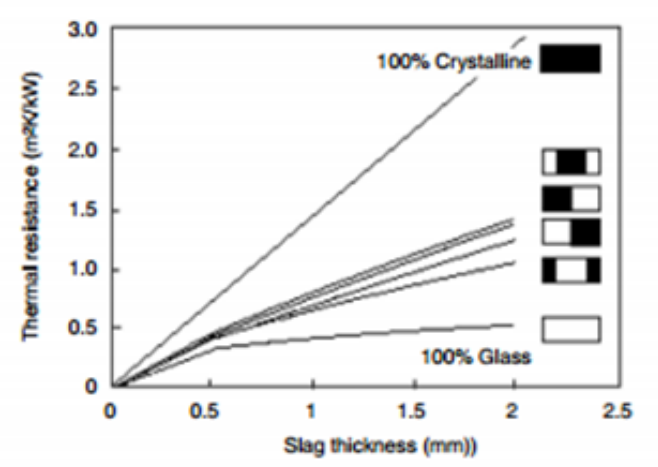

Figure 3.4: Crystallinity and thickness dependent conductivity [121]

The casting powder has several functions [4, 17, 121]:

- Protect the metal from oxidation
- Thermally isolate the upper surface to prevent meniscus solidification
- Absorb inclusions from the melt and dissolve them
- Lubricate the surface between mold and shell
- Allow for uniform heat removal
- Determine the meniscus shape by determining the metal/slag interfacial tension
- Further details on mold powders and slag behavior can be found in the literature [122].

There is dispute in the literature and practice on what exactly the distribution of the liquid and solid layers is. Plant practice has also shown that there is often liquid slag captured at mold exit, while still others report completely solid layers; while both scenarios do occur, the details remain rather unclear.

Solid Slag Layer

The molten slag flowing into the gap travels downwards with the strand during casting and gradually solidifies against the copper mold. A solidification temperature T_{Sol} is chosen for this model, a value of 650°C is used initially with variations explored in a parametric study. Reported values of critical flux temperatures vary widely across the literature and even between similar fluxes. They are still the

subject of much research, and the chosen value falls within a range of values found in the literature [90, 120, 123]. Flux powder contains air which gives the mixture a low conductivity, 0.3 $\mathrm{W\,m^{-1}\,K}$ [124]. As the powder heats, sinters, coalesces, and melts, the air disappears so its thermal conductivity gradually increases as shown in Figure 3.5 [123].

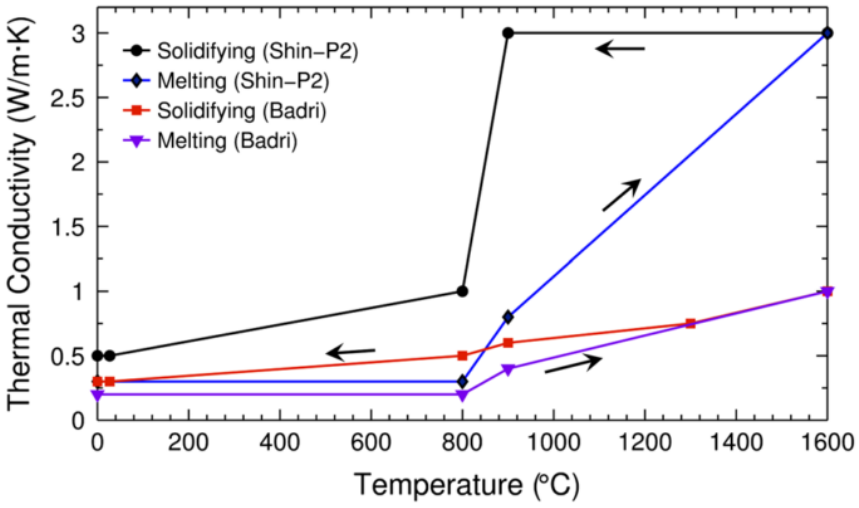

Figure 3.5: Temperature dependent conductivity [123]

The solid flux layer thickness D_{Sol} is calculated according to Equation (3.2.6) as a fraction of the total gap thickness with a linear relationship between the chosen flux solidification temperature T_{Sol} and the interface temperatures T_{LS} and T_{MC} given by Equation (3.2.3) and Equation (3.2.2) respectively.

$$D_{sol} = (T_{crystal} - T_{mc})\frac{D_{gap}}{T_{ls} - T_{mc}} \tag{3.2.6}$$

This model uses a fixed conductivity value of $k_{Sol} = 0.5\ \mathrm{W\,m^{-1}\,K}$ for the solid slag layer, this conductivity value is specifically lower than that of liquid slag and similar to values reported in the literature for solid slag which show decreasing conductivity with decreasing temperature [123]. Solid flux layer resistance R_{Sol} is calculated according to Equation (3.2.7) using the fixed value chosen for k_{Sol}.

$$R_{sol} = \frac{D_{sol}}{k_{sol}} \tag{3.2.7}$$

Liquid Slag Layer

The properties of liquid slag are complicated to say the least which makes conclusive data difficult to find. Reported values of liquid conductivity in the literature vary from 0.5 to 3 $\mathrm{W\,m^{-1}\,K}$ [18,20,21] in addition, slag conductivity exhibits the hysteresis effect. Within the slag, the liquid layer is assumed to be solidifying with distance from the meniscus as the shell temperature drops, thus for the purposes of this work the hysteris effect is ignored, a fixed value will be used, and it is assumed that once the liquid layer disappears, re-melting does not occur.

Within the liquid slag layer both conduction and radiation play a role. The radiation effect has been shown to contribute up to 30% of the total heat flux in the liquid layer but removal of this effect only reduced the total heat flux in the mold by 10% [120]. Some previous work has utilized a partially linearized form of the 4th order radiation equation [73] however, due to the difficulties associated with calculating the nonlinearity of the radiation equation as well as lack of time, an increased value for liquid slag conductivity was used to account for radiation instead.

The thickness of the liquid layer D_{Liq} is calculated based on the defined flax gap size D_{Gap} and the solid layer thickness D_{Sol}according to Equation (3.2.8).

$$D_{liq} = D_{gap} - D_{sol} \tag{3.2.8}$$

A constant thermal conductivity value for $k_{Liq} = 3\ \mathrm{W\,m^{-1}\,K}$ is used based on work appearing in the literature [123]. Thermal resistance of the liquid layer R_{Liq} is calculated using this fixed value according to Equation (3.2.9).

$$R_{liq} = \frac{D_{liq}}{k_{liq}} \tag{3.2.9}$$

This work assumes that a decrease in conductivity is balanced by the increase in radiation at higher temperatures [123], which agrees with the other models [125] and the measurement of constant conductivity in molten slag systems [124]. A

minimum threshold value for liquid layer thickness is chosen to ease numerical difficulties and prevent wildly large values for heat transfer coefficient. This thickness $D_{LiquidThresh}$ is chosen to be 0.01mm for this work which represents a maximum h value to be $20,000\ \mathrm{W\,m^{-2}\,K}$, values used in the literature have been in this range [73].

3.2.4 The Air Gap

As discussed previously, if conditions within the mold allow for it, an air gap can form. The size of the air gap is an output of the stress model in the form of displacement of the shell surface nodes from the mold. This model includes time dependent ferrostatic pressure applied as a traction pulling the shell towards the mold surface. To help the numerical solution a minimum threshold value $D_{AirThresh} = 0.001$ mm is adopted to prevent non-physical behavior associated with very small gaps (displacements). The details of the ferrostatic pressure method are the same as that described in Appendix A.1.

Additionally, if there is a liquid layer of slag present in the gap above the chosen T_{Sol} temperature, the air gap is given to be filled with liquid slag. This condition is based on the assumption that liquid slag from above the gap location would flow downwards to fill in this gap.

The thermal conductivity of the air gap is dependent on composition of the gas [126]. Prior work has values assumed for air [90] as well as a 20% hydrogen mixture [126] using the binary conductivity mixture rules [127]. For this work a fixed value for conductivity $k_{Air} = 0.06\ \mathrm{W\,m^{-1}\,K}$ is used for the air gap [85]. This value is consistent with low temperature values for a high hydrogen environment found in the literature [126]. A temperature dependent conductivity value is left for future work. The thermal resistance of the air gap is given by Equation (3.2.10).

$$R_{Air} = \frac{D_{Air}}{0.06} \tag{3.2.10}$$

3.2.5 Total Gap Heat Transfer

The heat transfer model is dependent on the 5 resistant components in the gap described above: the mold/slag interface, the air gap, the solid slag layer, the liquid slag layer, and the slag/steel interface. Combining Equations (3.2.1), (3.2.5), (3.2.7), (3.2.9) and (3.2.10) into Equation (3.2.11) yields Equation (3.2.12) and an effective thermal resistor model represented by Figures 3.6 and 3.7.

Heat conduction depends on the thermal resistances and time-averaged thickness profiles down the mold of the different layers of materials contained in the gap. For the purposes of this model, we are concerned primarily with the bulk behavior of the solidifying shell. as such a number of simplifications will be made: In addition to those discussed above, some simplifying assumptions were made for this model:

- The potential buildup of scale, and/or resulting blockage, within the water channels was neglected, thus we will assume that the mold is operating at steady state with constant temperature $T_{Mold} = 150°C$
- The distribution of liquid and solid slag will be assumed linear between the interface temperatures
- As mold slags are mixtures they do not have a singular transition temperature. While there is some debate on the minimum percentage of liquid slag that would fill in an air gap, for the purposes of this work, 60% liquid slag will be assumed to fill in an air gap.
- The latent heat evolved by liquid-slag solidification is less than 3% of the heat transferred across the gap, so it is neglected in this model. [96]
- Oscillation marks and prescribed surface shape non-uniformity are neglected
- Interface resistances are not dependent on flux layer thickness

Table 3.1: Gap conductivity and resistance values

Location	Conductivity/Conductance	Resistance
	$\mathrm{W\,m^{-1}\,K^{-1}}/\mathrm{W\,m^{-2}\,K^{-1}}$	$\mathrm{m^2\,K\,W^{-1}}$
Mold/Flux Interface	33 (h_{mold})	0.0004
Air Gap	0.06 (k_{Air})	$D_{Air}/0.06$
Solid Flux Layer	0.5 (k_{Sol})	$D_{Sol}/0.5$
Liquid Flux Layer	3.0 (k_{Liq})	$D_{Liq}/3.0$
Flux/Shell Interface	$3.98e^{0.0054T_{ls}}$ (h_{shell})	$\frac{1}{3.98e^{0.0054T_{ls}}}$

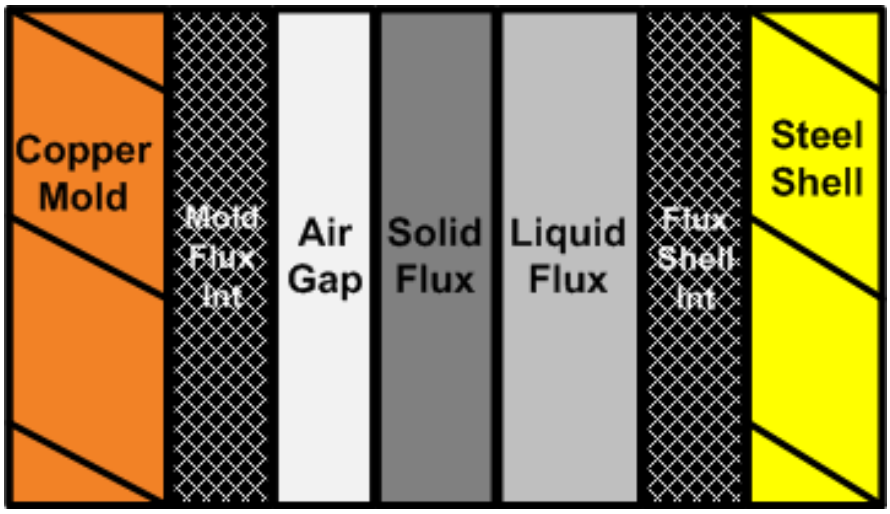

Figure 3.6: Interfacial gap material schematic

$$R_{total} = R_{Mold} + R_{Air} + R_{Sol} + R_{Liq} + R_{Shell} \tag{3.2.11}$$

$$R_{total} = \frac{1}{h_{Mold}} + \frac{D_{Liq}}{k_{Liq}} + \frac{D_{sol}}{k_{Sol}} + \frac{D_{Air}}{k_{Air}} + \frac{1}{h_{Shell}} \tag{3.2.12}$$

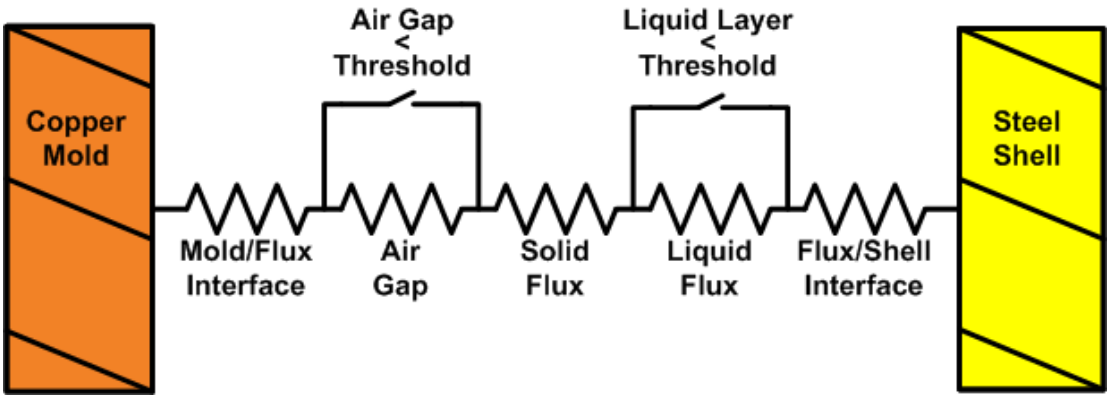

Figure 3.7: Interfacial gap resistor schematic

3.3 The Model

The model was first implemented in Microsoft Excel for troubleshooting and proof of concept and implemented into a FORTRAN subroutine GAPCON for ABAQUS finite element software. The flowchart for operation can be found in Figure 3.8. The primary inputs of interest to the subroutine from ABAQUS are the temperatures of the slave and master surfaces. For inclusion of the coupled model results and potential air gap formation, the distance of the surfaces from each other is also needed. The surface displacement is first converted to meters from the millimeter units of the model. If this value is larger than the threshold size for air gap formation, the resistance is calculated according to Equation (3.2.4), if it is less than the threshold, the resistance is set to 0.

The fixed value for the mold/flux interface resistance is calculated according to Equation (3.2.1).

On the first call to the program, initial values for the interfacial temperatures are set to approximate values. In addition, we programmatically assume that the gap is half liquid and half solid so that a starting total resistance can be approximated. As iterations will be performed, these values need only to be reasonable for the initial conditions.

The model then checks if the solidification flag has been thrown indicating that

in a previous increment, the entire slag layer solidified. If the entire slag layer has become solid, it is assumed that it will remain solid, a simplified calculation is performed, and iterations are skipped.

If the solidification flag has not been thrown, the program enters the iteration loop. The loop begins with calculation of the shell interface resistance according to the previously calculated interface temperature. As discussed, this value is bounded, and if it is found to be outside of the bounds, it is set equal to the appropriate value.

Based on the newly calculated interface resistance, a new total resistance is calculated and used to calculate new interface temperatures. The flux layer calculation is then performed using these new interface temperatures to find the size of the solid slag layer. If the liquid slag layer is found to be smaller than the threshold size set by the user, the entire gap is assumed to be solid, otherwise the remaining gap space is assumed to be liquid. The loop counter is incremented by one, and the loop repeats. When all iterations have been performed, the loop exits. If the temperature of the shell is below 1400°C (chosen to reduce the likelihood of an accidental flag trip too early in the simulation) AND the entire slag layer is solid, the solidification flag is tripped.

Finally, the gap resistance is totaled, converted to heat transfer coefficient, and output to ABAQUS.

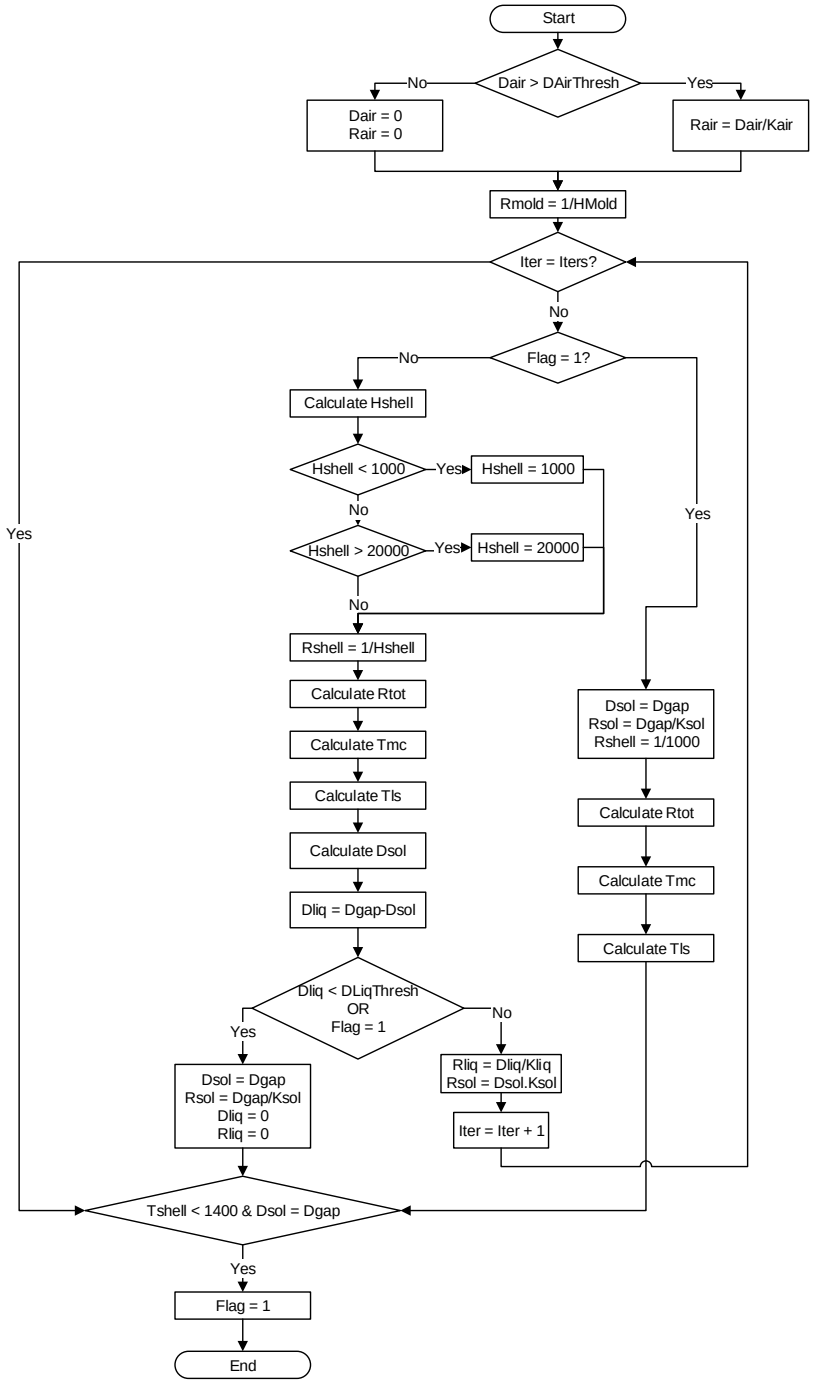

Figure 3.8: Calculation flowchart for resistor model

3.4 Heat Transfer Model Results

Working up to the full model, some simplified versions were created to verify expected behavior. Uniform flux thickness results in uniform heat transfer across the surface, it is non-uniformity in flux thickness that creates heat transfer variations and local hot/cold spots. These local hot spots are known to result in displacement from the surface as the steel shell begins to reheat. Before induced air gaps can be examined, uniform thicknesses were studied. For models with no air gap or a defined air gap the shell surface was constrained to remain fixed in the x direction within the stress model and ferrostatic pressure was not applied.

3.4.1 Base Case Results

Using a uniform total flux layer thickness of 2mm with no air gap, a first model was simulated using the values found in Table 3.1. Results of this comparison are shown in Figure 3.9, differences between Excel and ABAQUS results at early times are purely numerical and are ignored. In general both the calculated resistance and resultant heat flux have infinity norm error on the order of less than 2%. Results indicate values of approximately 4.5 $\mathrm{MW\,m^{-2}}$ at the meniscus gradually decreasing to 1.3 $\mathrm{MW\,m^{-2}}$ at 30 s. This decreasing behavior is to be expected, and the values do not appear unreasonable based on prior work of the author, and values that appear in the literature as shown in Figure 2.3.

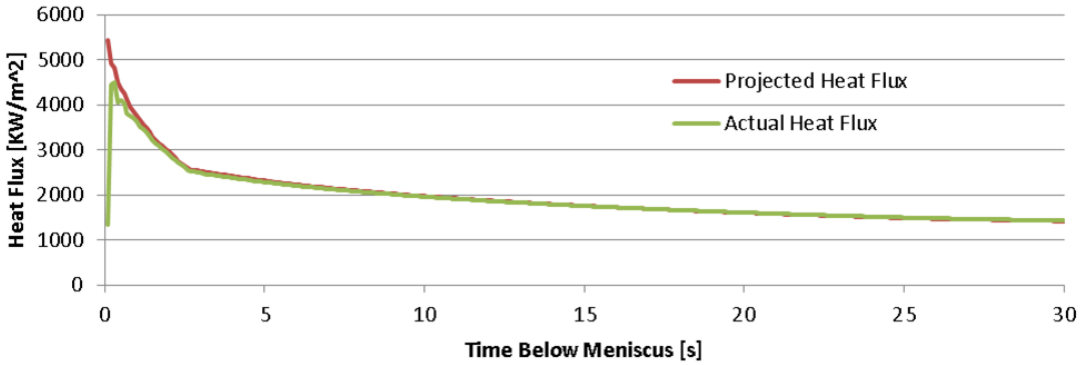

Figure 3.9: Projected and actual heat flux

3.4.2 Effect of Flux Layer Thickness

Studies were carried out using a constant total flux layer thickness shown in Figure 3.10. It was observed that with all other properties fixed, as flux layer thickness increased, heat flux across the interface dropped. The change from 0.5mm to 2mm resulted in a continuous difference of about 1000 $\mathrm{W\,m^{-1}\,K}$ with = 800°C.

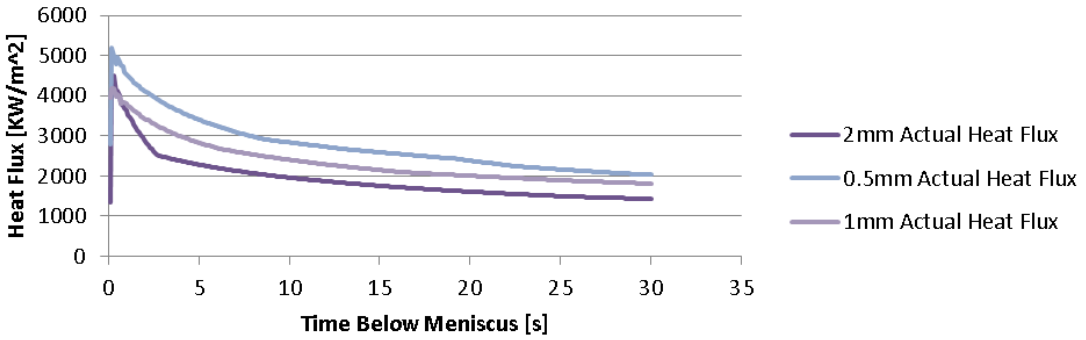

Figure 3.10: Flux layer thickness variation with 800°C solidification temperature

3.4.3 Effect of Flux Solidification Temperature

Studies were conducted using a fixed flux layer thickness while varying the solidification temperature of the slag layer. was fixed at 2mm, and the solidification temperature was varied according to values found in the literature 650°C, 800°C, 1030°C. Results, shown in Figure 3.11, indicate that as solidification temperature decreases, the interface heat flux rises. This is consistent with expectations as the higher conductivity liquid layer persists in the gap longer which lowers the total resistance within the gap.

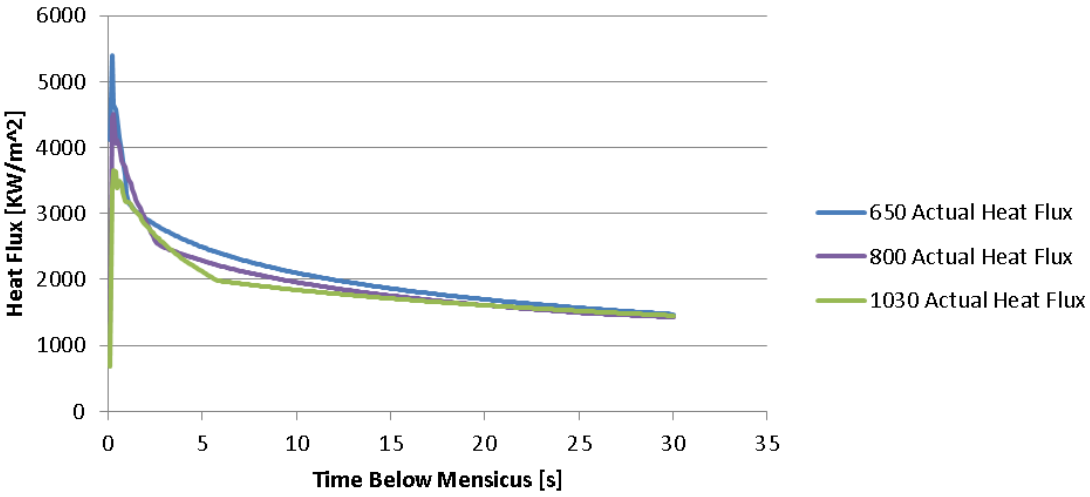

Figure 3.11: Effect of solidification temperature variation

3.4.4 Effect of Flux Layer Thickness Variation

Studies were conducted with the flux thickness varying with time/distance below the meniscus. Results are shown in Figure 3.12. The 2mm thickness with = 800°C was compared to a variation of 2mm at the meniscus decreasing linearly to 1 mm at mold exit. The varying flux thickness is shown to have a corresponding increase in heat flux as the mold flux thickness decreases. The difference in heat flux is more pronounced after 5 s

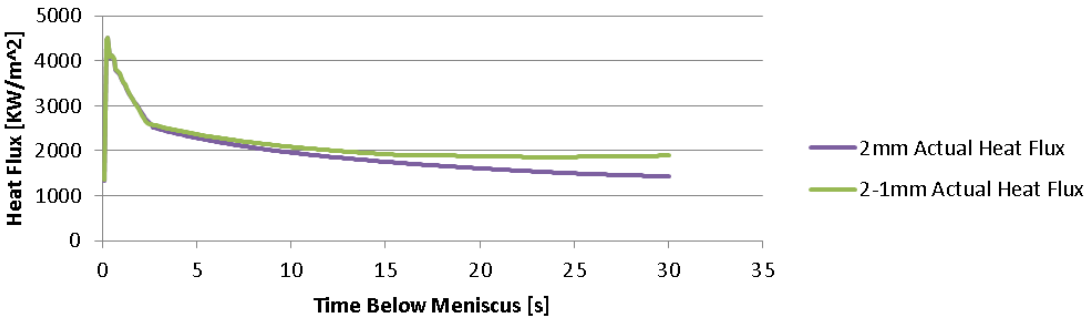

Figure 3.12: Time varying flux thickness with 800°C solidification temperature

3.5 Coupled Thermal-Mechanical Model of Slag Finger Depression

As discussed earlier, non-uniform flux thicknesses can result in heat transfer variation. This variation can often lead to local hot/cold spots, and depending on the severity these can lead to depression formation and shell reheating. The eventual goal of this work, as addressed in future work, is to utilize the GAPCON subroutine with a fully coupled 2-Dimensional model to explore the formation behavior of surface defects in continuous casting. One possible cause of a depression is a slag finger, where slag infiltrates down below the meniscus in a non-uniform manner creating a local bulge in the flux layer thickness. With this in mind, the last simulation presented in this work implemented a flux layer distribution similar to that of a slag finger - with thickness uniform in the casting direction but varied across the surface around the perimeter. For simplicity, the liquid steel domain and mesh does not account for the change in physical shape of the shell surface profile as a result of the bulging layer, this effect is only accounted for in the thermal model by way of the locally thicker flux.

3.5.1 Model setup

Model Domain & Implementation

The general model domain is shown in Figure 3.13, and occupies a small portion along the wide face of a continuous caster away from the corner region. The ABAQUS mesh implementation is shown in Figure 3.14.

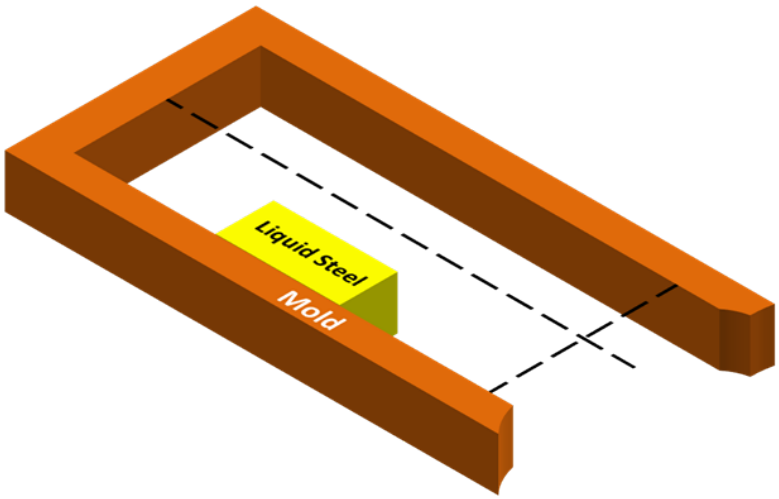

Figure 3.13: Slag finger domain

The model uses CPEG4HT elements in ABAQUS: Two dimensional, piecewise linear, continuum, generalized plane strain, 4 node, diffusive heat transfer, hybrid elements. The steel domain was divided into 0.5 mm square elements for a total of 3200 elements.

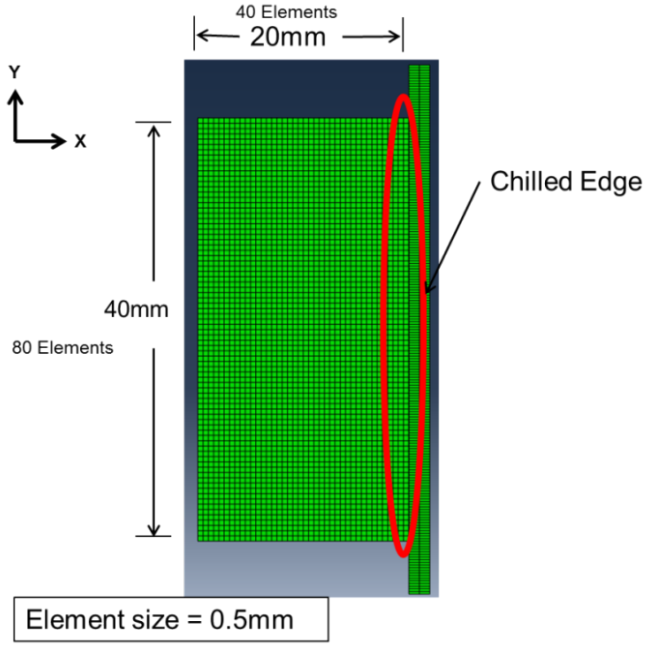

Figure 3.14: Slag finger mesh

Boundary conditions

The thermal and mechanical boundary conditions for the model domain are shown in Figures 3.15 and 3.17. The GAPCON subroutine is applied on the contact surface between the steel shell and the mold with the other 3 sides insulated.

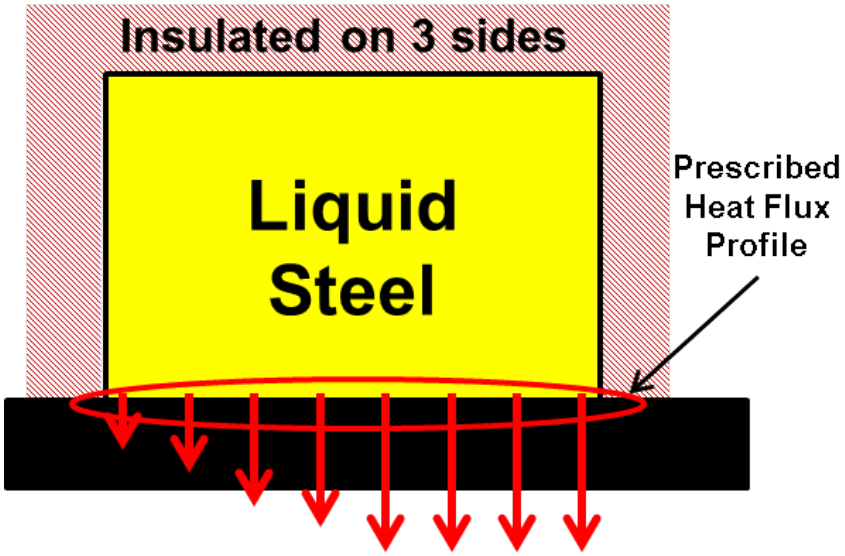

Figure 3.15: Slag finger thermal boundary conditions

Shown in Figure 3.16, the flux layer thickness is a uniform 1 mm across half of the domain, at the depression centerline the flux adopts a 2 mm thickness in a 12.7 mm wide region. Between the two areas, the thickness varies linearly. The 12.7 mm width was chosen as the half width of a potential 25 mm slag finger.

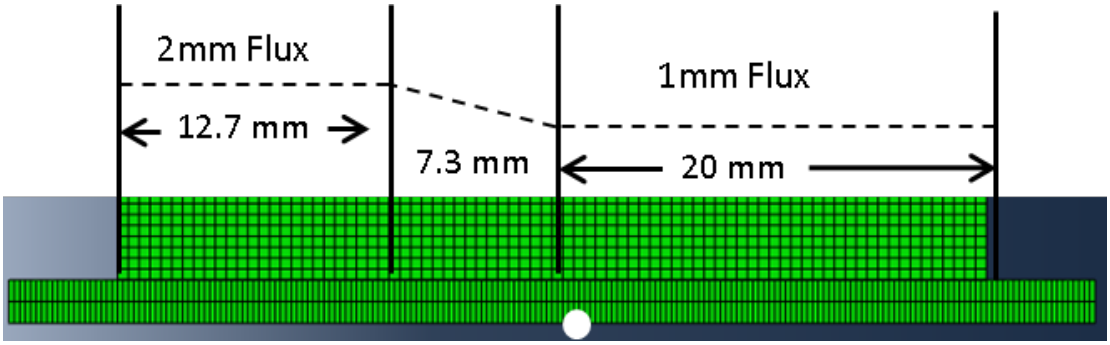

Figure 3.16: Slag finger model implementation

For constraints on the stress model, the mold is held fixed in all directions. The

treatment for ferrostatic pressure pulls the steel shell towards the mold wall, and the shell is allowed to slide along the mold wall. This also prevents rigid body motion. For this work a friction coefficient of $\mu = 0.15$ was given to ABAQUS based on reported values for solid slag on copper and acts only on the contact interface. The left and right edges represent symmetry planes. The right side is fixed in the y-direction and only allowed to displace towards or away from the mold, the left side is required to move as a straight line, and the top surface remains stress free.

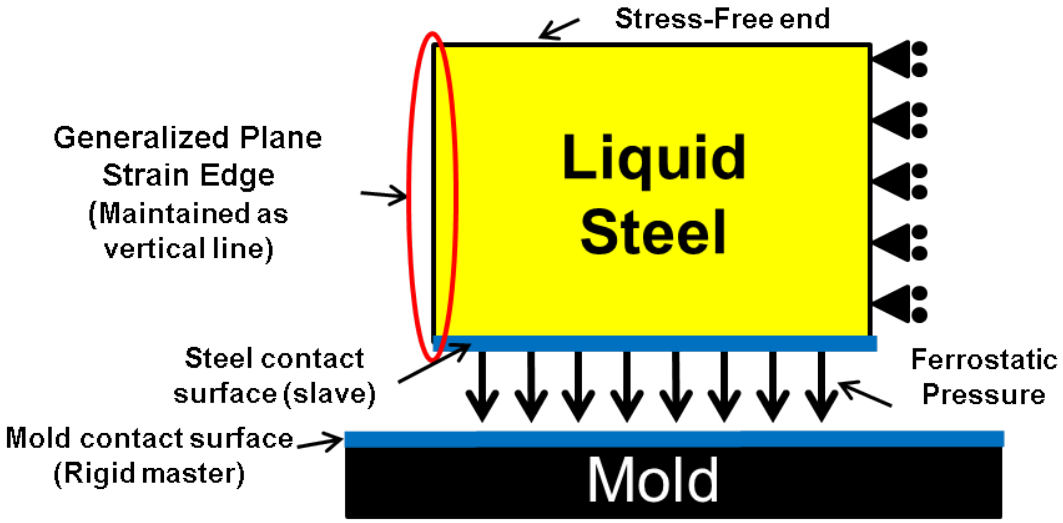

Figure 3.17: Slag finger mechanical boundary conditions

Ferrostatic pressure is applied on the domain as shown in Figure 3.17, increasing with time and starting at a value of 0.00129 MPa at 0.35 s when the first row of elements is solid. The value increases linearly proportional to time according to: $P_{Ferro} = \rho g V_c t$, where ρ is the density, g is the gravitational constant, V_c is the casting speed, and t is the time below meniscus. No additional displacements or tractions are applied to the domain, these conditions are selected to simulate an ideal casting situation where the mold taper exactly follows the desired shrinkage of the strand.

Material Properties

The same low carbon steel grade used in the Chapter 2 was used for this work with a pour temperature of $1533°C$. Full details on the material properties for this steel grade can be found in Section 2.7.

3.5.2 Results

Displacement and heat flux histories are shown in Figure 3.18. The depression does not appear until approximately 4.7 s into the simulation; prior to this point the surface separation was less than the specified threshold for an air gap to form. After this time the air gap resistor becomes active in the model and as shown in the figure, the center heat flux profile slope decreases along with the growing depression depth, to a maximum depth of about 0.3 mm. Heat flux variation from depression center to the far field starts close to 2 MW m^{-2} and is on the order of 1 MW m^{-2} at the end of the simulation.

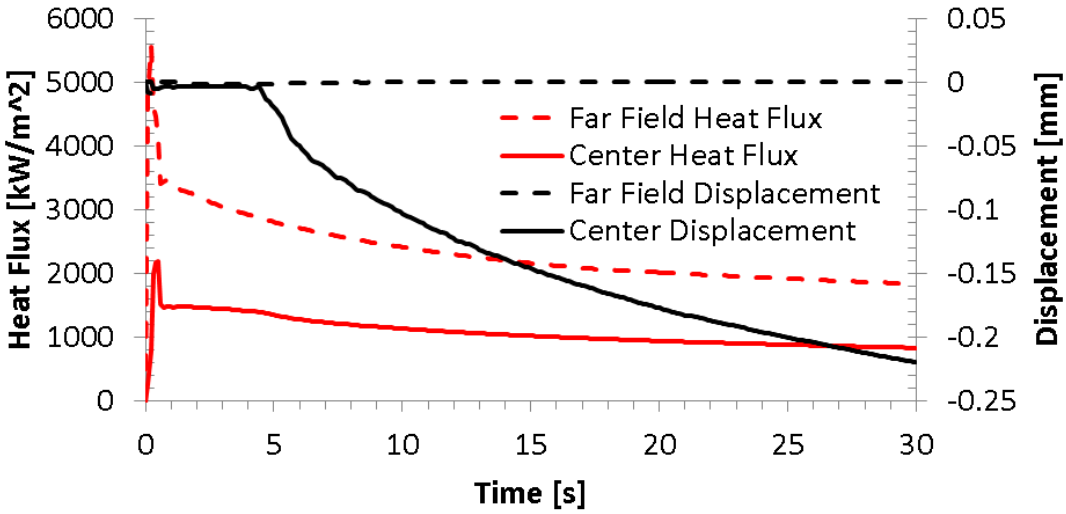

Figure 3.18: Slag finger model results

The shell surface separates from the mold wall along almost the entire length of the domain; Figure 3.19 shows the deformed shape scaled 5X with a contour values for displacement normal to the mold surface. A U shaped depression is seen

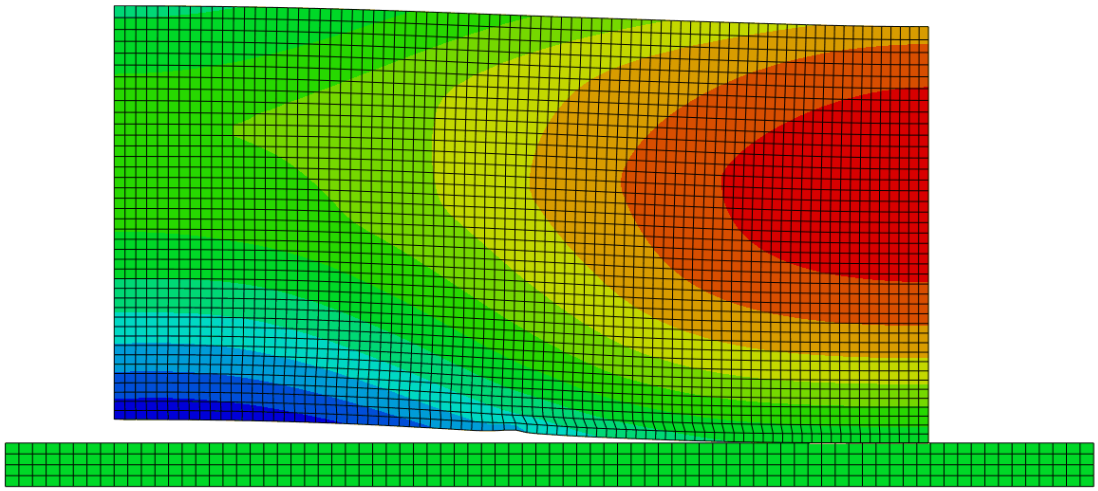

Figure 3.19: Slag finger model deformed shape (Displacements magnified 5X)

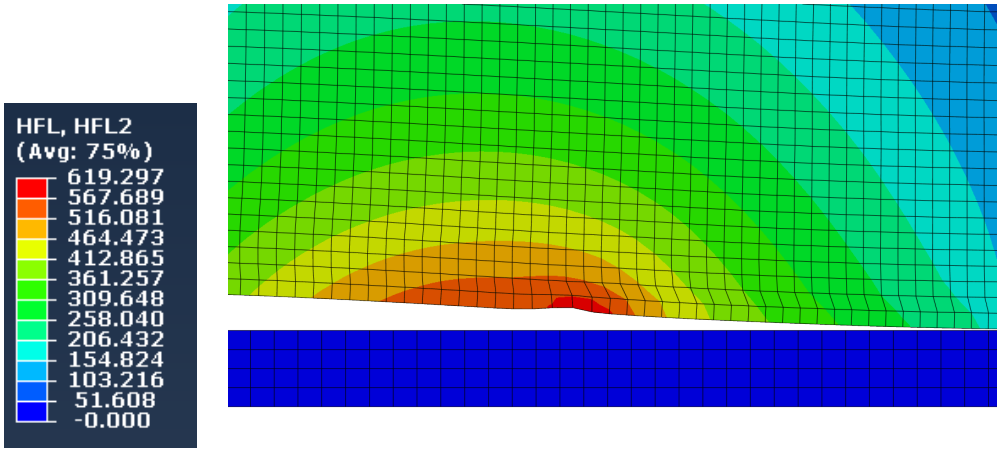

Figure 3.20: Y-heat flux contour plot showing distorted elements (Displacements magnified 5X)

to form in the 2 mm flux region; this is in line with expected behavior for these conditions. What does stick out however is what looks like distorted elements at the middle on the surface of the domain; Figure 3.20 shows a closeup of this region with contours of the heat flux tangent to the mold surface. The distortion itself is small relative to the total depression depth, and with the interest focused on large scale behavior, exploration of this issue is left to future work. Note: In the deformed shape figures the shell elements are 0.5 mm square.

When there is a reduction in local heat flux, in this case as a result of the

thicker mold flux layer, the shell remains hotter in this location. Temperature results for the slag finger are shown in Figure 3.21. At the depression center, the shell reaches 1329 °C, which is 350 °C hotter than the rest of the shell surface which is around 970 °C. As the rest of the shell continues to grow at the original rate of solidification, the locally depressed region experiences slower solidification; and as the rest of the shell cools and shrinks, stress concentrates in this thinned region and necking occurs creating a U-shaped depression. In extreme cases, this slowed solidification can progress to the point of remelting - because once contact with the mold is lost, the primary heat removal path is eliminated, the solid is unable to dissipate the energy, and the liquid steel interior will begin to reheat the shell. This can be seen in Figure 3.22 which shows the liquid fraction in the domain at 10 s, when the shell thins to 6 mm thick at the depression center relative to about 9 mm elsewhere.

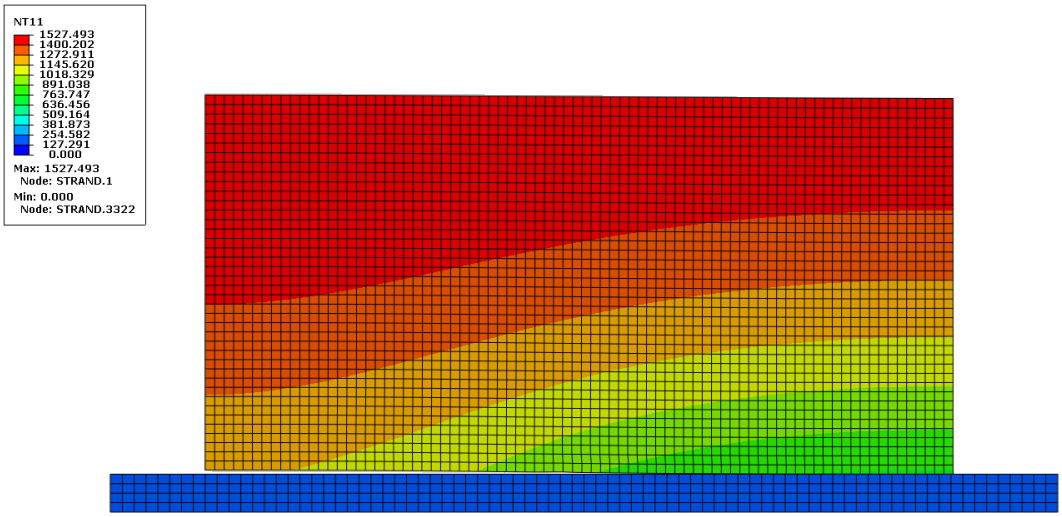

Figure 3.21: Slag finger temperature results at 30 s (Unmagnified)

The blue region represents solid phases and the red represents liquid, the colors in between are the mushy zone, which shows the shape of the solidifying shell. The left side of the domain where the thicker flux layer is present displays a 30% thinner solid region than the right side of the domain. This is a direct result of the reduced heat transfer experienced by the thicker flux region.

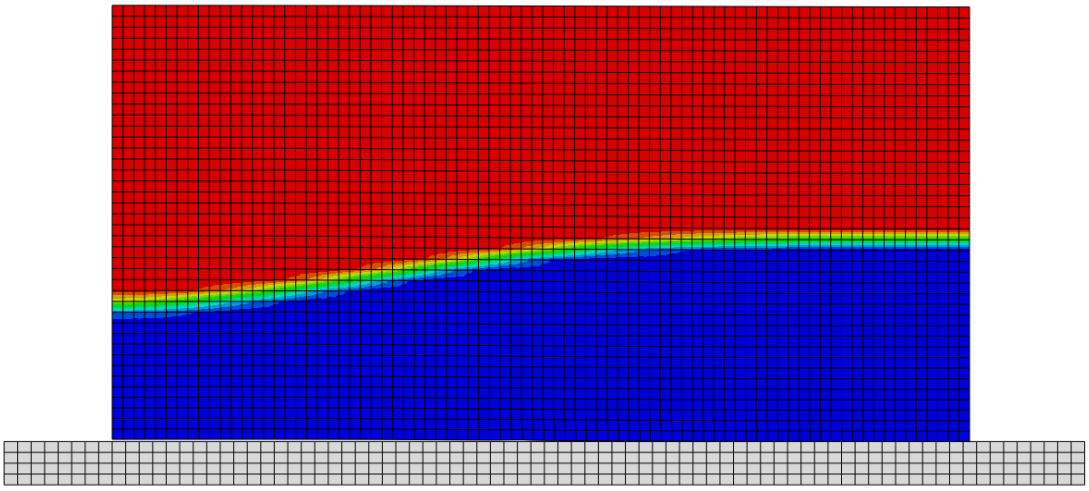

Figure 3.22: Slag finger liquid fraction contour at 10 s (Unmagnified)

The expected behavior of compression at the surface progressing to tension towards the solidification front is visible in Figure 3.23. The uniform heat flux region on the right side of the domain has compression on the surface of about 16 MPa. As the flux layer thickness decreases towards the depression centerline, the compressive stress decreases to about 1/4 of this value. In more extreme cases, with either larger reduced region, thinner flux layer, or with an applied tension (such as in an undertapered mold) this surface stress could become tensile.

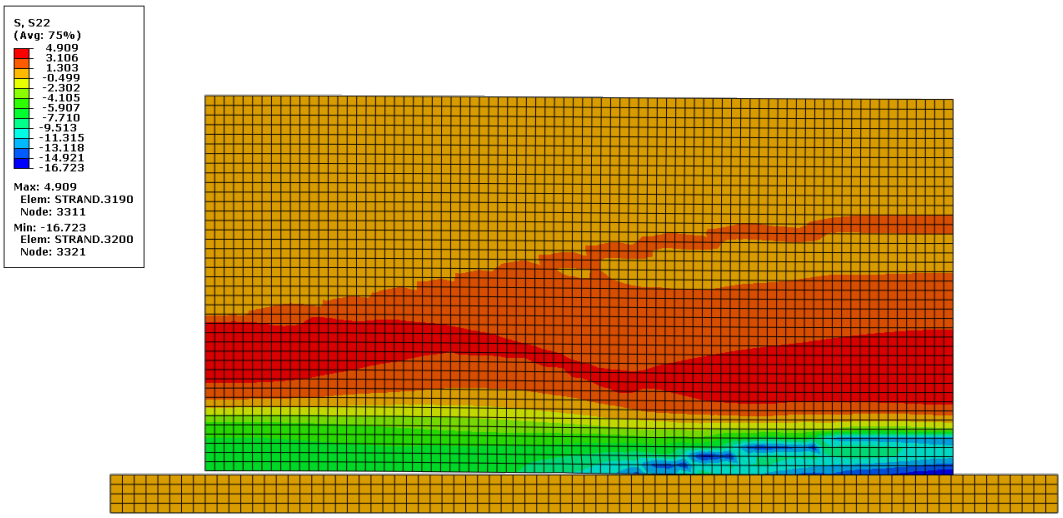

Figure 3.23: Slag finger stress results at 30 s (Unmagnified)

3.6 Conclusions

A thermal resistor model was developed to examine heat transfer phenomena within the interfacial gap during continuous casting. It was found that increasing slag layer thickness results in decreased heat flux across the gap. In addition results show that as solidification temperature decreases, the interface heat flux rises. Uniform flux layer thickness across the domain results in unform heat transfer as expected. Finally, the gap resistor model was applied together with the thermal-mechanical model to simulate a portion of solidifying steel shell in the mold, and showed the formation of a depression. Differences in flux layer thickness at the depression caused a drop in heat flux, higher surface temperatures, and a drop in shell thickness, which can result in necking phenomena in the solid shell as the stress from the shrinkage of the surrounding material concentrates in thinned shell regions.

3.7 Future Work

In combination with the solidification model discussed previously, this resistor model allows for fully coupled Thermal-Mechanical models of the continuous casting process. In addition it introduces the opportunity to alter the gap and thermal conditions throughout the entire mold. In this way we can examine the effect of uniform and non-uniform flux thickness variations, imposed air gaps, slag fingers, and a variety of other potential mold scenarios. This work treated radiation as an increased liquid conductivity, and while this is can be considered acceptable based on the assumptions discussed, inclusion of the radiation term is a potential are of future work. Air gaps are believed to only be able to form with a completely solid slag layer. If an air gap were to form in the presence of a still liquid slag layer, the gap might be filled with liquid from above and thus not have the same conductivity. Much further work applying this model is needed to understand depression and crack formation.

Chapter 4

Conclusions and Future Work

4.1 Conclusions

This work has developed and demonstrated 3 mathematical models in an effort to examine thermal and mechanical behavior in the mold region of the continuous casting process. A semi-one-dimensional model has been developed to study the effect of changes in steel grade early in the solidification process. General behavior has been discussed and explored, and similarities and differences have been noted. A thermal resistor model of the interfacial gap was developed to enable future coupled modeling work to extend this model into defect formation such as longitudinal cracks. Finally, these models have been combined into a two-dimensional model to explore depression formation and the effects of heat transfer variation across the surface of the mold.

Four different steel grades were investigated: Ultra-Low Carbon (0.003 %C), Low Carbon (0.04 %C), Peritectic (0.13 %C), and High Carbon (0.47 %C), simulating 30 s dwell times. Mesh refinement for capturing solidification details was examined and element sizes of 0.1 mm or smaller may be required to properly study solidification phenomena. All steel grades were found to follow the same general solidification behavior of compression at the surface increasing with time, and tension towards the solidification front. The initial solidification rate increases with carbon content. Thermal strain dominates the mechanical behavior. More stress and inelastic strain are generated in the high carbon steels, because they are mainly composed of high-strength austenite. Stress in the δ-ferrite phase is always very small, owing to the low strength of this phase. This simple model can

help in the calculation of taper profiles for different steel grades and maintain the desired contact with the mold. While fixed linear taper practices are common in industry, this work demonstrates that the desired profile of the shell is actually parabolic.

A thermal resistor model was developed to examine heat transfer phenomena within the interfacial gap during continuous casting. It was found that increasing slag layer thickness results in decreased heat flux across the gap. In addition results show that as solidification temperature decreases, the interface heat flux rises. Uniform flux layer thickness across the domain results in unform heat transfer as expected.

Finally, this work has demonstrated an example of combining the realistic thermal-resistor model of the gap together with the thermal-mechanical model to show the different local behavior that can occur at a depression. Differences in flux layer thickness at the depression caused a drop in heat flux, higher surface temperatures, and a drop in shell thickness, which can result in necking phenomena in the solid shell as the stress from the shrinkage of the surrounding material concentrates in thinned shell regions.

This work demonstrates the methodology necessary to model and capture the relevant behavior in a solidification problem; it also explores the basic property differences between steel grades according to the phase fractions and the properties of each phase, presents validation using analytical solutions, and a simulation of a continuous thin slab steel casting process where the shrinkage and solidification behavior of each grade is explored.

The increasing pressure and demands of the industry mean that new tools will always need to be developed to help expand and extrapolate our existing knowledge to keep up the pace. Increases in throughput are always a goal of manufacturers as long as it can be done effectively, without a loss of quality, and (especially in the case of steel plant operations) *safely*. With the information these models provide, better decisions, safer operating practices, and higher casting speeds can be realized.

In addition, it is the first step in demonstrating a transient 3-D model of thermal-mechanical behavior to examine the formation of cracks and depressions - where the correct behavior can be verified in a simplified case where an analytical solution exists, while allowing for extensions to higher dimensional modeling work in the future.

4.2 Future Work

The models developed in this work already provide a useful predictive tool and extensions of them will only increase their utility. The macroscopic models of thermal-mechanical behavior presented here should be combined together and applied to the entire strand. Next, more microscale behavior should be implemented, such as anisotropic behavior, cooling rate dependency. Then, in order to predict crack formation, damage criteria should be included. The detailed model used to investigate a single depression should be extended to investigate different cases, including grade variation, in order to identify the mechanisms for how individual depression-shaped defects are formed.

As mentioned previously, the complexities of the interfacial gap region make it quite difficult to study and model. In reality many of the conductivities and resistances are cooling rate based in addition to temperature dependency; furthermore the flux layer may be squeezed around and redistribute itself within the mold - implement better model for slag behavior in the gap by including for example the effect of flow due to squeezing when shell is forced against the mold, such as when taper is too high.

In the future a full quarter symmetry model of a slab may be used to examine the large scale behavior especially in the corner region, in addition, allowing the mold surface to distort within the model or including an already deformed mold shape may allows for study of asymmetries that otherwise may not have been seen.

The models developed in this work provide a useful starting point for exam-

ining continuous casting solidification. However, there is still a large gap in the ability to predict the formation of cracks and depressions, and missing knowledge regarding the crack sensitivity of peritectic steels. Breakouts at operating casters are extremely expensive and dangerous. Finding ways to understand and solve the root causes behind cracks and depressions, as well as the complexities of peritectics and newer grades, will lead to reductions in breakouts which will both save money and operational downtime, but more importantly keep employees safe.

Appendix A

Ferrostatic Pressure

A.1 Ferrostatic Pressure

In continuous casting, ferrostatic pressure is generally accepted as the primary force holding the solidfying shell in contact with the copper mold. This in contrast to the behavior of a pool of solidifying metal on a chilled surface and its tendency to freeze and bow upwards [128]. The ferrostatic pressure load is directly proportional to the depth below the meniscus, with the largest pressure experienced at the metallurgical length. The exact load may vary slightly from grade to grade with changes in density of the liquid steel, but it is on the order of magnitude of about 0.03 MPa.

Ferrostatic pressure is the continuous casting analog of hydrostatic pressure. From the top of the meniscus to the metallurgical length, the solidification front experiences this pressure as a result of the liquid steel pool above it. This ferrostatic pressure helps keep the solidifying shell in good contact with the mold copper, however the presence of ferrostatic pressure is not always enough to resist the shells attempts to pull away from the mold, especially in situations where there is local shell thinning or a drop in heat transfer.

This study demonstrates that in the general absence of ferrostatic pressure, the tendency for depression formation induced by a reduced heat transfer region is indeed substantially greater. This study also shows that application of the ferrostatic pressure as a traction on the liquid is feasible if setup correctly. It has also demonstrated that the difference between the pulling and pushing application is negligible for this model.

A.1.1 Magnitude

To examine the effect of ferrostatic pressure on the formation of depressions, the magnitude of the applied load was varied. A case was run with 10% of the expected value of the pressure applied to the domain. While this boundary condition is clearly not representative of casting on earth, it does allow us to imagine what the ferrostatic pressure is preventing or allowing.

A.1.2 Application Location

Application of the ferrostatic pressure in previous works has primarily applied it as a traction to the steel surface which contacts the mold as shown in Figure A.1. This applied traction pulls the steel shell towards the mold according to the ABAQUS user subroutine *DLOAD* and assuming a constant casting speed, is directly proportional to time below meniscus.

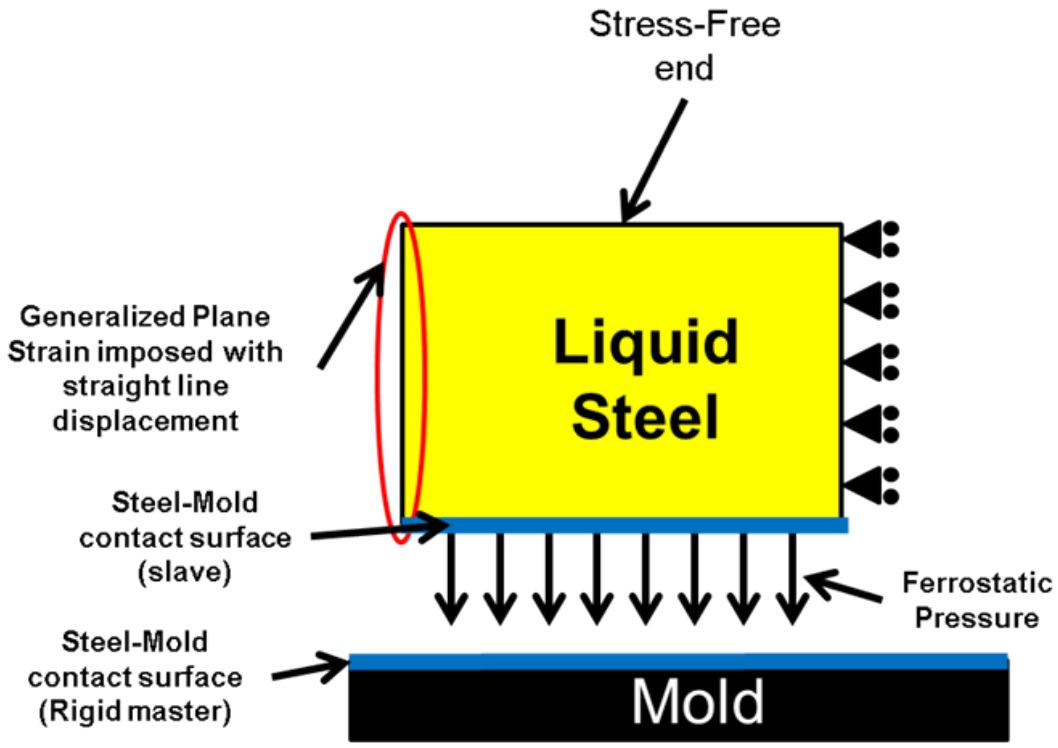

Figure A.1: Ferrostatic pressure applied pulling on domain

The purpose of this applied traction (as opposed to what some might consider more realistic in application on the solidification front) is primarily numerical simplification, and to ease the difficulties sometimes encountered with other methods such as tracking the liquid/solid boundary nodes, or large deformation of the weak liquid elements.

Application of the ferrostatic pressure using the pushing method is shown in Figure A.2. The steel-mold contact face is a free surface. The opposite face, has ferrostatic pressure traction applied.

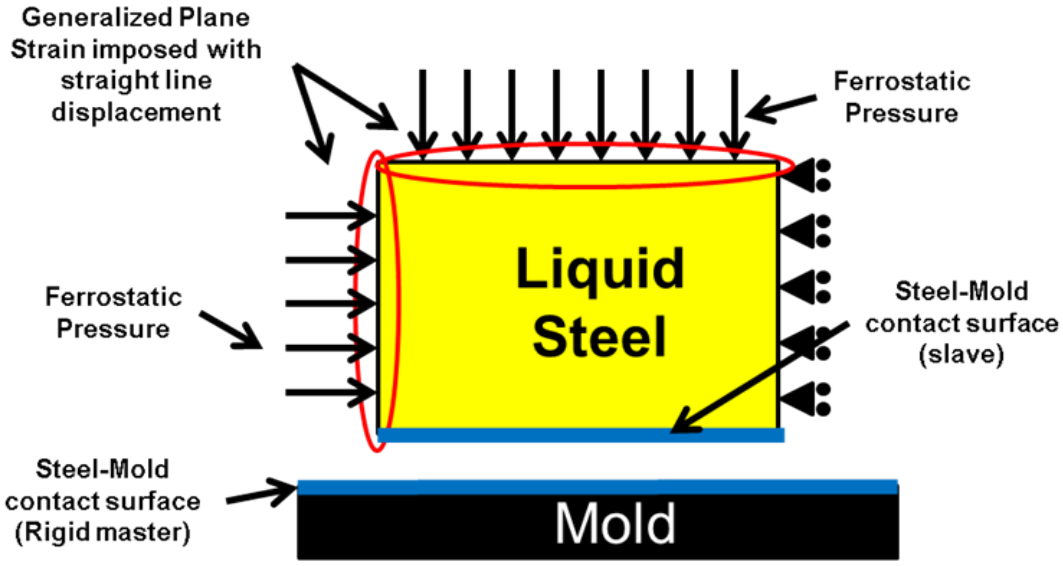

Figure A.2: Ferrostatic pressure applied pushing on domain

The free moving edge of the domain is constrained to remain vertical; However, when applying the ferrostatic pressure as a traction pushing on the free liquid surface, that surface also must be constrained to maintain a straight line.

Results of this small study are shown in Figure A.3. It was found that the size of the depression observed with ferrostatic pressure applied pushing on the liquid, it was observed that the size of the depression was about 10% smaller than when it pulls on the surface. This demonstrates that this method of ferrostatic pressure application is reasonable for this situation.

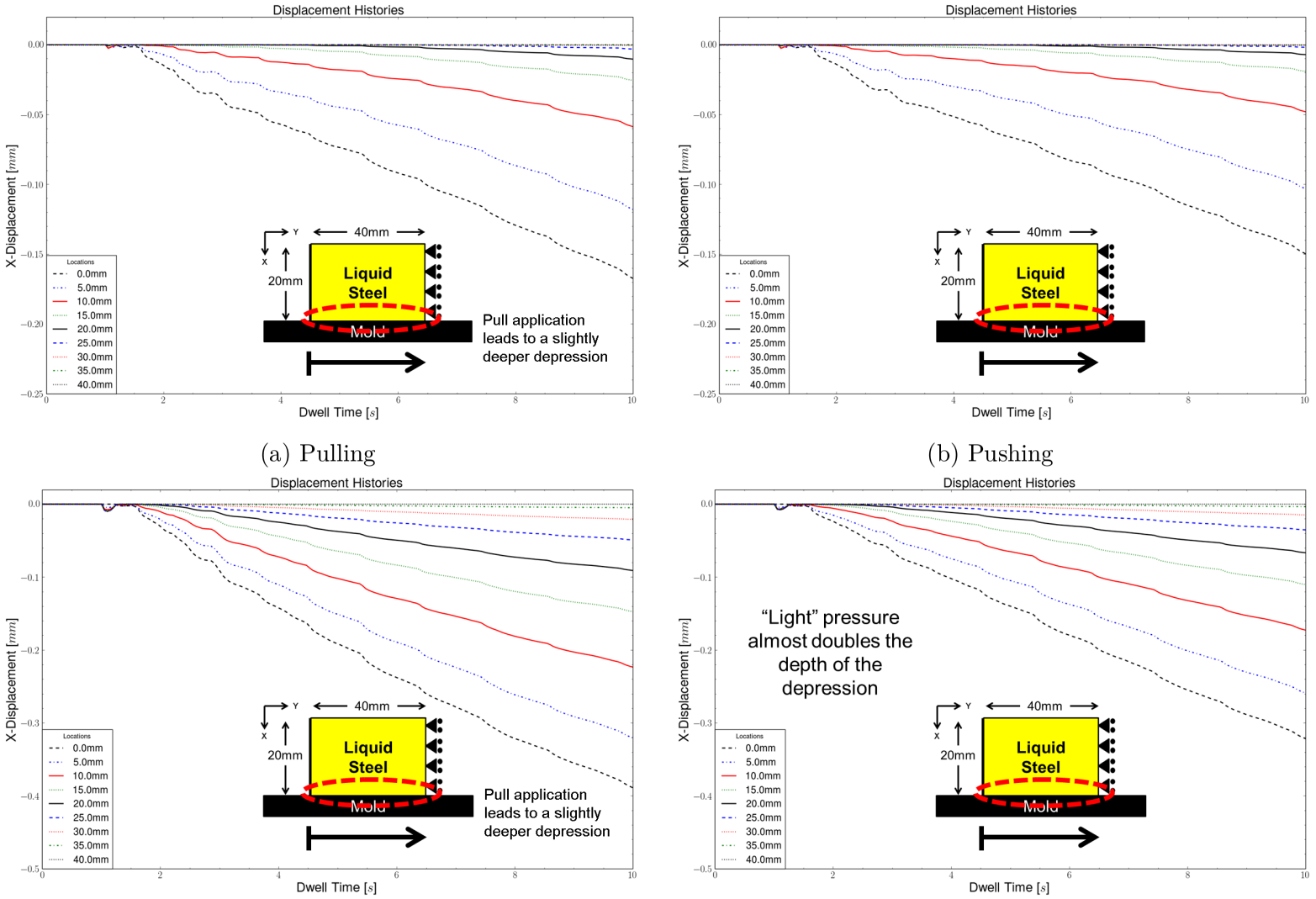

(a) Pulling

(b) Pushing

(c) 10% Pulling

(d) 10% Pushing

Figure A.3: Results of varied ferrostatic pressure application

Appendix B

ABAQUS Operational Notes, Input Files & Scripts

During the course of this work, the author has spent considerable time troubleshooting and exploring solidification modeling using ABAQUS commercial finite element software. This appendix contains some notes and recommendations for its successful operations, as well as example input files for the work conducted. The importance of reading and understanding the documentation cannot be emphasized enough, for convenience portions of this chapter contain large excerpts (some summarized) from the ABAQUS documentation collection.

There is also a section containing the following codes: ABAQUS input files, the GAPCON subroutine written in FORTRAN, and examples of Python script files that can be used to run batch jobs for parametric studies, subject to the following copyright:

Copyright (c) <2016> <Matthew L.S. Zappulla> Permission is hereby granted, free of charge, to any person obtaining a copy of this software and associated documentation files (the "Software"), to deal in the Software without restriction, including without limitation the rights to use, copy, modify, merge, publish, distribute, sublicense, and/or sell copies of the Software, and to permit persons to whom the Software is furnished to do so, subject to the following conditions: The above copyright notice and this permission notice shall be included in all copies or substantial portions of the Software. THE SOFTWARE IS PROVIDED "AS IS", WITHOUT WARRANTY OF ANY KIND, EXPRESS OR IMPLIED, INCLUDING BUT NOT LIMITED TO THE WARRANTIES OF MERCHANTABILITY, FITNESS FOR A PARTICULAR PURPOSE AND NONINFRINGEMENT. IN NO EVENT SHALL THE AUTHORS OR COPYRIGHT HOLDERS BE LIABLE FOR ANY CLAIM, DAMAGES OR OTHER LIABILITY, WHETHER IN AN ACTION OF CONTRACT, TORT OR OTHERWISE, ARISING FROM, OUT OF OR IN CONNECTION WITH THE SOFTWARE OR THE USE OR OTHER DEALINGS IN THE SOFTWARE.

B.1 Contact

B.1.1 Contact Variables

ABAQUS allows for output of many of it's internal variables used during calculation. For contact specifically there are dozens of possible output variables in addition to the defaults for a standard analysis. These variables are highly useful for understanding results, especially when it comes to contact problems.

On a nodal basis, Nodal Contact Area, CNAREA, multiplied by the Contact Shear Force, CSHEARF, will yield the frictional shear stress, CSHEAR. However, Frictional Shear Stress is not equal to Shear Stress $S12$, therefore using $S12$ with the nodal contact area in an attempt to figure out the contact shear force is not correct.

B.1.2 Notation

ABAQUS reports the values of tangential variables (frictional shear stress, viscous shear stress, and relative tangential motion) with respect to the slip directions defined on the surfaces. This may seem like a trivial statement but in situations where a rotated coordinate system might be used, this becomes consequential.

The number at the end of a variable's name indicates whether the variable corresponds to the first or second slip direction. For example,ÂăCSHEAR1Âăis the frictional shear stress component in the first slip direction, whileÂăCSHEAR2Âăis the frictional shear stress component in the second slip direction. 1 and 2 are NOT necessarily X and Y.

Local tangent directions on a contact surface (sometimes called "slip directions") are a reference orientation by which ABAQUS calculates tangential behavior in a contact interaction.

Finite-sliding, surface-to-surface formulation:ÂăThe default initial orientations of the two local tangent directions are based on the slave surface normal with the assumption that the contact normal corresponds to the negative normal to the

slave surface.

Two-dimensional models have only one local tangent direction. Abaqus/Standard defines the orientation of this direction by the cross product of the vector into the plane of the model $(0.0, 0.0, 1.0)$ and the contact normal vector.

Therefore, the positive contact variable orientation is in the positive Y direction.

B.2 Frictional Force Balance

This section explains the proper force balance on a global model level, as well as the local nodal level. Local nodal and global forces do balance in the model, however, confirming these to be true is not trivial without understanding the notation used by ABAQUS when it comes to output. Local nodal force balance is described in depth in Figure B.1 and the global model force balance is described in Figure B.2.

B.2.1 Stabilization

Well constrained and defined models with carefully chosen applied tractions and displacments avoid situations where arbitrary rigid body motion may be encountered. For contact problems ABAQUS includes tools called contact controls, signified by keyword "*CONTACT CONTROLS" within the input file. It is recommended by the documentation that this parameter be included to help in situations where rigid body motion may occur until contact is fully established.

This option is used to provide additional optional solution controls for models involving contact between bodies. HOWEVER, the standard solution controls are usually sufficient, unless there is a substantial amount of unconstrained rigid body motion. For example: if the ferrostatic pressure application is deferred, there is no constraint preventing the steel shell from translating normal to the mold surface. This method is ok as long as the defferal time is short (e.g. less than about 1 second), any longer than this, and the surfaces may start to separate, creating

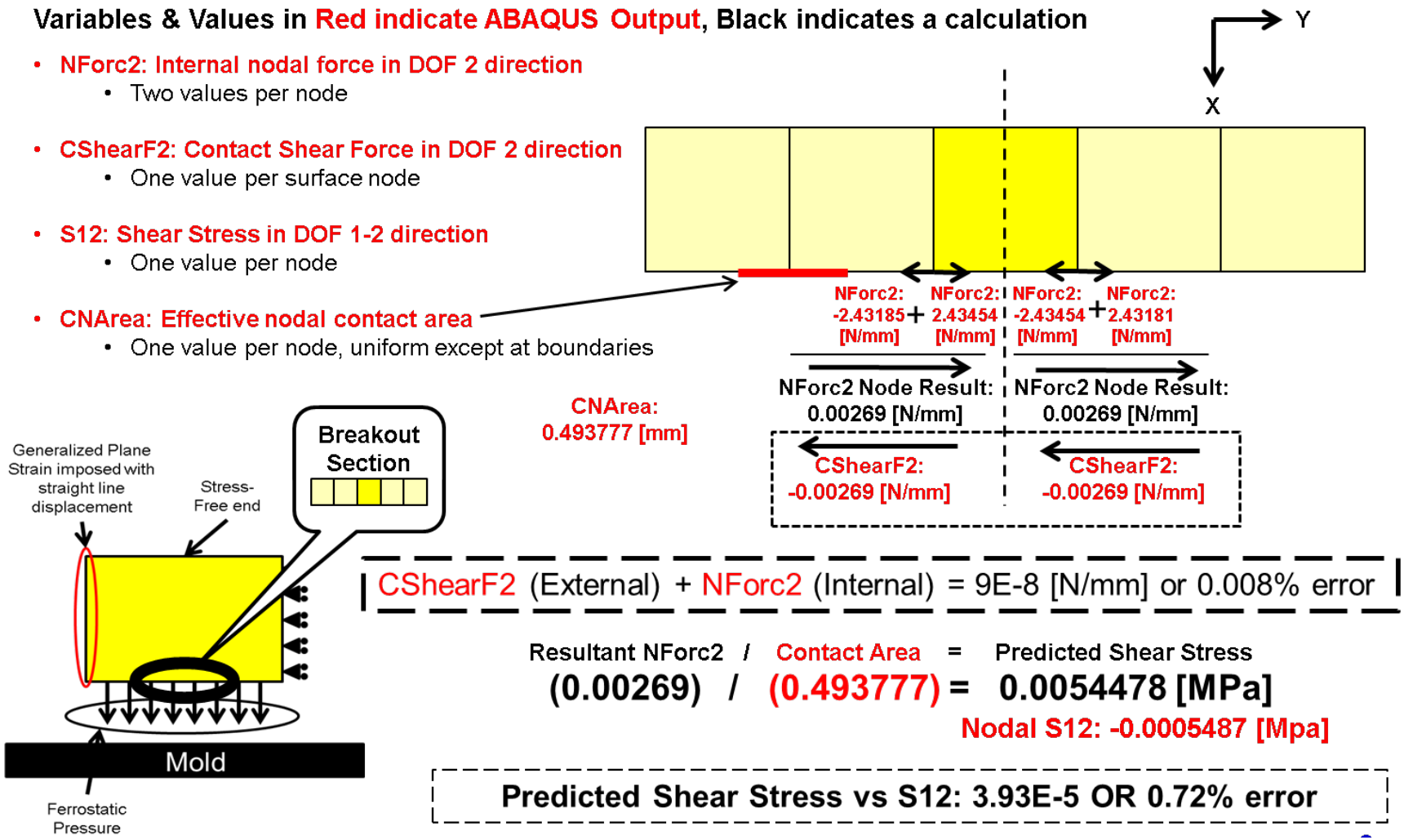

Figure B.1: Internal force balance at 10 s

Variables in Red indicate ABAQUS Output, Black indicates my calculation

- **Ferrostatic Pressure Force = Contact Pressure * Area**
  - Sum of nodal values taken along interface
- **CNormF1: Contact Normal Force in DOF direction 1**
  - Sum of nodal values taken along interface
- **CShearF2: Contact Shear Force in DOF direction 2**
  - Sum of nodal values taken along interface
- **RF2: Reaction Force in DOF direction 2**
  - Sum of nodal values taken along fixed edge

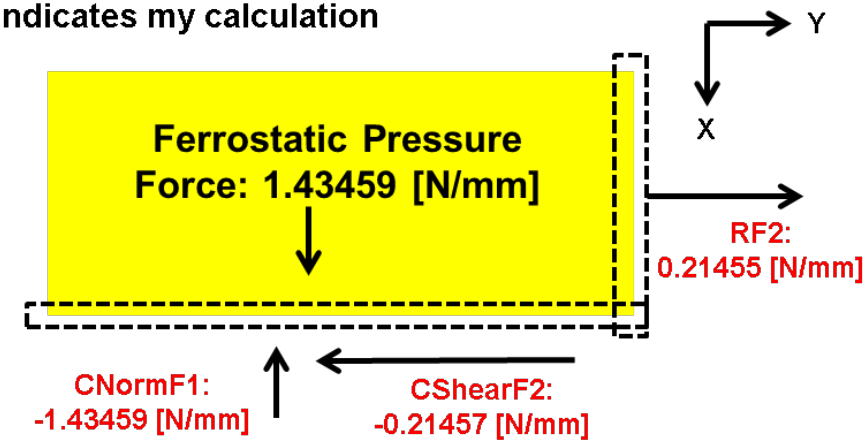

X Direction Force Balance: CNormF1 + Ferrostatic Pressure Force = -1.43459 + 1.43459 = **1E-7 OR 0.00000697% error**

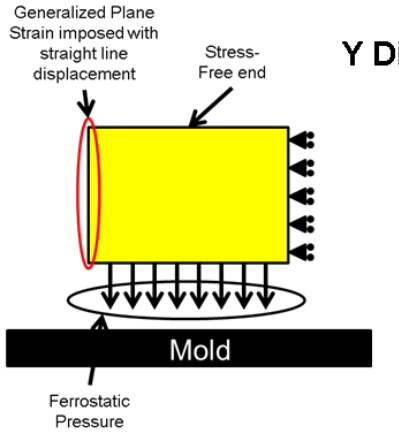

Y Direction Force Balance: CShearF2 + RF2 = -0.21457 + 0.21455 = **2E-5 OR 0.009% error**

Ferrostatic Force * Frictional Coefficient = **Predicted Frictional force**

(1.43459) * (0.15) = 0.21518 [N/mm]

Predicted Frictional Force vs CShearF2: 6.39E-4 OR 0.30% error

Figure B.2: External force balance at 10 s

not only a non physical situation, but when the traction is finally applied on the surface, the contact interaction will change abruptly.

It works by activating damping in the normal and tangential directions based on the stiffness of the underlying mesh and the time step size. If no value is assigned to this parameter, ABAQUS calculates the damping coefficient automatically. If a numerical value is assigned to this parameter, ABAQUS multiplies the automatically calculated damping coefficient by this value.

Used improperly this is dangerous In solidification contact problems, this parameter can be disastrous. For example: Non physical small displacements of contact surfaces can occur and lead to depression formation in the presence of completely uniform heat transfer. The lower the amount of stabilization applied the better.

Heed the warning in the documentation: *Warning: These controls are intended for experienced analysts and should be used with care. Using nondefault values of these controls may greatly increase the computational time of the analysis or produce inaccurate results.*

Abaqus/Standard offers contact stabilization to help automatically control rigid body motion in static problems before contact closure and friction restrain such motion.

It is recommended that you first try to stabilize rigid body motion through modeling techniques (modifying geometry, imposing boundary conditions, etc.). The automatic stabilization capability is meant to be used in cases in which it is clear that contact will be established, but the exact positioning of multiple bodies is difficult during modeling. It is not meant to simulate general rigid body dynamics; nor is it meant for contact chattering situations or to resolve initially tight clearances between mating surfaces.

Although the automatically calculated damping coefficient typically provides enough damping to eliminate the rigid body modes without having a major effect on the solution, there is no guarantee that the value is optimal or even suitable.

There are several ways to carry out such checks. The simplest method is to

consider the ratio between the energy dissipated by viscous damping and a more general energy measure for the model, such as the elastic strain energy. These quantities can be obtained as output variables $ALLSD$ and $ALLSE$, respectively.

More detailed information can be obtained by comparing the contact damping stresses $CDSTRESS$ (with the individual components $CDPRESS$, $CDSHEAR1$, and $CDSHEAR2$) to the true contact stresses $CSTRESS$ (with the individual components $CPRESS$, $CSHEAR1$, and $CSHEAR2$).

If the contact damping stresses are too high, you should decrease the damping. The comparison should be made after contact is firmly established; the contact damping stresses will always be relatively high when contact is not yet or only partially established.

The easiest way to increase or decrease the amount of damping is to specify a factor by which the automatically calculated damping coefficient will be multiplied. Typically, you should initially consider changing the default damping by (at least) an order of magnitude; if that addresses the problem sufficiently, you can do some subsequent fine-tuning. In some cases a larger or smaller factor may be needed; this is not a problem as long as a converged solution is obtained and the dissipated energy and contact damping stresses are sufficiently small. However, this is a relative statement, and "sufficiently small" depends directly on the problem being modeled.

It is also possible to specify the damping coefficient directly. Direct specification of the damping value is not easy and may require some trial and error.

B.3 Example Input Files

B.3.1 Example Heat Transfer Input Files

```
**#############################################################################*
**                                                                            #*
**        BASIC INPUT FILE TEMPLATE FOR 1D SOLIDIFICATION STRESS PROBLEM      #*
```

```
**                                                                              #*
**           THIS FILE IS INTENDED FOR USE WITH THE CCC USER SUBROUTINE FILES    #*
**             THAT CONTAIN THE MECHANICAL AND THERMAL UMAT, AS WELL AS THE      #*
**            USER THERMAL EXPANSION FUNCTIONS , AND USER DEFINED HEAT FLUX      #*
**                                                                              #*
**      CREATED BY MATTHEW L.S. ZAPPULLA AND LANCE C. HIBBELER, OCTOBER 2014     #*
**                                                                              #*
**################################################################################*

*PARAMETER
 EX = 400
 EY = 3
 LENGTH = 40.0
 WIDTH = (LENGTH/EX)*EY
**--------------------------------------------------------------------------------**
**                    MESH DEFINITION  -  LINEAR ELEMENTS                       **
**--------------------------------------------------------------------------------**
*PART, NAME=SLICE_L
  *PARAMETER
   L_NX = EX+1
   L_NY = EY+1
   L_SW = 1
   L_SE = L_NX
   L_NE = L_NX*L_NY
   L_NW = L_NE-L_NX+1
   L_ND_REF = L_NE+1
   L_DX = LENGTH/EX
   L_DY = WIDTH/EY
   L_Y_BOT  = -0.5*WIDTH
   L_Y_TOP  =  0.5*WIDTH
   L_ME_SW = 1
   L_ME_SE = 2
   L_ME_NW = L_NX+1
   L_ME_NE = L_NX+2
   L_E_NE = (EX*EY)-EX+1
  *NODE
   <L_SW>, 0.0, <L_Y_BOT>
   <L_NW>, 0.0, <L_Y_TOP>
  *NGEN, NSET=WALL
   <L_SW>, <L_NW>, <L_NX>
  *NODE
   <L_SE>, <LENGTH>, <L_Y_BOT>
   <L_NE>, <LENGTH>, <L_Y_TOP>
  *NGEN, NSET=FREE
   <L_SE>, <L_NE>, <L_NX>
```

```
  *NFILL, NSET=ALL
   WALL, FREE, <EX>, 1
  *NODE, NSET=RP
   <L_ND_REF>, 0.0, 0.0
  *NSET, NSET=TOP_EDGE, GENERATE
   <L_NW>, <L_NE>, 1
  *NSET, NSET=GPE_EDGE, GENERATE
   2, <L_SE>, 1
  *ELEMENT, TYPE=DC2D4
   1, <L_ME_SW>, <L_ME_SE>, <L_ME_NE>, <L_ME_NW>
  *ELGEN, ELSET=ALL
   1, <EX>, 1, 1, <EY>, <L_NX>, <EX>
  *ELSET, ELSET=WALL, GENERATE
   1, <L_E_NE>, <EX>
  *SURFACE, NAME=WALL, TYPE=ELEMENT
   WALL, S4
  *SOLID SECTION, ELSET=ALL, MATERIAL=STEEL
   1.0
*END PART

**----------------------------------------------------------------------------**
**                            ASSEMBLY DEFINITION                             **
**----------------------------------------------------------------------------**
*ASSEMBLY, NAME=ASSEMBLY
  *INSTANCE, NAME=STRAND, PART=SLICE_L
   0.0, 0.0
  *END INSTANCE
  ** *EQUATION
   ** 2
   ** STRAND.GPE_EDGE, 2, 1.0, STRAND.1, 2, -1.0
*END ASSEMBLY



*MATERIAL, NAME=Steel
*DENSITY
 7.5e-09,
*EXPANSION, USER, TYPE=ISO
*USER MATERIAL, CONSTANTS=0, TYPE=THERMAL
*USER MATERIAL, CONSTANTS=0, TYPE=MECHANICAL
*DEPVAR
   20
    1, FL,    "FRACTION LIQUID"
    2, FD,    "FRACTION DELTA"
    3, FG,    "FRACTION GAMMA"
```

```
    4, FA,    "FRACTION ALPHA"
    5, EE11,  "ELASTIC STRAIN 11"
    6, EE22,  "ELASTIC STRAIN 22"
    7, EE33,  "ELASTIC STRAIN 33"
    8, EE12,  "ELASTIC STRAIN 12"
    9, EEBAR, "EFFECTIVE ELASTIC STRAIN"
   10, EP11,  "PLASTIC STRAIN 11"
   11, EP22,  "PLASTIC STRAIN 22"
   12, EP33,  "PLASTIC STRAIN 33"
   13, EP12,  "PLASTIC STRAIN 12"
   14, EPBAR, "EFFECTIVE PLASTIC STRAIN"
   15, EPDOT, "EFFECTIVE PLASTIC STRAIN RATE"
   16, EF11,  "FLUID STRAIN 11"
   17, EF22,  "FLUID STRAIN 22"
   18, EF33,  "FLUID STRAIN 33"
   19, EF12,  "FLUID STRAIN 12"
   20, EFBAR, "EFFECTIVE FLUID STRAIN"
*PHYSICAL CONSTANTS, ABSOLUTE ZERO=-273.15, STEFAN BOLTZMANN=56.704e-09
**
**********************************************************************
**                      PREDEFINED FIELDS                            *
**********************************************************************
**
*Initial Conditions, type=TEMPERATURE
STRAND.ALL, 1543.0
*Initial Conditions, type=solution, user
**
**********************************************************************
**                      STEP DEFINITION                             *
**********************************************************************
**
*Step, name=ANALYSIS, inc=1000000
*HEAT TRANSFER, DELTMX = 0.5
1e-08, 30.0, 1e-30, 0.01
*CONTROLS, ANALYSIS=DISCONTINUOUS
*CONTROLS, PARAMETERS=TIME INCREMENTATION
10, , ,20,8,5, ,20, , , , ,
0.24,0.4,0.5, , ,0.2, ,
**
**
**********************************************************************
**                              LOADS                                *
**********************************************************************
*Dsflux
STRAND.WALL, SNU, 1.0
```

```
**
**************************************************************************
**                              OUTPUT                                  *
**************************************************************************
  *RESTART, WRITE, OVERLAY, NUMBER INTERVAL=250
  *OUTPUT, FIELD, TIME INTERVAL=0.01
    *NODE OUTPUT, NSET=STRAND.ALL
     NT, UT
    *ELEMENT OUTPUT, ELSET=STRAND.ALL
     HFL, S, E, THE, EE, SDV
  *OUTPUT, DIAGNOSTICS=NO
*END STEP
```

B.3.2 Example Stress Input Files

```
**############################################################################*
**                                                                           #*
**         BASIC INPUT FILE TEMPLATE FOR 1D SOLIDIFICATION STRESS PROBLEM    #*
**                                                                           #*
**           THIS FILE IS INTENDED FOR USE WITH THE CCC USER SUBROUTINE FILES #*
**             THAT CONTAIN THE MECHANICAL AND THERMAL UMAT, AS WELL AS THE   #*
**            USER THERMAL EXPANSION FUNCTIONS , AND USER DEFINED HEAT FLUX   #*
**                                                                           #*
**      CREATED BY MATTHEW L.S. ZAPPULLA AND LANCE C. HIBBELER, OCTOBER 2014 #*
**                                                                           #*
**############################################################################*


*PARAMETER
 EX = 400
 EY = 3
 LENGTH = 40.0
 WIDTH = (LENGTH/EX)*EY
**----------------------------------------------------------------------------**
**                    MESH DEFINITION  -  LINEAR ELEMENTS                     **
**----------------------------------------------------------------------------**
*PART, NAME=SLICE_L
  *PARAMETER
   L_NX = EX+1
   L_NY = EY+1
   L_SW = 1
   L_SE = L_NX
```

```
   L_NE = L_NX*L_NY
   L_NW = L_NE-L_NX+1
   L_ND_REF = L_NE+1
   L_DX = LENGTH/EX
   L_DY = WIDTH/EY
   L_Y_BOT  = -0.5*WIDTH
   L_Y_TOP  =  0.5*WIDTH
   L_ME_SW = 1
   L_ME_SE = 2
   L_ME_NW = L_NX+1
   L_ME_NE = L_NX+2
   L_E_NE = (EX*EY)-EX+1
  *NODE
   <L_SW>, 0.0, <L_Y_BOT>
   <L_NW>, 0.0, <L_Y_TOP>
  *NGEN, NSET=WALL
   <L_SW>, <L_NW>, <L_NX>
  *NODE
   <L_SE>, <LENGTH>, <L_Y_BOT>
   <L_NE>, <LENGTH>, <L_Y_TOP>
  *NGEN, NSET=FREE
   <L_SE>, <L_NE>, <L_NX>
  *NFILL, NSET=ALL
   WALL, FREE, <EX>, 1
  *NODE, NSET=RP
   <L_ND_REF>, 0.0, 0.0
  *NSET, NSET=TOP_EDGE, GENERATE
   <L_NW>, <L_NE>, 1
  *NSET, NSET=GPE_EDGE, GENERATE
   2, <L_SE>, 1
  *ELEMENT, TYPE=CPEG4H
   1, <L_ME_SW>, <L_ME_SE>, <L_ME_NE>, <L_ME_NW>
  *ELGEN, ELSET=ALL
   1, <EX>, 1, 1, <EY>, <L_NX>, <EX>
  *ELSET, ELSET=WALL, GENERATE
   1, <L_E_NE>, <EX>
  *SURFACE, NAME=WALL, TYPE=ELEMENT
   WALL, S4
  *SOLID SECTION, ELSET=ALL, MATERIAL=STEEL, REF NODE=RP
   1.0
*END PART

**------------------------------------------------------------------------**
**                          ASSEMBLY DEFINITION                           **
**------------------------------------------------------------------------**
```

```
*ASSEMBLY, NAME=ASSEMBLY
  *INSTANCE, NAME=STRAND, PART=SLICE_L
   0.0, 0.0
  *END INSTANCE
  *EQUATION
   2
   STRAND.GPE_EDGE, 2, 1.0, STRAND.1, 2, -1.0
*END ASSEMBLY


*MATERIAL, NAME=Steel
*DENSITY
 7.5e-09,
*EXPANSION, USER, TYPE=ISO
*USER MATERIAL, CONSTANTS=0, TYPE=THERMAL
*USER MATERIAL, CONSTANTS=0, TYPE=MECHANICAL
*DEPVAR
   20
    1, FL,    "FRACTION LIQUID"
    2, FD,    "FRACTION DELTA"
    3, FG,    "FRACTION GAMMA"
    4, FA,    "FRACTION ALPHA"
    5, EE11,  "ELASTIC STRAIN 11"
    6, EE22,  "ELASTIC STRAIN 22"
    7, EE33,  "ELASTIC STRAIN 33"
    8, EE12,  "ELASTIC STRAIN 12"
    9, EEBAR, "EFFECTIVE ELASTIC STRAIN"
   10, EP11,  "PLASTIC STRAIN 11"
   11, EP22,  "PLASTIC STRAIN 22"
   12, EP33,  "PLASTIC STRAIN 33"
   13, EP12,  "PLASTIC STRAIN 12"
   14, EPBAR, "EFFECTIVE PLASTIC STRAIN"
   15, EPDOT, "EFFECTIVE PLASTIC STRAIN RATE"
   16, EF11,  "FLUID STRAIN 11"
   17, EF22,  "FLUID STRAIN 22"
   18, EF33,  "FLUID STRAIN 33"
   19, EF12,  "FLUID STRAIN 12"
   20, EFBAR, "EFFECTIVE FLUID STRAIN"
*PHYSICAL CONSTANTS, ABSOLUTE ZERO=-273.15, STEFAN BOLTZMANN=56.704e-09
**
**********************************************************************
**                      PREDEFINED FIELDS                           *
**********************************************************************
**
*Initial Conditions, type=TEMPERATURE
```

```
STRAND.ALL, 1543.0
*Initial Conditions, type=solution, user
**
**********************************************************************
**                      STEP DEFINITION                              *
**********************************************************************
**
*Step, name=STRESS, inc=1000000
*STATIC
1e-08, 30.0, 1e-30, 0.01
*CONTROLS, ANALYSIS=DISCONTINUOUS
*CONTROLS, PARAMETERS=TIME INCREMENTATION
10, , ,20,8,5, ,20, , , , ,
0.24,0.4,0.5, , ,0.2, ,
**
**********************************************************************
**                      BOUNDARY CONDITIONS                          *
**********************************************************************
**
*Boundary
STRAND.Top_EDGE, 2, 2, 0.0
STRAND.RP, 4, 5, 0.0
STRAND.Wall, 1, 1, 0.0
**
**********************************************************************
**                              LOADS                                *
**********************************************************************
*TEMPERATURE, FILE=CC1FHT400LC

**********************************************************************
**                              OUTPUT                               *
**********************************************************************
  *RESTART, WRITE, OVERLAY, NUMBER INTERVAL=250
  *OUTPUT, FIELD, TIME INTERVAL=0.01
    *NODE OUTPUT, NSET=STRAND.ALL
     NT, UT
    *ELEMENT OUTPUT, ELSET=STRAND.ALL
     HFL, S, E, THE, EE, SDV
  *OUTPUT, DIAGNOSTICS=NO
*END STEP
```

B.4 GAPCON for Resistor Model

The full details for GAPCON can be found in the ABAQUS User Subroutine Reference Guide [18]. The subroutine allows for the definition of k_{Gap} as a function of other input parameters. It assumes that the heat transfer between surfaces is modeled as $q'' = k_{Gap}(T_{Master} - T_{Slave})$, where q'' is the heat flux per unit area flowing between corresponding points on the master and slave surfaces, k_{Gap} is the gap conductance, and T_{Master} and T_{Slave} are the master and slave surface temperature respectively. GAPCON is called for every increment at the slave nodes of a contact pair, in our case this means it is called for every node on the surface of the steel shell.

Note about ABAQUS environment: Within a subroutine call once a variable has been set to a value. Either initially, or from a previous calculation increment, it holds that value until it is set to a different value, is cleared, or the simulation is terminated. *However, each time a subroutine call is returned the stored values disappear. In order to make a variable value persist across subroutine calls the FORTRAN "save" keyword is necessary.* This is particularly important for the flag used in the example code to track whether the entire flux layer has become solid.

```
CCCCCCCCCCCCCCCCCCCCCCCCCCCCCCCCCCCCCCCCCCCCCCCCCCCCCCCCCCCCCCCCCCCCCCCCCC
C                                                                      C
C           INTERNAL ABAQUS GAP CONDUCTIVITY SUBROUTINE                C
C                                                                      C
C                 TEMPERATURE VARYING PROPERTIES                       C
C              SOLID/LIQUID FLUX AND AIR GAP FORMATION                 C
C                                                                      C
C            CREATED BY MATTHEW L.S. ZAPPULLA, MARCH 2016              C
C                                                                      C
CCCCCCCCCCCCCCCCCCCCCCCCCCCCCCCCCCCCCCCCCCCCCCCCCCCCCCCCCCCCCCCCCCCCCCCCCC


      SUBROUTINE GAPCON(AK,D,FLOWM,TEMP,PREDEF,TIME,CINAME,SLNAME,
```

```
     1                 MSNAME,COORDS,NOEL,NODE,NPRED,KSTEP,KINC)

      INCLUDE 'ABA_PARAM.INC'
      CHARACTER*80 CINAME,SLNAME,MSNAME
      DIMENSION AK(5),D(2), FLOWM(2), TEMP(2), PREDEF(2,*),
     1 TIME(2), COORDS(3)

      DOUBLE PRECISION DGAP, DAIR, DSOL, DLIQ, SLAG
      DOUBLE PRECISION LiqThresh, AirThresh
      DOUBLE PRECISION TMOLD, TSHELL, TCRYSTAL, TMC, TLS
      DOUBLE PRECISION KAIR, KLIQ, KSOL
      DOUBLE PRECISION RAIR, RSOL, RLIQ, RTOT, RGAP
      DOUBLE PRECISION ShellIntR, RCONTACT
      DOUBLE PRECISION HGAP
      DOUBLE PRECISION FLAG
      DOUBLE PRECISION ITER, ITERS
      DOUBLE PRECISION STARTCOORD, ENDCOORD, STARTVAL, ENDVAL
      INTEGER KINC
      SAVE FLAG, TLS, TMC

CCCCCCCCCCCCCCCCCCCCCCCCCCCCCCCCCCCCCCCCCCCCCCCCCCCCCCCCCCCCCCCCCCCCCC
C  DEFINE PARAMETERS
CCCCCCCCCCCCCCCCCCCCCCCCCCCCCCCCCCCCCCCCCCCCCCCCCCCCCCCCCCCCCCCCCCCCCC
      TCRYSTAL = 1030.0D0   !FLUX CRYSTALLIZATION TEMPERATURE, DEG C

      KSOL = 0.5D0          !FIXED CONDUCTIVITY OF THE SOLID SLAG
      KLIQ = 3.0D0          !FIXED CONDUCTIVITY OF THE LIQUID SLAG

      ITER = 0.0D0          !SET THE ITERATION COUNTER TO ZERO
      ITERS = 20.0D0       !TOTAL NUMBER OF ITERATIONS

      LiqThresh = 0.00001D0 !MINIMUM LIQUID THRESHOLD SIZE [m]
      AirThresh = 0.00001D0 !MINIMUM AIR GAP THRESHOLD SIZE [m]



      IF (COORDS(2).LE.-15.0D0) THEN
        SLAG = 0.001D0
      ELSE
        SLAG = 0.002D0        !DEFINE THE SLAG LAYER THICKNESS
      END IF

   IF USING THE INPUT FILE TEMPLATE OF ZAPPULLA AND HIBBELER
   THE DOMAIN IS CENTERED AT 0, SO ALL NEGATIVE Y COORDINATES ARE
   IN THE DIRECTION OF THE DEPRESSION CENTERLINE
```

```
CCCCCCCCCCCCCCCCCCCCCCCCCCCCCCCCCCCCCCCCCCCCCCCCCCCCCCCCCCCCCCCCCCCC
C  UNPACK VALUES FROM ABAQUS
CCCCCCCCCCCCCCCCCCCCCCCCCCCCCCCCCCCCCCCCCCCCCCCCCCCCCCCCCCCCCCCCCCCC
      TSHELL = TEMP(1)  ! SLAVE SURFACE TEMPERATURE
      TMOLD  = TEMP(2)  ! MASTER SURFACE TEMPERATURE
CCCCCCCCCCCCCCCCCCCCCCCCCCCCCCCCCCCCCCCCCCCCCCCCCCCCCCCCCCCCCCCCCCCC
C  THERMAL RESISTANCE OF AIR GAP
CCCCCCCCCCCCCCCCCCCCCCCCCCCCCCCCCCCCCCCCCCCCCCCCCCCCCCCCCCCCCCCCCCCC

      DAIR = D(1)/1000.0D0

      IF (DAIR.LE.AirThresh) THEN
        DAIR = 0.0D0
        RAIR = 0.0D0
      ELSE
        DAIR = DAIR
        KAIR = 6.0D-2  ! mW/(mm*K)
        RAIR = DAIR/KAIR
      END IF

      DGAP   = SLAG     ! GAP SIZE

      IF (TSHELL.GT.1532.0D0) THEN
        TLS = 1400.0D0
        TMC = 250.0D0
        RSOL = (DGAP/2)/KSOL
        RLIQ = (DGAP/2)/KLIQ
        FLAG = 0.0D0
      END IF


CCCCCCCCCCCCCCCCCCCCCCCCCCCCCCCCCCCCCCCCCCCCCCC
C  MOLD-FLUX INTERFACE CONTACT RESISTANCE
CCCCCCCCCCCCCCCCCCCCCCCCCCCCCCCCCCCCCCCCCCCCCCC
      RCONTACT = 1.0D0/2500.0D0 !m2K/W


      IF (FLAG.EQ.1.0D0) THEN

        DSOL = DGAP
        RSOL = DSOL/KSOL
        ShellIntR = 1.0D0/1000.0D0
        RTOT = RCONTACT + RSOL + ShellIntR + RAIR
```

```
        TMC = TMOLD+(TSHELL-TMOLD)*(RCONTACT/RTOT)
        TLS = (TMC+(TSHELL-TMOLD)*((RSOL+RAIR)/RTOT))
        GOTO 1738
      END IF

CCCCCCCCCCCCCCCCCCCCCCCCCCCCCCCCCCCCCCCCCCCCCCCCCCCCCCCCCCCCCCCCCCCCCCC
CCCCCCCCCCCCCCCCCCCCCCCCCCCCCCCCCCCCCCCCCCCCCCCCCCCCCCCCCCCCCCCCCCCCCCC
C   START OF THE GAP LAYER ITERATION LOOP
CCCCCCCCCCCCCCCCCCCCCCCCCCCCCCCCCCCCCCCCCCCCCCCCCCCCCCCCCCCCCCCCCCCCCCC
CCCCCCCCCCCCCCCCCCCCCCCCCCCCCCCCCCCCCCCCCCCCCCCCCCCCCCCCCCCCCCCCCCCCCCC

      DO WHILE(ITER.LT.ITERS)

CCCCCCCCCCCCCCCCCCCCCCCCCCCCCCC
C   SHELL INTERFACE RESISTANCE
CCCCCCCCCCCCCCCCCCCCCCCCCCCCCCC
          ShellIntR = (3.8981D0*DEXP(0.0054D0*TLS))
          IF (ShellIntR.LT.1000.0D0) THEN
            ShellIntR = 1000.0D0
          END IF
          IF (ShellIntR.GT.20000.0D0) THEN
            ShellIntR = 20000.0D0
          END IF

          ShellIntR = 1.0D0/ShellIntR

CCCCCCCCCCCCCCCCCCCCC
C    TOTAL RESISTANCE
CCCCCCCCCCCCCCCCCCCCC

          RTOT = RCONTACT + RLIQ + RSOL + ShellIntR + RAIR

CCCCCCCCCCCCCCCCCCCCCCCCCCCCCCC
C    TEMPERATURES THROUGH GAP
CCCCCCCCCCCCCCCCCCCCCCCCCCCCCCC

        TMC = TMOLD+(TSHELL-TMOLD)*(RCONTACT/RTOT)
        TLS = (Tmc+(TSHELL-TMOLD)*((RSOL+RLIQ+RAIR)/RTOT))

CCCCCCCCCCCCCCCCCCCCCCCCCCCCCCCCCCCCCCCCCCC
C  DIVIDE GAP INTO LIQUID AND SOLID PARTS
CCCCCCCCCCCCCCCCCCCCCCCCCCCCCCCCCCCCCCCCCCC

        DSOL = (TCRYSTAL-TMC)*DGAP/(TLS-TMC)
        DLIQ = DGAP-DSOL
```

```
        IF ((DLIQ.LT.LiqThresh).OR.(FLAG.EQ.1.0D0)) THEN
            DSOL = DGAP
            DLIQ = 0.0D0
            RLIQ = 0.0D0
            RSOL = DSOL/KSOL
        ELSE
            RLIQ = DLIQ/KLIQ
            RSOL = DSOL/KSOL
        END IF

          ITER = ITER + 1.0D0


      END DO
CCCCCCCCCCCCCCCCCCCCCCCCCCCCCCCCCCCCCCCCCCCCCCCCCCCCCCCCCCCCCCCCCCCCCCC
CCCCCCCCCCCCCCCCCCCCCCCCCCCCCCCCCCCCCCCCCCCCCCCCCCCCCCCCCCCCCCCCCCCCCCC
C
C   END OF THE GAP LAYER ITERATION LOOP
C
CCCCCCCCCCCCCCCCCCCCCCCCCCCCCCCCCCCCCCCCCCCCCCCCCCCCCCCCCCCCCCCCCCCCCCC
CCCCCCCCCCCCCCCCCCCCCCCCCCCCCCCCCCCCCCCCCCCCCCCCCCCCCCCCCCCCCCCCCCCCCCC

1738  IF ((TSHELL.LT.1400.0D0).AND.(DSOL.EQ.DGAP)) THEN
        FLAG = 1.0D0
      END IF

CCCCCCCCCCCCCCCCCCCCCCCCCCCCCCCCC
C  GAP HEAT TRANSFER COEFFICIENT
CCCCCCCCCCCCCCCCCCCCCCCCCCCCCCCCC
      RGAP = RTOT
      HGAP = 1.0D0/RGAP
CCCCCCCCCCCCCCCCCCCCCCCCCCCCCCCCCC
C  PACK VALUES AND RETURN TO ABAQUS
CCCCCCCCCCCCCCCCCCCCCCCCCCCCCCCCCC
      AK(1) = HGAP/100.0D0  ! GAP CONDUCTANCE, mW/(mm^2*K)
      AK(2) = 0.0D0         ! DERIV WRT GAP SIZE
      AK(3) = 0.0D0         ! DERIV WRT PRESSURE
      AK(4) = 0.0D0         ! DERIV WRT SLAVE SURFACE TEMPERATURE
      AK(5) = 0.0D0         ! DERIV WRT MASTER SURFACE TEMPERATURE


      RETURN
      END SUBROUTINE GAPCON

CCCCCCCCCCCCCCCCCCCCCCCCCCCCCCCCCCCCCCCCCCCCCCCCCCCCCCCCCCCCCCCCCCCCCCC
```

```
CCCCCCCCCCCCCCCCCCCCCCCCCCCCCCCCCCCCCCCCCCCCCCCCCCCCCCCCCCCCCCCCCCCCCCCCCCCC
```

B.5 Parametric Study Scripts

B.5.1 Discrete Set Parametric Study Script

```
################################################################################
#                        PARAMETRIC STUDY PYTHON SCRIPT                        #
#           WRITTEN BY MATTHEW L.S. ZAPPULLA OCTOBER 7, 2014                   #
################################################################################
Copyright (c) <2016> <Matthew L.S. Zappulla>
################################################################################
Permission is hereby granted, free of charge, to any person obtaining a copy of
this software and associated documentation files (the "Software"), to deal in the
Software without restriction, including without limitation the rights to use, copy,
 modify, merge, publish, distribute, sublicense, and/or sell copies of the Software,
 and to permit persons to whom the Software is furnished to do so, subject to the
following conditions:

The above copyright notice and this permission notice shall be included in all copies
or substantial portions of the Software.

THE SOFTWARE IS PROVIDED "AS IS", WITHOUT WARRANTY OF ANY KIND, EXPRESS OR IMPLIED,
INCLUDING BUT NOT LIMITED TO THE WARRANTIES OF MERCHANTABILITY, FITNESS FOR A
PARTICULAR PURPOSE AND NONINFRINGEMENT. IN NO EVENT SHALL THE AUTHORS OR COPYRIGHT
HOLDERS BE LIABLE FOR ANY CLAIM, DAMAGES OR OTHER LIABILITY, WHETHER IN AN ACTION
OF CONTRACT, TORT OR OTHERWISE, ARISING FROM, OUT OF OR IN CONNECTION WITH THE
SOFTWARE OR THE USE OR OTHER DEALINGS IN THE SOFTWARE.
################################################################################


################################################################################
#                                                                              #
#   EXECUTE BY GIVING THE COMMAND: ABAQUS SCRIPT=THISFILENAMEWITHOUTEXTENSION   #
#                                                                              #
#   BE VERY CAREFUL SETTING UP YOUR INPUT TEMPLATE, COMMENT LINES ARE DANGEROUS  #
################################################################################
#                                                                              #
#   IF NEED BE MULTIPLE CPUS CAN BE SPECIFIED IN THE execOptions area below    #
```

```
#   i.e. execOptions=' USER=umatfile CPUS=numberofcores'                        #
#                                                                               #
#################################################################################
#                                                                               #
#   SETTING UP A MESH PARAMETER PARAMETRIC STUDY                                #
#                                                                               #
#       MESH STUDIES REQUIRE THAT YOUR MESH GENERATION BE PARAMETER BASED       #
#       THIS WILL USUALLY REQUIRE NODE GENERATION AND ELEMENT GENERATION        #
#                                                                               #
#################################################################################
#                                                                               #
# FOR SPECIFIC VALUE EVALUATION (AS OPPOSED TO GENERATING A SAMPLE SET IN A RANGE)#
#       parstudyfunction.sample(VALUES, par=parametername, values=(5,11,17,77))  #
#                                                                               #
#                                                                               #
#   "MESH" KEYWORD WILL CREATE A STUDY FOR ALL POSSIBLE COMBINATIONS            #
#                                                                               #
#################################################################################
##                            MAIN STUDY SETTINGS
#################################################################################
#################################################################################
#
#  THE GENERATED FILES WILL BE: templateinpname_prefix_studyname_C#
#    WHERE C# REPRESENTS THE SPECIFIC CASE NUMBER AND IS NOT USER DEFINEABLE
#
#   AFTER EXECUTION studyname.var CONTAINS THE DESIGN LIST WITH PARAMETER VALUES
#################################################################################

#  THE NAME OF YOUR PARAMETER BASED INPUT FILE OMITTING *.INP
templateinpname = 'BasicTemplate'

# THE PARAMETRIC STUDY NAME, FOLLOWS THE TITLE OF THE TEMPLATE FILE
prefix = 'ParametricStudy'

# THE DESIGN SET NAME, FOLLOWS THE STUDY NAME
studyname = 'DesignSetName'

#################################################################################

# THE NAME OF THE CHANGING PARAMETER IN YOUR INPUT FILE
discparametername = ('EX', 'MAXSTEP', 'DELTATEMP')

# DISCRETE VALUES
discval = ((20, 200, 400, 1000),(0.5, 1.0, 5.0, 10.0),(0.5, 1.0, 10.0, 20.0))
```

```
##############################################################################
##                        EXECUTION CONTROL SETTINGS
##############################################################################

# IF FORTRAN USER SUBROUTINE NEEDED enter name
#           OTHERWISE COMMENT THIS LINE OUT
forfile = 'UMAT'

# IF MULTIPLE CPUS REQUIRED i.e. TOTAL_D.O.F > 10,000
#           GENERAL RULE IS UP TO 10K DOF PER CORE
#   USING MORE PROCESSORS WHEN YOU DONT NEED TO WILL INCREASE SOLVER TIME
proc = 1



##############################################################################
##############################################################################
##                       END OF USER INPUT SECTION
##
##                        MODIFY BELOW AT YOUR OWN RISK
##############################################################################
##############################################################################
#
#  PARSTUDY CAN USE DIRECTORY=ON TO CREATE A FOLDER STRUCTURE FOR A COMPLICATED STUDY
#

parametername = discparametername
parstudyfunction = ParStudy(par=parametername,name=prefix)

nofdiscparameters = len(discparametername)

if nofdiscparameters > 0:
    for p in range(0,nofdiscparameters):
        vals = len(discval[p])
        for v in range(0,vals):
            parstudyfunction.define(DISCRETE, par=discparametername[p])
            parstudyfunction.sample(VALUES, par=discparametername[p], values=discval[p])


parstudyfunction.combine(MESH,name=studyname)

parstudyfunction.generate(template=templateinpname)

##############################################################################
#
#   OPTIONAL CONSTRAINTS ON THE STUDY
```

```
#   parstudyfunction.constrain('parametername[0]*parametername[1] < 100.')
#
################################################################################

################################################################################
#
#                           EXECUTION SECTION
#
################################################################################

if forfile == None:
    fname = ' ' + 'CPUS=' + proc
    parstudyfunction.execute(INTERACTIVE,execOptions=fname)
else:
    fname = ' ' + 'USER=' + forfile
    parstudyfunction.execute(INTERACTIVE,execOptions=fname)
```

B.5.2 Sampling Set Parametric Study Script

```
################################################################################
#           CONTINOUS SAMPLING PARAMETRIC STUDY PYTHON SCRIPT                  #
#           WRITTEN BY MATTHEW L.S. ZAPPULLA OCTOBER 7, 2014                   #
################################################################################
Copyright (c) <2016> <Matthew L.S. Zappulla>
################################################################################
Permission is hereby granted, free of charge, to any person obtaining a copy of
this software and associated documentation files (the "Software"), to deal in the
Software without restriction, including without limitation the rights to use, copy,
 modify, merge, publish, distribute, sublicense, and/or sell copies of the Software,
 and to permit persons to whom the Software is furnished to do so, subject to the
following conditions:

The above copyright notice and this permission notice shall be included in all copies
or substantial portions of the Software.

THE SOFTWARE IS PROVIDED "AS IS", WITHOUT WARRANTY OF ANY KIND, EXPRESS OR IMPLIED,
INCLUDING BUT NOT LIMITED TO THE WARRANTIES OF MERCHANTABILITY, FITNESS FOR A
PARTICULAR PURPOSE AND NONINFRINGEMENT. IN NO EVENT SHALL THE AUTHORS OR COPYRIGHT
HOLDERS BE LIABLE FOR ANY CLAIM, DAMAGES OR OTHER LIABILITY, WHETHER IN AN ACTION
OF CONTRACT, TORT OR OTHERWISE, ARISING FROM, OUT OF OR IN CONNECTION WITH THE
SOFTWARE OR THE USE OR OTHER DEALINGS IN THE SOFTWARE.
################################################################################
```

```
##############################################################################
#                                                                            #
#   EXECUTE BY GIVING THE COMMAND: ABAQUS SCRIPT=THISFILENAMEWITHOUTEXTENSION    #
#                                                                            #
#   BE VERY CAREFUL SETTING UP YOUR INPUT TEMPLATE, COMMENT LINES ARE DANGEROUS  #
##############################################################################
#                                                                            #
#   IF NEED BE MULTIPLE CPUS CAN BE SPECIFIED IN THE execOptions area below      #
#   i.e. execOptions=' USER=umatfile CPUS=numberofcores'                     #
#                                                                            #
##############################################################################
##                          MAIN STUDY SETTINGS
##############################################################################
##############################################################################
#
#  THE GENERATED FILES WILL BE: templateinpname_prefix_studyname_C#
#    WHERE C# REPRESENTS THE SPECIFIC CASE NUMBER AND IS NOT USER DEFINEABLE
#
#   AFTER EXECUTION studyname.var CONTAINS THE DESIGN LIST WITH PARAMETER VALUES
#
##############################################################################

#  THE NAME OF YOUR PARAMETER BASED INPUT FILE OMITTING *.INP
templateinpname = 'BasicTemplate'

# THE PARAMETRIC STUDY NAME, FOLLOWS THE TITLE OF THE TEMPLATE FILE
prefix = 'SamplingParametricStudy'

# THE DESIGN SET NAME, FOLLOWS THE STUDY NAME
studyname = 'DesignSetName'

##############################################################################

# THE NAME OF THE CHANGING PARAMETER IN YOUR INPUT FILE
contparametername = ('EX', 'MAXSTEP', 'DELTATEMP')

# THE STARTING AND ENDING VALUE OF THE CONTINOUS SAMPLE PARAMETERS
startval = (3, 0.5, 0.25)
endval   = (6, 5.0, 10.0)

# NUMBER OF CONTINOUS PARAMETER SAMPLES (INCLUSIVE AND EQUALLY SPACED)
num = (3, 3, 3)
```

```
###############################################################################
##                        EXECUTION CONTROL SETTINGS
###############################################################################

# IF FORTRAN USER SUBROUTINE NEEDED enter name
#           OTHERWISE COMMENT THIS LINE OUT
forfile = 'UMAT'

# IF MULTIPLE CPUS REQUIRED i.e. TOTAL_D.O.F > 10,000
# GENERAL RULE IS UP TO 10K DOF PER CORE
# USING MORE PROCESSORS WHEN YOU DONT NEED TO WILL SLOW YOUR STUDY DOWN
proc = 1



###############################################################################
###############################################################################
##                       END OF USER INPUT SECTION
##
##                        MODIFY BELOW AT YOUR OWN RISK
###############################################################################
###############################################################################
#
#   PARSTUDY CAN USE DIRECTORY=ON TO CREATE A FOLDER STRUCTURE FOR A COMPLICATED STUDY
#

parametername = contparametername
parstudyfunction = ParStudy(par=parametername,name=prefix)

nofcontparameters = len(contparametername)

if nofcontparameters > 0:
    for p in range(0,nofcontparameters):
        parstudyfunction.define(CONTINUOUS, par=contparametername[p], domain=(startval[p],endval[p]))
        parstudyfunction.sample(NUMBER, par=contparametername[p], number=num[p])


parstudyfunction.combine(MESH,name=studyname)
parstudyfunction.generate(template=templateinpname)

###############################################################################
#
#   OPTIONAL CONSTRAINTS ON THE STUDY
#   parstudyfunction.constrain('parametername[0]*parametername[1] < 100.')
#
```

```
###############################################################################

###############################################################################
#
#                           EXECUTION SECTION
#
###############################################################################

if forfile == None:
    fname = ' ' + 'CPUS=' + proc
    parstudyfunction.execute(INTERACTIVE,execOptions=fname)
else:
    fname = ' ' + 'USER=' + forfile
    parstudyfunction.execute(INTERACTIVE,execOptions=fname)
```

References

[1] J. S. Spoerl, "A Brief History of Iron and Steel Production." http://www.anselm.edu/homepage/dbanach/h-carnegie-steel.htm, 2013.

[2] H. Bessemer, "The Bessemer Steel Works At Troy," *The Journal of The Franklin Institute*, pp. 82–83, 1845.

[3] S. Mizoguchi, T. Ohashi, and T. Saeki, "Continuous Casting of Steel," *Annual Review Material Science*, pp. 151–169, 1981.

[4] J. Elfsberg, *Oscillation Mark Formation in Continuous Casting Processes*. PhD thesis, Royal Institute of Technology, 2003.

[5] E. Studies, "Steel Statistical Yearbook," *Steel Statistical Yearbook 2014 worldsteel*, vol. 1, p. 121, 2011.

[6] H. Bessemer, "Improvement in the manufacture of iron and steel." U.S. Patent: US49053 A, 1865.

[7] B. G. Thomas, "Introduction to Continuous Casting." http://ccc.mechse.uiuc.edu/introduction/concast.html.

[8] A. W. Cramb, "High Purity , Low Residual and Clean Steels."

[9] J. Oda, K. Akimoto, and T. Tomoda, "Long-term global availability of steel scrap," *Resources, Conservation and Recycling*, vol. 81, pp. 81–91, 2013.

[10] A. W. Cramb, "Issues in Caster Operation." Brimacombe Continuous Casting Course-Vancouver, 2013.

[11] I. V. Samarasekera and C. Chow, "Continuous Casting of Steel Billets," in *Making, Shaping and Treating of Steel*, ch. 18, pp. 1–46, Pittsburgh, PA: AISE Steel Foundation, 11th ed., 2002.

[12] A. W. Cramb, R. Rastogi, and R. L. Maddalena, "Nozzle Clogging," in *Making, Shaping and Treating of Steel*, ch. 10, pp. 1–17, Pittsburgh, PA: AISE Steel Foundation, 2002.

[13] L. C. Hibbeler and B. G. Thomas, "Mold Slag Entrainment Mechanisms in Continuous Casting Molds," in *AISTech - Iron and Steel Technology Conference Proceedings*, pp. 1215–1230, 2013.

[14] AEIS, "Effects of alloying elements on Steel." http://www.aeisndt.com/pdf/1 Effects of Alloying Elements on Steel.pdf, 2010.

[15] Z. G. Yang, D. M. Paxton, K. S. Weil, J. W. Stevenson, and P. Singh, "Materials Properties Database for Selection of High-Temperature Alloys and Concepts of Alloy Design for SOFC Applications," Tech. Rep. November, Pacific Northwest National Laboratory, Richland, Washington, 2002.

[16] J. K. Brimacombe and K. Sorimachi, "Crack formation in the continuous casting of steel," *Metallurgical and Materials Transactions B*, vol. 8, no. 2, pp. 489–505, 1977.

[17] S. Watanabe, K. Harada, and F. HitoshiShiro, "Continuous Casting," *Tetsu-to-Hagané*, vol. 58, no. 11, p. S393, 1972.

[18] Simulia, *Analysis User' s Manual: User Subroutines and Parametric Studies*, vol. VI. DS SIMULIA Corp, 2011.

[19] S. Koric, *Efficient Thermo-Mechanical Model for Solidification Processes and its Applications in Steel Continuous Casting*. PhD thesis, The University of Illinois at Urbana-Champaign, 2006.

[20] Y. Ueshima, S. Mizoguchi, T. Matsumiya, and H. Kajioka, "Analysis of solute distribution in dendrites of carbon steel with δ/γ transformation during solidification," *Metallurgical and Materials Transactions B*, vol. 17, no. 4, pp. 845–859, 1986.

[21] J. D. Hunt, "Steady state columnar and equiaxed growth of dendrites and eutectic," *Materials Science and Engineering*, vol. 65, no. 1, pp. 75–83, 1984.

[22] W. Kurz, "About initial solidification in continuous casting of steel," *Metallurgia Italiana*, vol. 100, no. 7, pp. 56–64, 2008.

[23] W. Kurz and D. J. Fisher, "Dendrite growth at the limit of stability: tip radius and spacing," *Acta Metallurgica*, vol. 29, no. 1, pp. 11–20, 1981.

[24] J. Lipton, W. Kurz, and R. Trivedi, "Rapid dendrite growth in undercooled alloys," *Acta Metallurgica*, vol. 35, no. 4, pp. 957–964, 1987.

[25] A. Chojecki, I. Telejko, and T. Bogacz, "Influence of chemical composition on the hot tearing formation of cast steel," *Theoretical and Applied Fracture Mechanics*, vol. 27, no. 2, pp. 99–105, 1997.

[26] W. T. Lankford, "Some considerations of strength and ductility in the continuous-casting process," *Metallurgical Transactions*, vol. 3, no. 6, pp. 1331–1357, 1972.

[27] J. Miettinen, S. Louhenkilpi, H. Kytönen, and J. Laine, "IDS: Thermodynamic kinetic empirical tool for modelling of solidification, microstructure and material properties," *Mathematics and Computers in Simulation*, vol. 80, no. 7, pp. 1536–1550, 2010.

[28] Y. M. Won, K.-h. Kim, T.-j. Yeo, and K. H. Oh, "Effect of Cooling Rate on ZST, LIT and ZDT of Carbon Steels Near Melting Point," *ISIJ International*, vol. 38, no. 10, pp. 1093–1099, 1998.

[29] K.-h. Kim, T.-j. Yeo, K. H. Oh, and D. N. Lee, "Effect of Carbon and Sulfur in Continuously Cast Strand on Longitudinal Surface Cracks," *ISIJ International*, vol. 36, no. 3, pp. 284–289, 1996.

[30] K. E. Blazek, O. Lanzi, P. L. Gano, and D. L. Kellogg, "Calculation of the peritectic range for steel alloys," in *AISTech - Iron and Steel Technology Conference Proceedings*, vol. 5, pp. 80–85, 2008.

[31] M. H. Burden and J. D. Hunt, "A Mechanism for the Columnar to Equiaxed Transition in Castings or Ingots," *Metallurgical and Materials Transactions A*, vol. 6A, pp. 240–241, 1975.

[32] S. C. Flood and J. D. Hunt, "Columnar and equiaxed growth. II. Equiaxed growth ahead of a columnar front," *Journal of Crystal Growth*, vol. 82, no. 3, pp. 552–560, 1987.

[33] W. J. Poole and F. Weinberg, "Observations of the columnar-to-equiaxed transition in stainless steels," *Metallurgical and Materials Transactions A*, vol. 29, no. 3, pp. 855–861, 1998.

[34] M. Rappaz, J. Drezet, and M. Gremaud, "A New Hot-Tearing Criterion," *Metallurgical and Materials Transactions A*, vol. 30A, pp. 449–455, 1999.

[35] Y. M. Won, T.-j. Yeo, D. J. Seol, and K. H. Oh, "A new criterion for internal crack formation in continuously cast steels," *Metallurgical and Materials Transactions B*, vol. 31, no. 4, pp. 779–794, 2000.

[36] D. G. Eskin and L. Katgerman, "Mechanical properties in the semi-solid state and hot tearing of aluminium alloys," *Progress in Materials Science*, vol. 49, pp. 629–711, 2004.

[37] T. W. Clyne and G. J. Davies, "The influence of composition on solidification cracking susceptibility in binary alloy systems," *British Foundryman*, vol. 74, pp. 65–73, 1981.

[38] H. Mizukami, S. Hiraki, M. Kawamoto, and T. Watanabe, "Initial Solidification Behavior of Ultra Low, Low and Middle Carbon Steel.," *ISIJ International*, vol. 39, no. 12, pp. 1262–1269, 1999.

[39] M. M. Wolf and K. Kurz, "The Effect of Carbon Content on Solidification of Steel in the Continuous Casting Mold," *Metallurgical and Materials Transactions B*, vol. 12, no. 1, pp. 85–93, 1981.

[40] M. Suzuki and Y. Yamaoka, "Influence of Carbon Content on Solidifying Shell Growth of Carbon Steels at the Initial Stage of Solidification," *Materials Transactions*, vol. 44, no. 5, pp. 836–844, 2003.

[41] B. Thomas and C. Ojeda, "Ideal taper prediction for slab casting," in *ISS Steelmaking Conference*, (Indianapolis, IN), pp. 295–308, ISS-AIME, 2003.

[42] H. Mehrara, D. G. Eskin, R. H. Petrov, M. Lalpoor, and L. Katgerman, "Linear contraction behavior of low-carbon, low-alloy steels during and after solidification using real-time measurements," *Metallurgical and Materials Transactions A*, vol. 45, no. 3, pp. 1445–1456, 2014.

[43] M. Reid, D. Phelan, and R. J. Dippenaar, "Concentric Solidification for High Temperature Laser Scanning Confocal Microscopy," *ISIJ International*, vol. 44, no. 3, pp. 565–572, 2004.

[44] M. Rowan, B. G. Thomas, R. Pierer, and C. Bernhard, "Measuring mechanical behavior of steel during solidification: Modeling the SSCC test," *Metallurgical and Materials Transactions B*, vol. 42, no. 4, pp. 837–851, 2011.

[45] A. Lagerstedt and H. Fredriksson, "A model for prediction of cracks in a solidifying shell," *Materials Science and Engineering: A*, vol. 414, pp. 37–43, 2005.

[46] Y. Meng, C. Li, J. Parkman, and B. G. Thomas, "Simulation of shrinkage and stress in solidifying steel shells of different grades," in *International Conference on Modeling of Casting, Welding and Advanced Solidification Processes* (M. Rappaz, ed.), (Charlotte, NC), pp. 33–39, The Minerals, Metals & Materials Society, 2004.

[47] H. G. Suzuki, S. Nishimura, and S. Yamaguchi, "Characteristics of Hot Ductility in Steels Subjected to the Melting and Solidification," *Transactions of the Iron and Steel Institute of Japan*, vol. 22, no. 1, pp. 48–56, 1982.

[48] P. J. Wray, "Tensile Failure Behavior of Plain Carbon Steels at Elevated Temperatures," *Metallurgical and Materials Transactions A*, vol. 15, no. 11, pp. 2059–2073, 1984.

[49] B. G. Thomas, J. K. Brimacombe, and I. V. Samarasekera, "The Formation of Panel Cracks in Steel Ingots: A State-of-the-Art Review, I. Hot Ductility of Steel," *Transactions of the Iron and Steel Society*, vol. 7, no. 10, pp. 7–20, 1986.

[50] C. H. Yu, M. Suzuki, H. Shibata, and T. Emi, "Simulation of Crack Formation on Solidifying Steel Shell in Continuous Casting Mold.," *ISIJ International*, vol. 36, no. Suppl, pp. S159–S162, 1996.

[51] M. B. Santillana, *Thermo-mechanical properties and cracking during solidification of thin slab cast steel*. PhD thesis, Delft University of Technology, 2013.

[52] S. Singh and K. E. Blazek, "Heat transfer and skin formation in a continuous-casting mold as a function of steel carbon content," *Journal of Metals*, pp. 17–27, 1974.

[53] S. Moon, *The peritectic phase transition and continuous casting practice*. PhD thesis, University of Wollongong, 2015.

[54] J. Konishi, M. Militzer, I. V. Samarasekera, and J. K. Brimacombe, "Modeling the formation of longitudinal facial cracks during continuous casting of hypoperitectic steel," *Metallurgical and Materials Transactions B*, vol. 33B, pp. 413–423, 2002.

[55] P. Presoly, R. Pierer, and C. Bernhard, "Identification of defect prone peritectic steel grades by analyzing high-temperature phase transformations," *Metallurgical and Materials Transactions A*, vol. 44, no. 12, pp. 5377–5388, 2013.

[56] E. Wielgosz and T. Kargul, "Differential scanning calorimetry study of peritectic steel grades," *Journal of Thermal Analysis and Calorimetry*, vol. 119, no. 3, pp. 1547–1553, 2015.

[57] A. Kagawa and T. Okamoto, "Influence of alloying elements on temperature and composition for peritectic reaction in plain carbon steels," *Materials Science and Technology*, vol. 2, no. 10, pp. 997–1008, 1986.

[58] C. Bale, P. Chartrand, and S. Degterov, "FactSage thermochemical software and databases," 2002.

[59] N. Saunders, U. K. Z. Guo, X. Li, a. P. Miodownik, and J. P. Schillé, "Using JMatPro to model materials properties and behavior," *The Journal of The Minerals, Metals & Materials Society (TMS)*, vol. 55, pp. 60–65, 2003.

[60] J. O. Andersson, T. Helander, L. Hoglund, P. Shi, and B. Sundman, "THERMO-CALC & DICTRA, Computational Tools For Materials Science," *Calphad*, vol. 26, no. 2, pp. 273–312, 2002.

[61] R. D. Pehlke, R. D. Jeyarajan, and H. Wada, "Summary of Thermal Properties for Casting Alloys and Mold Materials," tech. rep., National Science Foundation: Applied Research Division, Ann Arbor, Michigan, 1982.

[62] A. Jablonka, K. Harste, and K. Schwerdtfeger, "Thermomechanical properties of iron and iron-carbon alloys: density and thermal contraction," *Steel research*, vol. 62, no. 1, pp. 24–33, 1991.

[63] P. J. Wray, "High Temperature Plastic-Flow Behavior of Mixtures of Austenite, Cementite, Ferrite, and Pearlite in Plain-Carbon Steels," *Metallurgical and Materials Transactions A*, vol. 15A, no. 11, pp. 2041–2058, 1984.

[64] C. Li and B. G. Thomas, "Thermomechanical finite-element model of shell behavior in continuous casting of steel," *Metallurgical and Materials Transactions B*, vol. 35, no. 6, pp. 1151–1172, 2004.

[65] J. Sengupta, C. Ojeda, and B. G. Thomas, "Thermal-mechanical behaviour during initial solidification in continuous casting: steel grade effects," *International Journal of Cast Metals Research*, vol. 22, no. 1, pp. 8–14, 2009.

[66] B. G. Thomas, G. Li, A. Moitra, and D. Habing, "Analysis of Thermal and Mechanical Behavior of Copper Molds during Continuous Casting of Steel Slabs," in *80th Steelmaking Conference*, (Chicago, Illinois), pp. 1–19, 1997.

[67] R. J. Dippenaar, I. V. Samarasekera, and J. K. Brimacombe, "Mold taper in continuous casting billet machines," *ISS Transactions*, vol. 7, pp. 33–43, 1986.

[68] D. P. Lorento, "Billet Mold Taper and Secondary Cooling Pattern Design." Private Communication, 2002.

[69] C. Li and B. G. Thomas, "Maximum casting speed for continuous cast steel billets based on sub-mold bulging computation," in *85th Steelmaking Conference Proceedings*, (Warrendale, PA), pp. 109–130, Iron and Steel Society, 2002.

[70] C. Li and B. G. Thomas, "Ideal taper prediction for billet casting," *ISS Steelmaking Conference*, pp. 295–308, 2003.

[71] Ridolfi, B. G. Thomas, and Foglia, "The optimization of mold taper for the Ilva-Dalmine round bloom caster," *La Revue de Metallurgie-CIT*, vol. 91, no. 4, pp. 609–620, 1994.

[72] B. G. Thomas and W. Storkman, "Mathematical Models of Continuous Slab Casting to Optimize Mold Taper," in *Modeling and Control of Casting and Welding Processes - IV* (A. Giamei and G. Abbaschian, eds.), (Palm Coast, Florida), pp. 287–297, The Metallurgical Society, 1988.

[73] A. Moitra, B. G. Thomas, and W. Storkman, "Thermo-Mechanical Model of Steel Shell Behavior in the Continuous Casting Mold," in *TMS Annual Meeting*, (San Diego, CA), pp. 1–31, The Minerals, Metals & Materials Society, 1992.

[74] B. Bottger, M. Apel, M. B. Santillana, and D. G. Eskin, "Relationship between solidification microstructure and hot cracking susceptibility for continuous casting of low-carbon and high-strength low-alloyed steels: A phase-field study," *Metallurgical and Materials Transactions A*, vol. 44, no. 8, pp. 3765–3777, 2013.

[75] J. Tiaden, "Phase field simulations of the peritectic solidification of Fe-C," *Journal of Crystal Growth*, vol. 198-199, pp. 1275–1280, 1999.

[76] B. Bottger, G. J. Schmitz, and M. B. Santillana, "Multi-phase-field modeling of solidification in technical steel grades," *Transactions of the Indian Institute of Metals*, vol. 65, no. 6, pp. 613–615, 2012.

[77] B. G. Thomas, G. Li, A. Moitra, and D. Habing, "Analysis of thermal and mechanical behavior of copper molds during continuous casting of steel slabs," *Iron and Steelmaker(USA)*, pp. 1–19, 1998.

[78] A. Howe, "Micro-Segregation: Issues of Growth Rate and the Peritectic," *Materials Science Forum*, vol. 649, pp. 419–424, 2010.

[79] H. Fredriksson, "The mechanism of the peritectic reaction in iron-base alloys," *Metal Science*, vol. 10, no. 3, pp. 77–86, 1976.

[80] H. Mizukami, A. Yamanaka, and T. Watanabe, "Prediction of Density of Carbon Steels.," *ISIJ International*, vol. 42, no. 4, pp. 375–384, 2002.

[81] M. L. S. Zappulla, L. C. Hibbeler, and B. G. Thomas, "Thermal-Mechanical Analysis of Grade Effects During Initial Solidification of Steels," *Manuscript in Preparation*, 2016.

[82] J. A. Dantzig and C. L. Tucker III, *Modeling in Materials Processing*. Cambridge University Press, 2001.

[83] S. Koric and B. G. Thomas, "Thermo-mechanical models of steel solidification based on two elastic visco-plastic constitutive laws," *journal of materials processing technology*, vol. 7, pp. 408–418, 2008.

[84] E. C. Bingham, "An investigation of the laws of plastic flow," *Bulletin of the Bureau of Standards*, vol. 13, pp. 309–353, 1916.

[85] S. Koric and L. C. Hibbeler, "Multiphysics Model of Metal Solidification on the Continuum Level," *Numerical Heat Transfer*, no. October 2013, pp. 37–41, 2010.

[86] B. G. Thomas, R. O. Malley, T. Shi, Y. Meng, D. Creech, and D. Stone, "Validation of fluid flow and solidification simulation of a continuous thin-slab caster," in *Modeling of casting, welding and advanced solidification processes IX*, pp. 769–776, 2000.

[87] J. K. Brimacombe, "Design of continuous casting machines based on a heat-flow analysis: state-of-the-art review," *Canadian Metallurgical Quarterly*, vol. 15, no. 2, pp. 163–175, 1976.

[88] C. Cicutti, M. Valdez, T. Perez, G. DiGresia, W. Balante, and J. Petroni, "Mould Thermal Evaluation in a Slab Continuous Casting Machine," in *Steelmaking Conference Proceedings*, (Warrendale, PA), pp. 97–107, Iron and Steel Society, 2002.

[89] N. Kapaj, M. Pavlicevic, and A. Poloni, "Exceeding the casting speed of bloom cc machines by three times," in *Steelmaking Conference Proceedings*, (Warrendale, PA), pp. 369–376, Iron and Steel Society, 2001.

[90] J. K. Park, B. G. Thomas, and I. V. Samarasekera, "Analysis of thermo-mechanical behaviour in billet casting with different mould corner radii," *Ironmaking & Steelmaking*, vol. 29, no. 5, pp. 359–375, 2002.

[91] M. M. Wolf, "Mold Length in Slab casting - A Review," *Iron & Steelmaker*, vol. 23, no. 2, pp. 47–51, 1996.

[92] P. Duvvuri, B. Petrus, and B. G. Thomas, "Correlation for Mold Heat Flux Measured in a Thin Slab Casting Mold," in *AISTech - Iron and Steel Technology Conference Proceedings*, (Indianapolis, IN), pp. 2881–2894, AIST, 2014.

[93] A. W. Cramb, "The Brimacombe Continuous Casting Course: Slag Emulsification." Brimacombe Continuous Casting Course-Vancouver, 2013.

[94] M. M. Wolf, "Mold Heat Transfer and Lubrication Control - Two Major Functions of Caster Productivity and Quality Assurance," in *Continuous Casting. Vol 9, Initial Solidification and Strand Surface Quality of Peritectic Steels* (M. M. Wolf, ed.), pp. 211–229, Warrendale, PA: Iron and Steel Society/AIME, 1997.

[95] Y. M. Won and B. G. Thomas, "Simple model of microsegregation during solidification of steels," *Metallurgical and Materials Transactions A*, vol. 32, no. 7, pp. 1755–1767, 2001.

[96] Y. Meng and B. G. Thomas, "Heat-transfer and solidification model of continuous slab casting: CON1D," *Metallurgical and Materials Transactions B*, vol. 34B, no. 5, pp. 685–705, 2003.

[97] K. Harste, *Investigation of the shrinkage and the origin of mechanical tension during the solidification and successive colling of cylindrical bars of Fe-C alloys*. PhD thesis, Technischen Universität Clausthal, 1989.

[98] E. Mizikar, "Mathematical heat transfer model for solidification of continuously cast steel slabs," *Transactions of the Metallurgical Society of AIME*, vol. 239, pp. 1747–1753, 1967.

[99] I. Jimbo and A. W. Cramb, "The density of liquid iron-carbon alloys," *Metallurgical and Materials Transactions B*, vol. 24, no. 1, pp. 5–10, 1993.

[100] H. Mizukami, K. Murakami, and Y. Miyashita, "Elastic modulus of steels at high temperature," *Journal of the Iron and Steel Institute of Japan*, vol. 63, no. 146, 1977.

[101] B. G. Thomas, I. V. Samarasekera, and J. K. Brimacombe, "Mathematical model of the thermal processing of steel ingots: Part II. Stress model," *Metallurgical and Materials Transactions B*, vol. 18, no. 1, pp. 131–147, 1987.

[102] P. J. Wray, "Effect of Carbon Content on the Plastic Flow of Plain Carbon Steels at Elevated Temperatures," *Metallurgical and Materials Transactions A*, vol. 13, no. 1, pp. 125–134, 1982.

[103] H. Zhu, *Coupled Thermo-Mechanical Finite-Element Model With Application to Initial Soldification*. PhD thesis, The University of Illinois at Urbana-Champaign, 1996.

[104] P. F. Kozlowski, B. G. Thomas, J. A. Azzi, and H. Wang, "Simple constitutive equations for steel at high temperature," *Metallurgical and Materials Transactions A*, vol. 23A, no. 3, pp. 903–918, 1992.

[105] S. Koric, L. C. Hibbeler, and B. G. Thomas, "Explicit coupled thermo-mechanical finite element model of steel solidification," *International Journal for Numerical Methods in Engineering*, vol. 78, no. 1, pp. 1–31, 2009.

[106] J. J. Weiner and B. B. Boley, "Elasto-plastic thermal stresses in a solidifying body," *Journal of the Mechanics and Physics of Solids*, vol. 1, no. 3, pp. 145–154, 1963.

[107] R. D. Cook, *Concepts and Applications of Finite Element Analysis*. Wiley, 1989.

[108] ABAQUS, *Abaqus 6.11 theory manual*. DS SIMULIA Corp, 2011.

[109] L. C. Hibbeler and B. G. Thomas, "Longitudinal face crack prediction with thermo-mechanical models of thin slabs in funnel moulds," in *6th European Continuous Casting Conference*, (Ricionne, Italy), pp. 1–16, Association Italiana Metallurgia, 2008.

[110] R. Pierer, C. Bernhard, and C. Chimani, "A contribution to hot tearing in the continuous casting process," *La Revue de Metallurgie-CIT*, vol. 3, no. 3, pp. 72–83, 2007.

[111] B. G. Thomas and J. Parkman, "Simulation of thermal mechanical behavior during initial solidification," in *Thermec 1997 International Conference on Thermomechanical Processing of Steel and Other Materials*, pp. 2279–2285, 1997.

[112] L. C. Hibbeler, M. M. Langeneckert, J. Iwasaki, I. Hwang, R. J. O. Malley, and B. G. Thomas, "Calibration of Thermal Models of Continuous Casting of Steel," in *AISTech - Iron and Steel Technology Conference Proceedings*, pp. 1291–1301, 2012.

[113] T. J. Piccone, I. Sohn, T. T. Natarajan, and E. J. Serrano, "Observations on Mold Corner Temperatures Measured using Thermocouples," in *AISTech - Iron and Steel Technology Conference Proceedings*, no. 2, pp. 1–12, Association for Iron and Steel Technology, 2007.

[114] L. C. Hibbeler and B. G. Thomas, "The Thermal Distortion of a Funnel Mold," in *AISTech - Iron and Steel Technology Conference Proceedings*, pp. 1–10, 2012.

[115] T. Murakami and H. Kashima-cho, "Improvements of Longitudinal Corner Cracks at High-Speed Casting," in *Current Advances in Materials and Processes: Report of the ISIJ Meeting*, vol. 5, (Tokyo), p. 1291, Iron and Steel Institute of Japan, Iron and Steel Institute of Japan, 1992.

[116] K. C. Mills and A. B. Fox, "The Role of Mould Fluxes in Continuous Casting-So Simple Yet So Complex," *ISIJ International*, vol. 43, no. 10, pp. 1479–1486, 2003.

[117] J. K. Brimacombe, F. Weinberg, and E. B. Hawbolt, "Formation of Longitudinal , Midface Cracks in Continuously-Cast Slabs," *Metallurgical and Materials Transactions B*, vol. 10, pp. 279–292, 1979.

[118] D. T. Stone and B. G. Thomas, "Measurement and modeling of heat transfer across interfacial mold flux layers," *Canadian Metallurgical Quarterly*, vol. 38, no. 5, pp. 363–375, 1999.

[119] J. Cho, H. Shibata, T. Emi, and M. Suzuki, "Thermal Resistance at the Interface between Mold Flux Film and Mold for Continuous Casting of Steels.," *ISIJ International*, vol. 38, no. 5, pp. 440–446, 1998.

[120] Y. Meng, B. G. Thomas, a.a. Polycarpou, a. Prasad, and H. Henein, "Mould Slag Property Measurements To Characterize Cc Mould âĂŞ Shell Gap Phenomena," *Canadian Metallurgical Quarterly*, vol. 45, no. 1, pp. 79–94, 2006.

[121] K. C. Mills, A. Fox, Z. Li, and R. Thackray, "Performance and properties of mould fluxes," *Ironmaking & Steelmaking*, vol. 32, no. 1, pp. 26–34, 2005.

[122] K. C. Mills, "Mold Powders for Continuous Casting," in *The Making, Shaping, and Treating of Steel*, ch. 9, pp. 1–41, AISE Steel Foundation, 2003.

[123] A. S. M. Jonayat and B. G. Thomas, "Transient Thermo-fluid Model of Meniscus Behavior and Slag Consumption in Steel Continuous Casting," *Metallurgical and Materials Transactions B*, vol. 45, no. 5, pp. 1842–1864, 2014.

[124] H. Hasegawa, H. Ohta, H. Shibata, and Y. Waseda, "Recent development in the investigation on thermal conductivity of silicate melts," *High Temperature Materials and Processes*, vol. 31, no. 4-5, pp. 491–499, 2012.

[125] R. M. Mcdavid and B. G. Thomas, "Flow and Thermal Behavior of the Top Surface Flux / Powder Layers in Continuous Casting Molds," *Metallurgical and Materials Transactions B*, vol. 27, no. 4, pp. 672–685, 1996.

[126] J. E. Kelly, K. P. Michalek, T. G. O'connor, B. G. Thomas, and J. A. Dantzig, "Initial development of thermal and stress fields in continuously cast steel billets," *Metallurgical Transactions A*, vol. 19, no. 10, pp. 2589–2602, 1988.

[127] A. Bejan, *Convection Heat Transfer*. Hoboken, NJ, USA: John Wiley & Sons, Inc., fourth ed., 2013.

[128] B. G. Thomas and J. T. Parkman, "Simulation of thermal distortion of a steel droplet solidifying on a copper chill," in *The Materials Society Annual Meeting* (M. Chu and E. Lavernia, eds.), (San Antonio, TX), pp. 509–520, The Minerals, Metals & Materials Society, 1998.